The Dissertation Committee for Stephen Larkin Gibbs Certifies that this is the approved version of the following Dissertation:

Nonuniform Charge Carrier Distribution within Plasmonic Semiconductor Nanocrystals

Committee:

Delia Milliron, Supervisor

Carlton Grant Willson

Charlies Buddie Mullins

Sean Roberts

Brian Korgel

Nonuniform Charge Carrier Distribution within Plasmonic Semiconductor Nanocrystals

by

Stephen Larkin Gibbs

Dissertation

Presented to the Faculty of the Graduate School of

The University of Texas at Austin

in Partial Fulfillment

of the Requirements

for the Degree of

Doctor of Philosophy

The University of Texas at Austin

August 2021

Acknowledgements

I've always enjoyed being a part of a team. Failures have less sting. Successes bring more joy. I think many expect a PhD journey to be the plight of one – that was not the case for me. With guidance from mentors, collaboration with technicians and colleagues, support from family, and companionship from friends, my PhD was a team sport and I owe a lot to my teammates.

The DMG team. My gratitude first goes to our fearless leader, Prof. Delia Milliron. You have built a culture that values criticism and inspires interest and collaboration across a wide range of topics. Thank you for giving me so many opportunities throughout my PhD to grow as a scientist, a leader, and a mentor. I aim to emulate your approach to science as I move forward in my career. I enjoyed learning from you and I of course enjoyed all of the celebratory drinks and food we shared as a group along the way. Omid, thank you for taking the time to teach me and bring me in on a depletion project that ended up being a central piece of my thesis. Molly, thank you for being a great desk mate and always being down to chat about science or life. Ankit, thank you for being willing to stop whatever you are doing to answer my dumb questions about plasmonics, coupling, electrochromism.. you were a truly invaluable resource for me and always a pleasure to chat with as a mentor and friend. Clay, thank you for being a leader to look up to in lab and being a great hang outside of lab – it was a blast getting to play flag football together! Gary, thank you for the stimulating intellectual discussions. In the beginning, you were always someone I could go to for sage lab advice, but as I progressed in my PhD you made me feel like a true colleague when we discussed science and I thank you for that. Camila, you always served as an example for me on how to do things right – whether it be in lab, in group meeting, or giving a presentation. As you neared the end of your PhD and we began to collaborate, I really

began to value or friendship in and out of lab and it was/is so nice to have you to talk about any topic under the sun! I will always treasure our lunchtime discussions. Sungyeon, thank you for serving as an example of how hard work pays off! Lauren, thank you for valuable lunchtime conversations over the years and always being the first to organize a group gathering – you always knew how to make me and others feel welcome! Rob, I was so lucky to have you as my mentor when I joined the group. I felt like a sponge absorbing everything you had to say about plasmans and synthesis. I recall one time in particular that you came in on a weekend to show me how to set up a Schlenk line and I think that exemplifies the lengths you were willing to go to help me out. I enjoyed learning from you and sharing French press coffee. Corey, my PhD would have been much less enjoyable without you. By the end of your time in Austin you felt much more like a brother than a labmate. Thank you so much for your consistent guidance and your motivation. I am a more effective scientist today because I got to watch the way you carry out your work. And thank you for being a great friend in and out of lab. I'm glad I got to watch you break an espresso drinking record that will hold forever… all the while building a tower of monster. Bharat, for someone who has left and returned so many times it is surprising that I feel as if you were with me throughout my entire PhD. Thank you for being an amazing collaborator and friend, but most importantly thank you for being my valentine. Manny, I remember the very first time we met on the picnic table outside of Littelfield café. I instantly knew how lucky I was to have such a friendly, motivated partner throughout my PhD. Thank you for always answering my dumb questions about ligands and surface chemistry and for being a jovial respite from the harrows of PhD life. Vikram, thank you for always being willing to chip in and help wherever the lab needs you and thanks for your puns - I hope you achieve your dreams of being a filmmaker. Hsin-Che, I've always admired your diligence to work and clarity of presentations. Thank you for being a steady

drumbeat of progress for our group. Kihoon, thank you for being my desk mate in the plasmon corner. You are a great scientist and I'm happy to have had the opportunity to discuss science with you over the years. Sofia, I've enjoyed getting to watch you grow from an undergraduate researcher into an independent scientist! Thanks for your inquisitive, positive attitude and willingness to help out anywhere that needs helping. Allison, I've admired your ability to take on a variety of complex projects from the jump. Thanks for being a great friend and collaborator in lab! Ben, it has been great getting to work with you for a couple years. I look forward to seeing what you will accomplish and thank you for always showing cute pictures of Ralph. Jiho, thanks for sticking it out on the night shift with me and always being open to project discussions. To my undergraduate students, Joey and Christopher, thanks for tolerating my slightly overbearing mentorship style. I would not have completed my PhD without the contributions from either of you. A special thanks to Christopher for sticking it out through COVID and picking up a whole new skill, simulation, that I knew nothing about! I know you will both go on to be successful in your future!

The McKetta Team. Having just talked up my own research group, I would be remiss to not acknowledge our department as a whole. It's not easy to build a sense of community within a graduate chemical engineering department, but by george we certainly try. From tailgates to intramural sports (shout out to our coed flag football teams that won two championships!), to community service and a host of other activities, I want to thank our faculty and administration for promoting a healthy work life balance. I also want to thank all those who served on the graduate chemical engineering leadership council (GLC) and worked to promote this fellowship.

The Pinky's Up Team. I could not imagine a better crew for tackling a PhD program. When life is rough, you've been there to lift me up. And when life is good, you

lift me up even higher! I can honestly say I will look back on these 5 years as some of the best of my life because of you all.

The Gibbs Team. I've appreciated the support and motivation from each of you. Long chats with mom and pop on the weekend help me decompress and rejuvenate. Catching up with my siblings and hearing how they are progressing in their own lives and how they are proud of me motivates me to do better myself! I really appreciate all of the visits and enjoyed getting to host you all in my city! It helped Austin feel like home. I love you all so much and I am so lucky to have you as a support system.

Abstract

Nonuniform Charge Carrier Distribution within Plasmonic Semiconductor Nanocrystals

Stephen Larkin Gibbs, PhD

The University of Texas at Austin, 2021

Supervisor: Delia Milliron

Plasmonic nanocrystals (NCs) can act as focusing lenses that capture incident light at wavelengths near the localized surface plasmon resonance peak frequency (ω_{LSPR}) and confine it into nanoscopic volumes. This concentration of photon energy manifests in enhanced electric fields, increased temperature, and even electron transfer near the nanocrystal surface. Traditional plasmonic materials, metals, have ω_{LSPR} in the visible range, whereas doped semiconductor nanocrystals have ω_{LSPR} tunable through the infrared. This has helped to expand plasmon-enhanced processes to include those that lie within infrared wavelengths such as molecular sensing, photothermal therapy, and infrared driven photochemistry. The infrared ω_{LSPR} arises from a lower charge carrier concentration in doped semiconductors as compared to metals, which also promotes another phenomenon: nonuniform intra-NC charge carrier concentration. Depletion regions near the NC surface create an insulating shell, nearly devoid of charge carriers, that surrounds the higher carrier concentration, plasmonic core. This depletion layer can hinder all forms of plasmon-enhancement. Through careful colloidal synthetic techniques, quantitative spectroscopy, and Drude theory modelling, I demonstrated understanding and control over the thickness

of this depletion layer with varied size and doping concentration. Going one step further, I employed radial control over dopant placement to not only tune the depletion layer thickness, but the entire intra-NC carrier concentration profile. In fact, I engineered a doping profile that promoted a secondary plasmonic absorption mode within a single nanocrystal. Engineering the intra-NC doping profile is uniquely achievable for doped semiconductor, which opens up the door to improved infrared plasmonic devices.

Table of Contents

List of Tables xiii

List of Figures xiv

Chapter 1: Introduction 1

1.1 Motivation 1

1.2 Fundamental Concepts 3

1.2.1 The Dielectric Function of a Metal 4

1.2.2 Absorption and Scattering by a Sphere 9

1.2.3 Localized Surface Plasmon Resonance 11

1.2.4 Doped Metal Oxide Nanocrystals 14

1.2.4.1 Electronic Band Structure of Semiconductors 15

1.2.4.2 Doping and Defect Chemistry 20

1.2.4.3 Colloidal Synthesis 24

1.2.5 Near-Surface Charge Carrier Depletion 26

1.3 Dissertation Overview 30

Chapter 2: Quantitative Analysis of Extinction Coefficients of Tin-Doped Indium Oxide Nanocrystals 32

2.1 Introduction 32

2.2 Quantifying Extinction Coefficients in NC Dispersions 35

2.3 Doping Series 37

2.4 Size Series 39

2.5 Magnitude of ITO NC Extinction 41

2.6 Conclusion 42

2.7 Future Work: Failure of Standard Fitting Procedures 42

Chapter 3: Intrinsic Optical and Electronic Properties from Quantitative Analysis of Plasmonic Semiconductor Nanocrystal Optical Extinction 44

3.1 Introduction 44

3.2 Methods 47

3.2.1 Fitting Procedure. 47

3.3 Results and Discussion 48

3.3.1 Fitting NC Ensemble Optical Spectra 48

3.3.1.1 Near-surface depletion regions 51

3.3.1.2 Intrinsic damping 52

3.3.1.3 Ensemble heterogeneity 53

3.3.2 HEDA Fit Results 56

3.3.2.1 Quantifying ensemble heterogeneity 56

3.3.2.2 Intrinsic properties for the average NC in an ensemble 58

3.3.3 HEDA Fit Results Align with Mie Scattering Theory 61

3.3.4 Optical and Electronic Properties Derived from HEDA Model Fit Results 64

3.4 Conclusions 68

Chapter 4: Segregating Dopants within Semiconductor Nanocrystals 70

4.1 Tuning Nanocrystal Surface Depletion By Controlling Dopant Distribution as a Means to Route toward Enhanced Film Conductivity 70

4.1.1 Mitigating Depletion through Chemical Modification of the NC Surface 70

4.1.2 Tuning the Depletion Width by Controlling Intra-NC Dopant Distribution 72

4.2 Dual-Mode Infrared Absorption by Segregating Dopants within Plasmonic Semiconductor Nanocrystals 75

4.2.1 Introduction 76
4.2.2 Shell-Doped Series 78
4.2.3 Extracting Electronic Parameters 82
4.2.4 Core-Doped Series 84
4.2.5 Dielectric Sensitivity 87
4.2.6 Conclusion 91
Chapter 5: Looking Ahead for Nonuniform Carrier Concentration in Nanomaterials 93
Appendices 96
Appendix A: Supporting Information to Chapter 2 96
Text A1: Synthesis of ITO NCs 96
Text A2: Spectroscopy measurements 97
Text A3: Small-angle X-ray scattering measurements (SAXS) 97
Text A4: Scanning transmission electron microscopy (STEM) measurements 98
Text A5: Inductively coupled plasma-atomic emission spectroscopy (ICP-AES) measurements 98
Appendix B: Supporting Information to Chapter 3 105
Appendix C: Supporting Information to Chapter 4 109
Text C1: Nanocrystal Synthesis 109
Text C2: Inductively Coupled Plasma-Atomic Emission Spectroscopy (ICP-AES) 110
Text C3: X-ray Photoelectron Spectroscopy (XPS) 110
Text C4: Visible and Infrared Spectroscopy 110
Text C5: Effective Medium Theory 111
References 119

List of Tables

Table 4.1: Experimentally measured properties of shell-doped samples. 80

Table 4.2: Experimentally measured properties of core-doped samples. 86

Table 4.3: A comparison of the dielectric sensitivity of nanocrystals with differing dopant segregation. 90

Table A1: Comparison of extinction efficiency across materials. 104

Table B1: Size series fit parameters and calculated properties. 106

Table B2: Dopant concentration series fit parameters and calculated properties. 106

Table C1: Average and standard deviation of fit results for shell-doped samples for three independently prepared dispersions of varying NC concentration. 113

Table C2: Average and standard deviation of fit results for core-doped samples for three independently prepared dispersions of varying NC concentration. 113

Table C3: Average and standard deviation of fit results for three independently prepared dispersions of varying NC concentration for each sample. 118

List of Figures

Figure 1.1: Wavelength regimes of the electromagnetic spectrum. 1

Figure 1.2: A parallel plate capacitor.. 5

Figure 1.3: The incompressible electron gas (blue) is displaced from the solid metal (red) by an average distance x when an external electric field is applied.. 8

Figure 1.4: The different colors of the Lycurgus cup..... 9

Figure 1.5: The amount of light that is either transmitted, absorbed, or scattered when interacting with a particle 10

Figure 1.6: Schematic depicting localized surface plasmon resonance 12

Figure 1.7: Absorption and scattering cross-sections calculated based on Mie theory.... 13

Figure 1.8: Electronic structure of sodium as a function of interatomic spacing..... 17

Figure 1.9: Electronic band structure of a typical semiconductor (a) and metal (b)..... 18

Figure 1.10: The Fermi-Dirac distribution at (a) zero Kelvin and (b) finite temperature 19

Figure 1.11: Energy level diagrams for an undoped (left) and doped (right) semiconductor..... 21

Figure 1.12: Energy level diagrams for an increasingly n-type doped (left to right) semiconductors 22

Figure 1.13: Surface and bulk energy contributions to overall free energy 25

Figure 1.14: Schematic depicting typical setup for slow-injection colloidal synthesis of metal oxide NCs 26

Figure 1.15: Schematic illustration the negative effects of depletion on optical extinction and NC conductivity..... 27

Figure 1.16: Simulated surface depletion in an ITO NC..... 29

Figure 2.1: Determination of extinction coefficient 37

Figure 2.2: Dopant concentration series at constant NC diameter 38

Figure 2.3: Size series at constant dopant concentration 39

Figure 3.1: Three models for fitting extinction spectra. Simple Drude approximation (SDA) with a floating NC volume fraction, SDA with volume fraction fixed to the measured value, and heterogeneous ensemble Drude approximation (HEDA) fits to extinction data for 5 at% Sn 6 nm ITO NCs. 49

Figure 3.2: Calculated LSPR spectra. Volume-normalized extinction spectra for ITO NC ensembles of varying NC radius (a), NC radius polydispersity (b), electron concentration (c), electron concentration polydispersity, electron accessible volume fraction (e), and bulk mean free path (f) 50

Figure 3.3: Theoretical concepts for surface depletion and surface scattering 52

Figure 3.4: Quantification of ensemble heterogeneity. Polydispersity in radius measured by small angle X-ray scattering (SAXS) and polydispersity in carrier concentration extracted by fitting with the HEDA model as a function of NC radius (a) and at% Sn (b). 58

Figure 3.5: HEDA Fit results 59

Figure 3.6: Ensemble and average NC extinction. Volume-normalized peak extinction coefficient extracted from SDA (a) and HEDA (b) fits to ensemble spectra. 63

Figure 3.7: Trends in optical extinction. Peak volume-normalized extinction from all spectra plotted in Figure 3.2 64

Figure 3.8: Ensemble and average NC optical properties. Q-factor calculated from the ensemble spectrum and the spectrum of the average NC within that ensemble acquired through HEDA modeling as a function of NC radius (a) and doping level (b) 65
Figure 3.9: Ensemble and average NC electronic properties 67
Figure 4.1: Identifying adsorbed water species as a surface state in metal oxide NCs using in situ sheet resistance measurements. 72
Figure 4.2: NC film conductivity dependence on near-surface dopant concentration before and after alumina ALD. 74
Figure 4.3: Carrier concentration profiles for NCs of different radial doping distribution. All NCs have ~3 at% Sn overall and are ~20 nm in diameter. 75
Figure 4.4: Experimental trends in shell-doped NCs. (a) Normalized experimental extinction spectra for the shell-doped series. (b) ICP-OES and XPS quantification of at% Sn for each sample 79
Figure 4.5: STEM images and size histograms of the shell-doped series. 81
Figure 4.6: Experimental trends in core-doped NCs. (a) Normalized experimental extinction spectra for the core-doped series. (b) ICP-OES and XPS quantification of at% Sn for each sample in the CD series 85
Figure 4.7: STEM images and size histograms of the core-doped series 86
Figure 4.8: Dielectric sensitivity of dopant segregated NCs 89
Figure 5.1: Normalized extinction spectra for dispersions of CdO NCs of increasing size. 94
Figure 5.2: Carrier concentration profiles for ITO NCs of different radial doping distribution. 95

Figure A1: STEM images of 20 nm 0 at% (a), 1 at% (b), 3 at% (c), 4.5 at% (d), 5 at% (e), 6 at% (f), and 7.5 at% (g) ITO NCs and 6 nm (h), 8 nm (i), 11 nm (j), 12 nm (k),14 nm (l), 15 nm (m), 16 nm (n), and 18 nm (o) 5 at% ITO NCs 99

Figure A2: SAXS of 20 nm 0 at% (a), 1 at% (b), 3 at% (c), 4.5 at% (d), 5 at% (e), 6 at% (f), and 7.5 at% (g) ITO NCs. 100

Figure A3: SAXS of 6 nm (a), 8 nm (b), 11 nm (c), 12 nm (d),14 nm (e), 15 nm (f), 16 nm (g), and 18 nm (h) 5 at% ITO NCs. 101

Figure A4: Brouwer Diagram showing the concentration dependence of various defects in ITO with respect to Sn concentration 102

Figure A5: Tauc plots of ITO NCs showing optical bandgap widening with increasing dopant concentration (a) and NC radius (b and c). 103

Figure B1: Optical extinction fits for SDA with a floating NC volume fraction, SDA with measured NC volume fraction, and HEDA model 105

Figure B2: Dopant activation. 107

Figure B3: SDA volume-normalized extinction compared to the ensemble spectrum. . 107

Figure B4: HEDA-derived average NC extinction spectra compared to ensemble 108

Figure B5: Bulk ITO electronic properties. 108

Figure C1: Assigning molecular vibrational modes 111

Figure C2: Comparison of calculated values for core volume fraction based on STEM imaging and based on fitting optical spectra 114

Figure C3: Extracted values for damping in the core and shell for the shell-doped and core-doped series 115

Figure C4: STEM images and size histograms for samples made for dielectric sensitivity measurements for core-doped, uniformly-doped, and shell-doped ITO 116
Figure C5: Experimental and simulated graphs for changes to optical response with a changing surrounding refractive index 117

Chapter 1: Introduction

1.1 Motivation

Our growing understanding of light-matter interaction has led to the development of truly revolutionary technologies. One of the clearest examples is that of the solar cell. The sun constantly bathes our planet with solar energy and without Albert Einstein's explanation of the photoelectric effect, we would have no idea how to transduce that energy into useful electrical energy. Light-matter interaction, though, is not limited to light from the sun. Light, more broadly, is an electromagnetic wave that can travel through space with a variety of wavelengths (Figure 1.1).[1] Another crucial technology enabled by studying

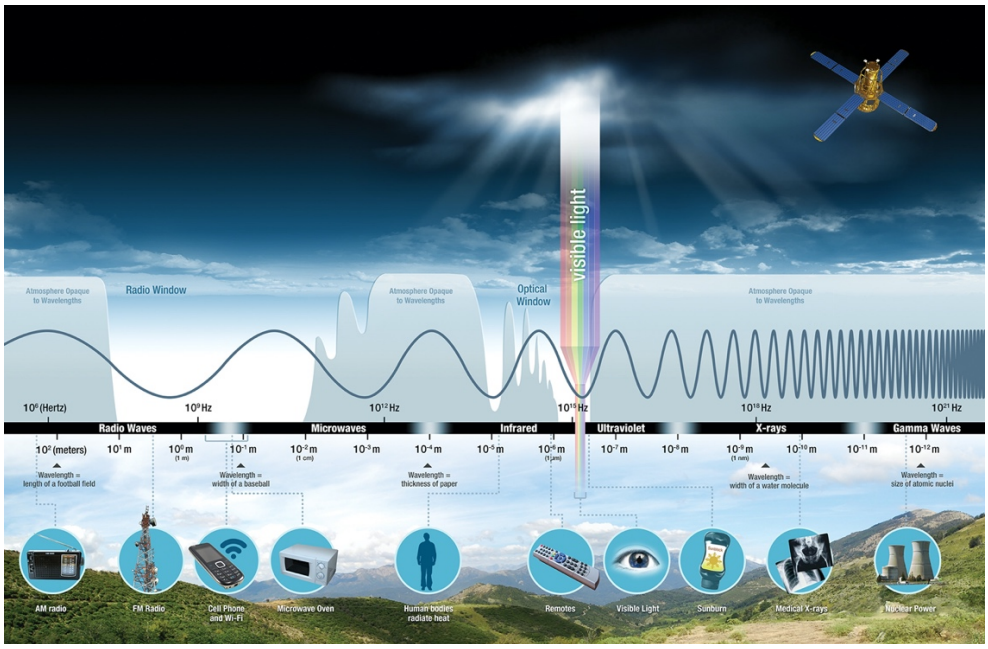

Figure 1.1: Wavelength regimes of the electromagnetic spectrum. Reproduced from Ref 1.

light-matter interaction is that of the radio. Local production of electromagnetic waves and subsequent transmission to a distant receiver opened the door to rapid communication across the globe.

Today, the development of technology involving light-matter interaction is ongoing and the potential impacts are every bit as disruptive as in the past. A particularly promising pursuit in this area is that of plasmon-enhanced processes. Plasmonic nanoparticles absorb incident electromagnetic energy in the oscillations of their freely moving charge carriers which are confined to nanoscopic volumes. Much like using a magnifying glass to concentrate solar energy to a point and start a fire, plasmonic nanoparticles can capture incident electromagnetic waves and concentrate that energy to create enhanced electric fields, localized heating, and even promote catalytic reactions. The capture and confinement of energy dubs these nanoparticles as "nanoantennas" because just like a radio antenna captures radio waves, these nano-sized particles can capture electromagnetic waves of various wavelengths and concentrate their energy by localizing it to the particle itself and the nearby area.

The capture and transduction of electromagnetic energy through plasmonic nanoparticles has resulted in stunning progress of "plasmon-enhanced processes." In the field of biomedicine, gold nanoshells have been aggregated in tumors and irradiated with near-infrared light to raise the local temperature and kill cancer cells.[2] Plasmonic nanoparticles have also proven to be successful photocatalysts to drive multi-electron reduction of CO_2 to produce hydrocarbons,[3] a crucial step in pushing forward artificial photosynthesis. Moreover, plasmonic particles are ubiquitous in the sensing community. They have not only shown sensitivity to changes in protein conformation[4] but have also illustrated heat detection in hopes of being deployed as early-stage forest fire alarms.[5]

These plasmon-enhanced processes exemplify just a handful of the possibilities enabled by plasmonic particles. While the results are promising, there is still very little commercial application of these materials. Thus, there remains ample opportunity to explore new plasmonic materials and probe for fundamental understanding that can continue to push these materials to commercial relevance and open the door to new application areas.

The plasmonic materials used in each application listed so far have been precious metals, such as gold or silver. Doped semiconductor nanocrystals (NCs) are an emerging plasmonic material class. In addition to being a generally more abundant material class, doped semiconductors are (i) particularly effective operating in infrared wavelengths, (ii) open up a new library of surface chemistry for promoting catalytic reactions, and (iii) contain charge carriers that are governed by different physical mechanisms which can translate to new energy transduction pathways. In my thesis work, I've explored the viability of this material class as an effective plasmonic material. To do so, I developed and carried out careful synthetic and quantitative spectroscopic techniques which unveiled a rich physical understanding of how the nonuniform charge carrier concentration within a doped semiconductor NC significantly impacts its optoelectronic properties.

1.2 Fundamental Concepts

Here, I've outlined the theory behind the most essential concepts that underpin the bulk of my research. While each section only skims the surface of each topic, I anticipate that reading through them and gleaning some familiarity will significantly enhance the reader's ability to follow my procedures and conclusions.

1.2.1 The Dielectric Function of a Metal

Science and engineering students should be familiar with a material property known as the dielectric constant, i.e. the electric permittivity. It's a measure of how readily a material is polarized when subjected to an external electric field. Polarizability refers to a material's ability to redistribute charge when placed in an electric field and it is measured in terms of polarization density, P. The manner in which P scales with the electric field, E, is dependent on the material's electric susceptibility, χ

$$P = \varepsilon_0 \chi E \qquad \text{Equation 1.1}$$

where ε_0 is the permittivity of vacuum. The electric susceptibility is related to the relative electric permittivity, ε, in the following way

$$\chi = \varepsilon - 1 \qquad \text{Equation 1.2}$$

Combining these two equations we can see how the electric permittivity relates the electric field to the polarization density

$$P = \varepsilon_0 (\varepsilon - 1) E \qquad \text{Equation 1.3}$$

Therefore, if we know the relative electric permittivity of the material, ε, we can predict it's polarization density under a given electric field. This is a rather straightforward measurement for a static electric field. Take a parallel plate capacitor. When a dielectric material is placed in between two metal plates (Figure 1.2)[6] and a voltage, V, is applied,

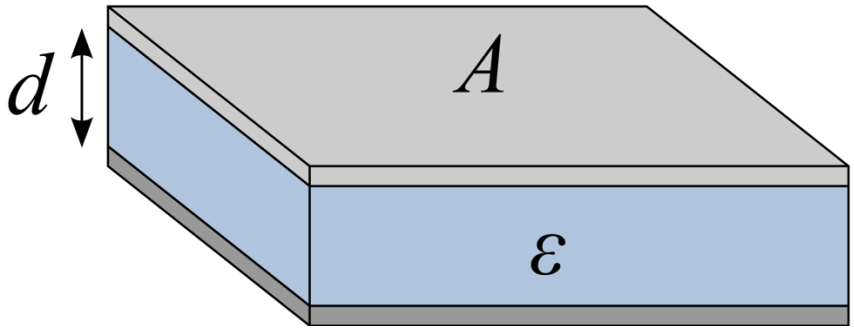

Figure 1.2: A parallel plate capacitor. Two metal plates of area $\boldsymbol{A}$ are separated by a dielectric material of electric permittivity $\boldsymbol{\varepsilon}$ and thickness $\boldsymbol{d}$. Reproduced from Ref 6.

there will be charge build-up, Q, on the metal plates and the relative electric permittivity can be calculated:

$$\varepsilon = \frac{Qd}{VA}\frac{1}{\varepsilon_0} \qquad \text{Equation 1.4}$$

From Equations 1.3 and 1.4 we can well-describe the response of a dielectric material to a static electric field. However, to describe how light interacts with matter, we need to understand how matter interacts with a *time-varying* electric field, $E(t)$.

There are many phenomena which can contribute to the overall polarization of a material. Some of the principal phenomena in solids are the reorganization of ions, ε_{ions}, the motion of electrons, ε_{drude}, and the excitation of electronic transitions to new energy states, $\varepsilon_{transition}$. The dominance of any one of these processes over another in contributing to the overall polarization is heavily-dependent on the frequency of the time-varying electric field. In other words, the electric permittivity is frequency-dependent. We can independently sum these different contributions to arrive at the overall relative electric permittivity

$$\varepsilon(\omega) = \varepsilon_{ions}(\omega) + \varepsilon_{drude}(\omega) + \varepsilon_{transition}(\omega) \qquad \text{Equation 1.5}$$

Now that we have written out the dielectric "constant" as a function of frequency, from this point on, I will refer to this property as the dielectric *function*. Further, the plasmonic response of nanoparticles is driven by the motion of their free electrons; therefore, to characterize the response to light, I will assume $\varepsilon(\omega) \approx \varepsilon_{drude}(\omega)$. Before deriving the polarization of free electrons in response to incident light, let's consider how electrons behave in a metal and what exactly is a "free electron."

When metal atoms condense together to form a solid, electrons can be divided into two categories: core and conduction electrons. Core electrons are *localized* near metal atoms. One might say they "belong" to a particular atom. Whereas conduction electrons are *delocalized* or "shared" equally by all metal atoms in the solid. Because conduction electrons are shared throughout, they can easily move across macroscopic distances. These are the electrons that contribute to electric current. In 1900, Paul Drude developed a theory for modelling the motion of conduction electrons that was based on the kinetic theory of gases.[7,8] I refer the reader to *Solid State Physics*, written by Aschroft and Mermin, for a wonderfully complete description of this theory.[9] In short, electrons of mass, m, are treated as particles occupying an incompressible volume. They are driven into motion when an external electric field exerts a force on them. They experience collisions with a frequency of γ, known as the damping or scattering frequency. It is not essential to define the exact cause of the collision, but rather to define that all collisions instantaneously change the velocity of the electron while conserving momentum. In the most basic form of Drude theory, the particles are deemed "free electrons" because in this approximation, the electromagnetic interaction of the electrons with one another and with the metal ions of the solid are neglected. Essentially, electrons are treated as particles in an "electron gas."

To derive the polarization caused by this incompressible electron gas in response to incident light, a force balance according to Newton's Second Law is set up

$$m\frac{\delta^2 x}{\delta t^2} + m\gamma\frac{\delta x}{\delta t} = -qE(t) \qquad \text{Equation 1.6}$$

where the force applied, $-qE(t)$, drives the displacement, x, of electrons of mass m. The change in momentum, $m\gamma\frac{\delta x}{\delta t}$, is determined by the frequency of electron scattering, γ, and the velocity $\frac{\delta x}{\delta t}$. If we assume a harmonic time-dependence of the incident field with some amplitude E_0 and frequency ω

$$E(t) = E_0 e^{-i\omega t} \qquad \text{Equation 1.7}$$

that function can be incorporated into Equation 1.6 and Fourier-transformed to result in the following:

$$m(-i\omega)^2 x + m\gamma(-i\omega)x = -qE_0 \qquad \text{Equation 1.8}$$

Solving for x results in a function for the average displacement of electrons as a function of frequency of the incident electric field.

$$x = \frac{qE_0}{m(\omega^2 + i\gamma\omega)} \qquad \text{Equation 1.9}$$

How does this relate to the dielectric function? The average displacement of the electrons in the free electron gas can be visualized in Figure 1.3.

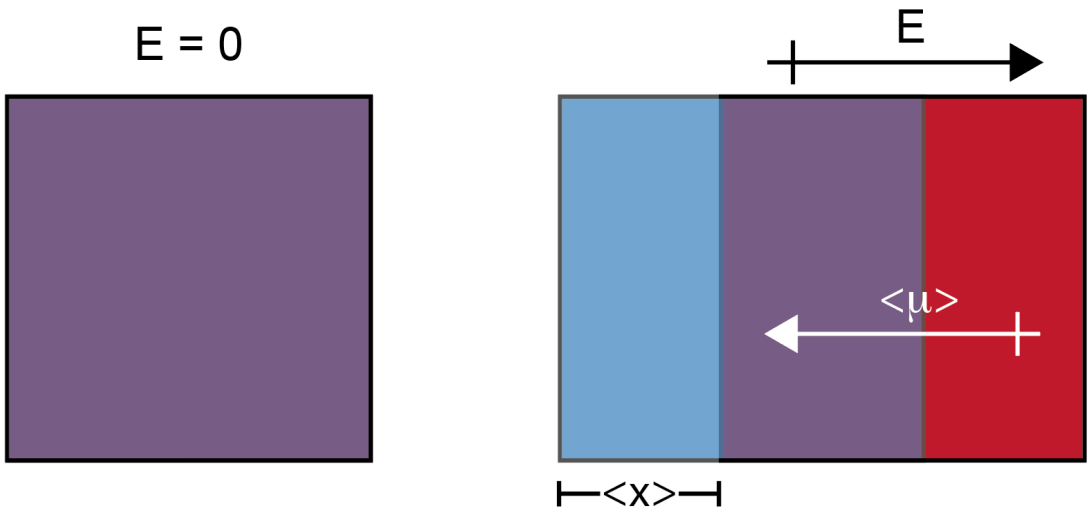

Figure 1.3: The incompressible electron gas (blue) is displaced from the solid metal (red) by an average distance $\langle x \rangle$ when an external electric field is applied. The displacement creates a macroscopic dipole moment $\langle \mu \rangle$ in the opposite direction of the applied field.

The macroscopic dipole moment, $\langle \mu \rangle$, created by the displacement of electrons can be interpreted as a polarization density, P, when multiplied by the concentration of free electrons.

$$P = \langle \mu \rangle n_e = -qxn_e \qquad \text{Equation 1.10}$$

Combining Equations 1.10 and 1.3 results in a dielectric function for a metal

$$\varepsilon(\omega) \approx \varepsilon_{drude}(\omega) = 1 - \frac{\omega_p^2}{\omega^2 + i\gamma\omega} \qquad \text{Equation 1.11}$$

where the plasma frequency is defined as

$$\omega_p = \sqrt{\frac{n_e q^2}{\varepsilon_0 m}} \qquad \text{Equation 1.12}$$

In order to correct for residual polarization of the metal ions in the background of the electron gas, an additional contribution to the polarization density is included, known as the high frequency dielectric constant, ε_∞.

$$P = \varepsilon_0(\varepsilon_\infty - 1)E \qquad \text{Equation 1.13}$$

When ε_∞ and ε_{drude} are incorporated together, it produces the widely used form of the dielectric function for metals

$$\varepsilon(\omega) = \varepsilon_\infty - \frac{\omega_p^2}{\omega^2 + i\gamma\omega} \qquad \text{Equation 1.14}$$

Much of this proof was gleaned from a more detailed version which can be found in the online textbook, *Plasmonics: Fundamentals and Applications*.[10]

1.2.2 Absorption and Scattering by a Sphere

One of the few analytical solutions there are to light interacting with particles is that of light with a sphere of arbitrary radius and known dielectric function. While it is not clear who was the first to derive this solution, Gustav Mie certainly holds claim to one of the earliest and most well-known derivations in 1908 as he sought to understand the color of small, colloidally dispersed gold particles.[11] Knowing that, one might guess that gold changes color when in its small particle form – they would be correct. Take one of the oldest and best-known examples of this: the Lycurgus cup (Figure 1.4).[12]

Figure 1.4: The different colors of the Lycurgus cup when light is predominantly shining through it from the back (left, red) or being reflected off the front (right, green). Photograph credit: Johnbod – Own work, CC BY-SA 3.0

The red and green colors of this cup result from the optical response of light interaction with nanoscale gold and silver particles – clearly not exhibiting the typical gold and silver colors! This phenomenon can be explained by classifying what can happen to light incident upon a sphere into three broad categories: transmission, absorption, and scattering (Figure 1.5). Transmitted light passes through the material without any interaction. Absorbed light transduces photon energy into *nonradiative* processes – typically resulting in the heating of the particle. Scattered light describes photons that have been redirected and *radiated* outward from the particle to continue on as propagating electromagnetic waves.

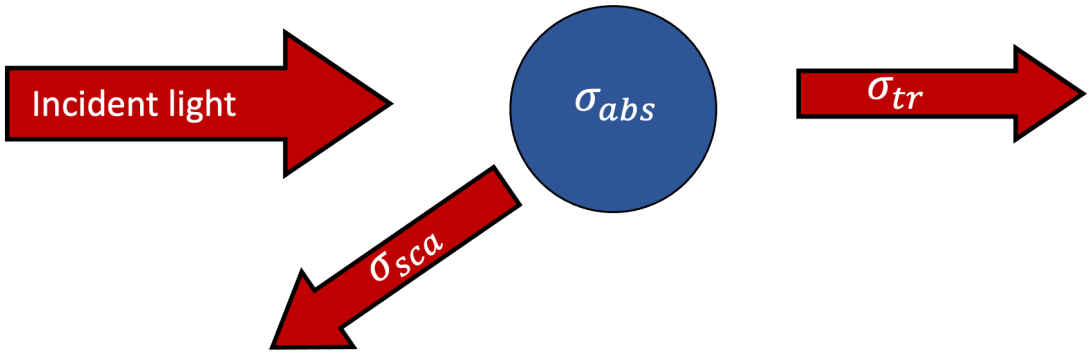

Figure 1.5: The amount of light that is either transmitted, absorbed, or scattered when interacting with a particle is defined by its transmission, σ_{tr}, absorption, σ_{abs}, and scattering, σ_{sca}, cross-sections

By solving Maxwell's equations, Mie arrived at a solution for the absorption, $\boldsymbol{\sigma_{abs}}$, and scattering, $\boldsymbol{\sigma_{sca}}$, cross-sections of a spherical particle of arbitrary size – given that the dielectric function of the particle, $\boldsymbol{\varepsilon_p}$, is known.

$$\sigma_{abs}(\omega) = 8\pi^2 r^3 \omega \sqrt{\varepsilon_H} Imag\left\{\frac{\varepsilon_p - \varepsilon_H}{\varepsilon_p + 2\varepsilon_H}\right\} \qquad \text{Equation 1.15}$$

$$\sigma_{sca}(\omega) = 64\pi^5 r^6 \omega^4 {\varepsilon_H}^2 \left|\frac{\varepsilon_p - \varepsilon_H}{\varepsilon_p + 2\varepsilon_H}\right| \qquad \text{Equation 1.16}$$

$$\sigma_{ext}(\omega) = \sigma_{abs}(\omega) + \sigma_{sca}(\omega) \qquad \text{Equation 1.17}$$

Here, ε_H is the dielectric constant of the host material (the surrounding environment), r is the radius of the particle, and ω is the frequency of incident light.* The sum of absorbed and scattered light is known as extinguished light – it consists of any light that is not transmitted. The extinction cross-section, σ_{ext}, is often reported when the experimental setup only measures transmitted light and therefore cannot distinguish between what light may have been absorbed or scattered by the particle.

These equations can be represented in many different ways, but this form of the cross-sections is very common ("cross-section" because the units are in fact, length^2, as is the case for a cross-sectional area). However, I find it helpful to simply think of the cross-section as reporting on how efficiently or strongly a material absorbs or scatters light, e.g. a particle with a high σ_{abs} will absorb a lot of light. Much of the intuition explained in this section is derived from a text that goes into much more detail on absorption and scattering by small particles.[13]

1.2.3 Localized Surface Plasmon Resonance

Having now understood how free electrons contribute to the dielectric function (Section 1.2.1) and how light interacts with spherical particles (Section 1.2.2), we now have the tools we need to study localized surface plasmon resonance (LSPR). When electromagnetic radiation is impingent upon metallic particles, it drives the collective motion of free electrons to oscillate at a resonant frequency known as the localized surface plasmon resonance (LSPR) frequency, ω_{LSPR}. We can gain a physical picture of this system by imagining an incompressible free electron gas, oscillating to the tune of the incident

*These equations may look slightly different than those commonly reported in literature. Most variation comes from the units used for frequency. In my case, I've opted to use linear wavenumber. Wikipedia has a very helpful graphic that I often refer to in order to unjumble the mess of units regarding the frequency of light: https://en.wikipedia.org/wiki/Wavenumber

electric field (Figure 1.6). This system has a resonant frequency comparable to any classical physics model for periodic motion, such as a mass on a spring.

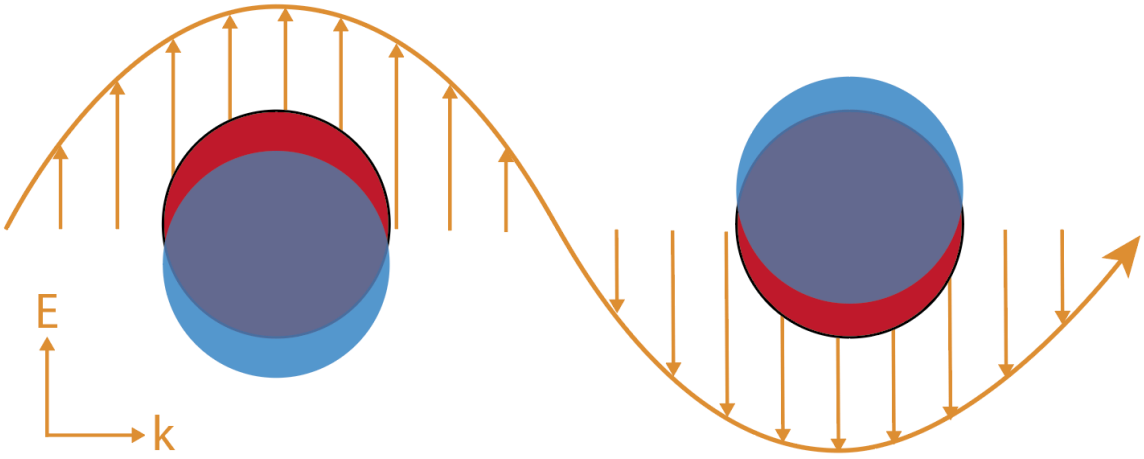

Figure 1.6: Schematic depicting localized surface plasmon resonance. The incident electromagnetic wave (orange) drives the oscillation of the freely moving cloud of electrons (blue) displacing them from the core of metal ions (red).

The position of ω_{LSPR} is dependent on a variety of factors, chief among them are the concentration of free electrons, n_e, the frequency of damping of those electrons, γ, and the host dielectric environment, ε_H. These factors are directly tracked when we plug in our equation for the dielectric function for metals into the scattering and absorption cross-sections derived from Mie theory. In plotting σ_{abs} and σ_{sca} for a plasmonic particle of $n_e = 6 \times 10^{20} cm^3$, $\gamma = 1200 cm^{-1}$, and $r = 10\, nm$, we see a strong absorption peak occur near 4000 cm^{-1}, or 2500 nm (Figure 1.7A). This is ω_{LSPR} wherein the oscillations of free electrons within the material are most efficiently absorbing incident light.

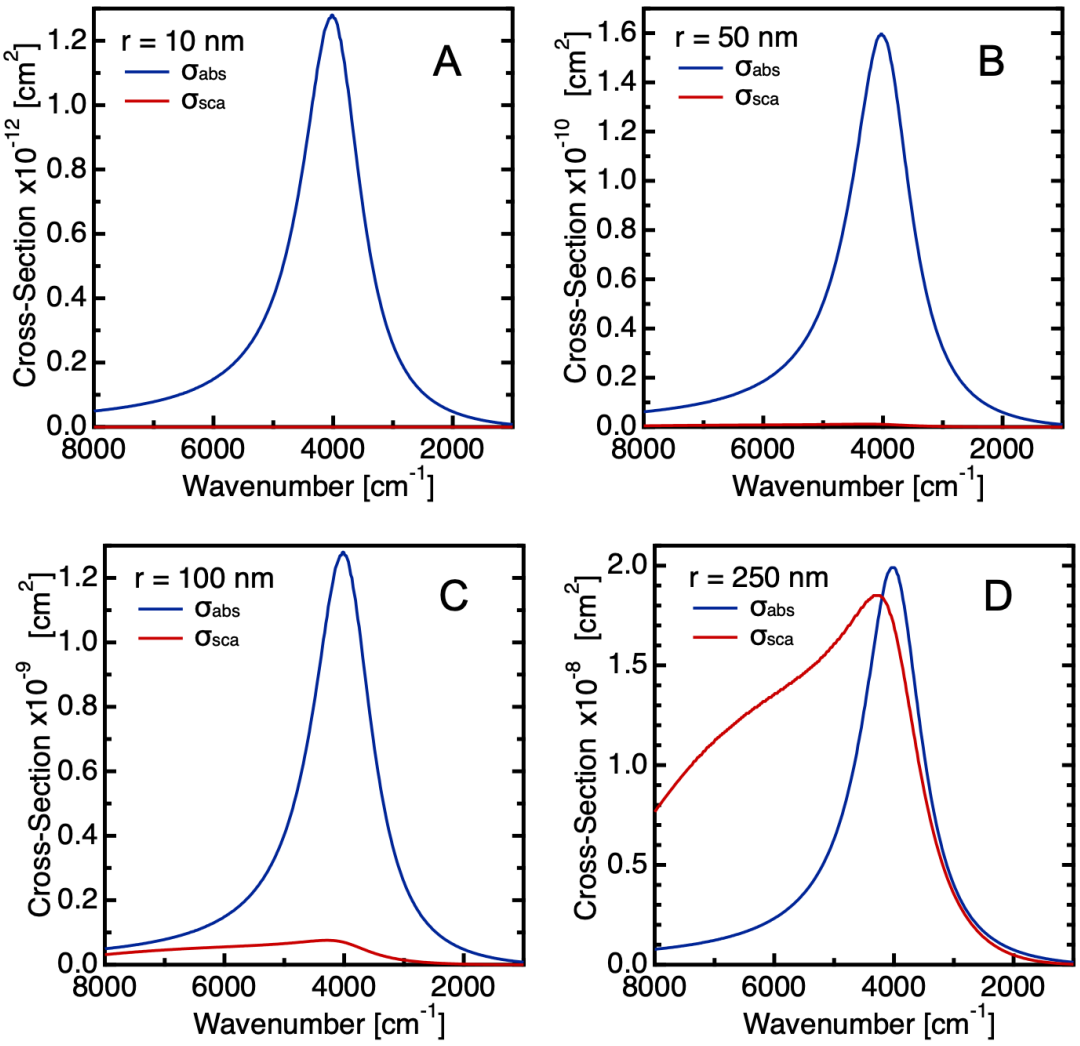

Figure 1.7: Absorption and scattering cross-sections calculated based on Mie theory equations for plasmonic spheres of radius (A) 10 nm, (B) 50 nm, (C) 100 nm, and (D) 250 nm.

Notice that at this size $\sigma_{sca} \approx 0$. As we run the Mie theory calculations for increasing size, it is not until the sphere reaches a radius of approximately 100 nm that the scattering signal is of the same order of magnitude as the absorption signal. This is generally the case for plasmonic particles. For particles $r < \frac{\lambda_{LSPR}}{25}$ it is generally safe to neglect the scattering component and assume all extinction comes from absorption.

$$if\ r < \frac{\lambda_{LSPR}}{25}, then\ \sigma_{ext}(\omega) \approx\ \sigma_{abs}(\omega)$$ Equation 1.18

For my work, the particle radii stay below ~15 nm and λ_{LSPR} never falls below ~1650 nm, so it is safe to assume scattering is negligible and absorption is equal to extinction. For this reason, extinction and absorption are often used interchangeably in my work.

It is this polarization of electrons, resulting in the strong absorption of incident light, that enables plasmonic particles to act as nanoantennas that efficiently capture and confine incident electromagnetic energy into nanoscopic volumes. The degree to which energy is concentrated then is dependent on the size of the nanoparticle and the wavelengths of light that are absorbed, which is determined by ω_{LSPR} of the nanoparticle. Throughout my thesis, I've focused on the synthetic development and optical characterization of an emerging class of plasmonic nanoparticles that allows for wide tunability of both nanoparticle radius and ω_{LSPR}: doped semiconductor NCs. In particular, I've focused on a library of semiconductors with large band gaps and relatively strong air stability known as metal oxides.

1.2.4 Doped Metal Oxide Nanocrystals

Metal oxides are known in the electronics and optics community for their semiconducting electrical properties as a result of large (>3eV) band gaps. They are also known to stabilize intrinsic defects and incorporate extrinsic dopant atoms to widely tune that conductivity – to even reach metallic conductivity. This property gives doped metal oxides the label of transparent conducting oxides (TCOs) due to their unique capability to maintain visible transparency (due to their large band gap) but sustain high conductivity. This makes them desirable materials for smart window coatings, solar cell conductive contacts, and touchscreens. In fact, it is likely you are staring through a TCO in order to read this dissertation.

When synthesized in nanocrystal form, doped metal oxides sustain sufficient electron concentration, n_e, to promote LSPR. This ushers in the material class known as semiconductor plasmonics. This name is somewhat of an oxymoron given that we know LSPR can only occur in materials behaving as metals. These unique properties can be understood with the rich physics underlying these solids.

1.2.4.1 Electronic Band Structure of Semiconductors

In general chemistry we learn that the electron configuration of a sodium atom is $1s^2 2s^2 2p^6 3s^1$. This means there are 2 electrons in the 1s orbital, 2 electrons in the 2s orbital, 2 electrons in each of the three 2p orbitals (so 6 total in 2p orbitals), and 1 electron in the 3s orbital. The first number (principal quantum number) denotes the energy level and the letter (angular momentum quantum number) denotes the orbital shape. According to the Pauli exclusion principle, no two electrons can occupy the same quantum state within a single quantum system simultaneously. In terms of orbitals, that means orbitals can only hold two electrons (one "spin up" and one "spin down"). In sodium, only one orbital is partially filled, 3s. Electrons in lower energy, filled orbitals are known as core electrons and they tend not to participate in bonding or chemical reactions, but stay *localized* on the atom, whereas electrons at higher energy levels, near partially-filled orbitals are known as valence electrons and are much more reactive/mobile. They form bonds and are shared between atoms i.e. are *delocalized* among multiple atoms. So, what happens when atoms come together to form bonds and make a macroscopic solid?

For bonds to form, i.e. electrons to be shared between atoms, atomic orbitals must come together to form molecular orbitals that are spread across multiple atoms. For bonding in a macroscopic solid (think Avogadro's number: 6×10^{23} atom), many of the "molecular orbitals" that form are so closely spaced in energy that it is actually more

accurate to describe them as a continuous band of energy levels. Hence, instead of simply forming more and more molecular orbitals, atomic orbitals form into *bands* in solids. Bands formed from atomic orbitals constitute the *electronic structure* of solids. The electronic structure of sodium is illustrated with changing interatomic distance to show how the broadening of atomic orbitals into bands increases as interatomic distance decreases (Figure 1.8).[14] The true bond length in sodium solid is indicated by the vertical dashed line. At this interatomic spacing, the core orbitals (2p and below) remain at a single energy level. This indicates that electrons which populate those orbitals remain in isolated, localized atomic orbitals because they do not participate in bonding. The higher energy orbitals, in contrast, have broadened into bands that span a range of energy levels. Electrons that were in the atomic 3s orbital now belong to the valence band.

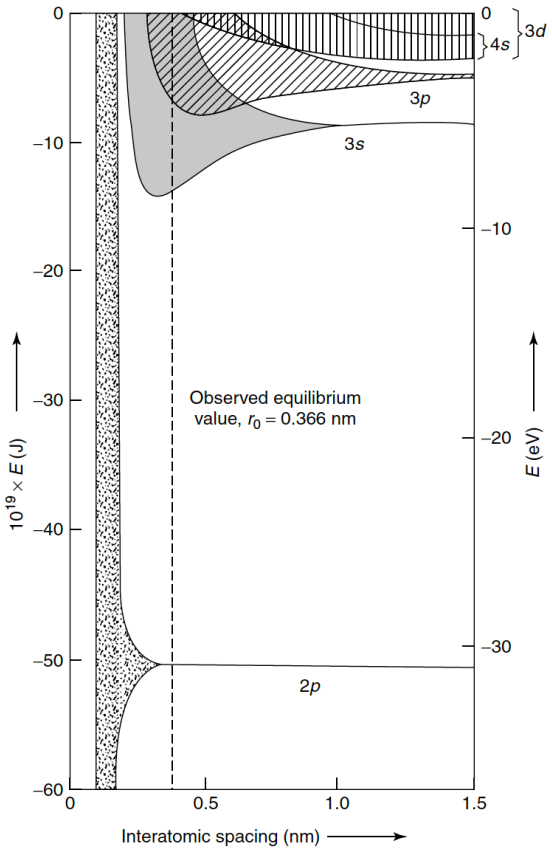

Figure 1.8: Electronic structure of sodium as a function of interatomic spacing. The dashed line indicates the actual bond distance in sodium solid. Reproduced from Ref 14.

Any orbitals that are higher energy than the valence band will also come together to form a band known as the conduction band. This is where the principal difference between metals, semiconductors, and insulators arises. Let's take two imaginary materials of fixed interatomic distance and plot their valence and conduction bands. Figure 1.9 is a very common plot to show the energetic position of the highest energy bands. The shading indicates whether or not those bands are occupied with electrons. Think of this plot as taking a vertical slice of Figure 1.8 at the dashed line. The x-axis doesn't have any significance. All that is important is the y-axis (energy level) and the shading (occupation of that energy level with an electron).

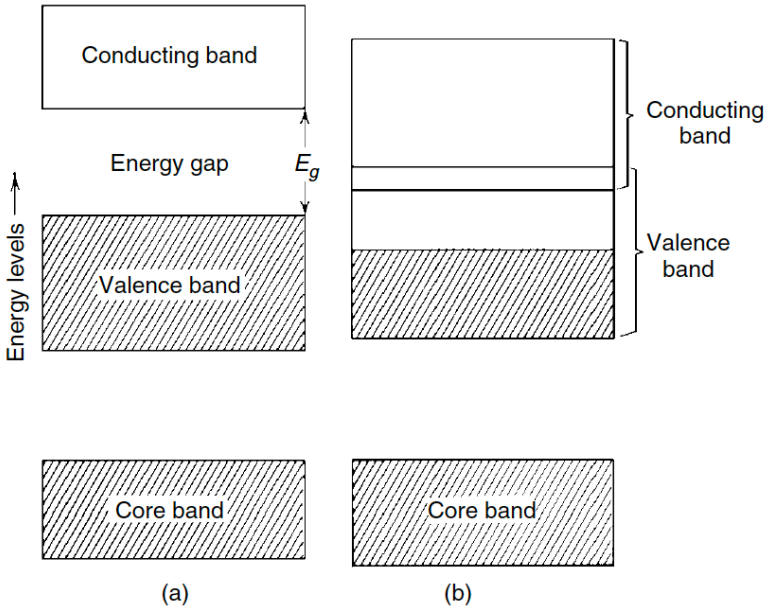

Figure 1.9: Electronic band structure of a typical semiconductor (a) and metal (b). Shading indicates occupation of band with electrons. Reproduced from Ref 14.

In metals, the highest energy band remains partially filled. This is often a consequence of overlapping (degenerate) valence and conduction bands (Figure 1.9b). When the highest energy band remains partially filled, electrons are able to be excited into motion even with an infinitesimally small amount of energy. This is why only a small applied voltage is required to promote current in a metal wire. However, if the valence band is completely filled and there is an "energy gap" before the next available energy state (Figure 1.9a), then a lot more energy must be applied before any electron can become mobile. In other words, a much higher voltage would need to be applied to generate current from a material with an energy gap, or *band gap*.

There is a theoretical framework that can help us determine the probability of electronic states being populated within a band structure for particles obeying the Pauli

exclusion principle, i.e. fermions: the Fermi-Dirac distribution. This theory defines the probability, f, that an electronic state of energy, E , is populated at a given temperature, T.

$$f(E) = \frac{1}{\exp\left[(E - E_f)/k_B T\right] + 1} \qquad \text{Equation 1.19}$$

Here, k_B is the Boltzmann constant and E_f is the Fermi level. The Fermi level falls at the energy of the highest electron when the system is at zero Kelvin (Figure 1.10a). An equivalent description of the Fermi level is that it defines the point of 50% occupation probability, at any temperature (Figure 1.10b).

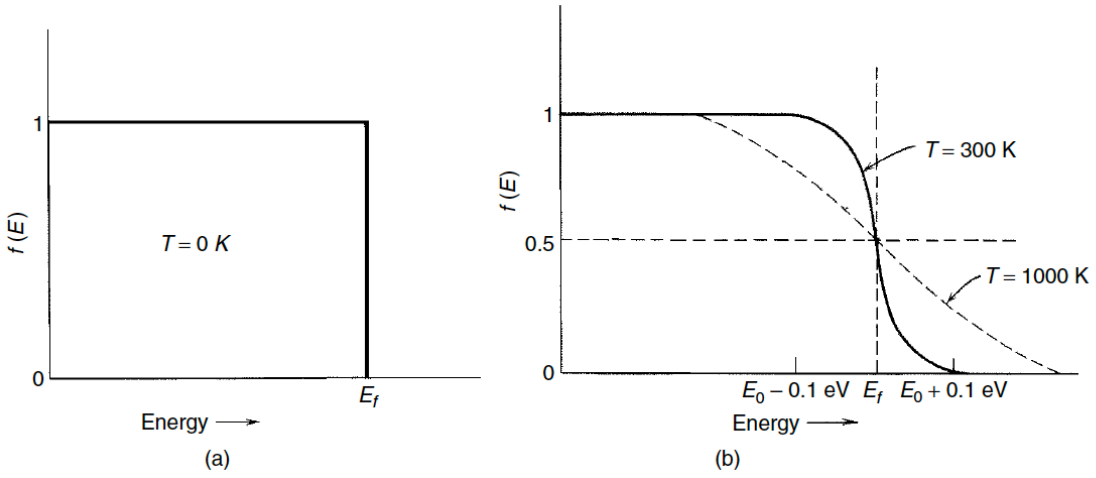

Figure 1.10: The Fermi-Dirac distribution at (a) zero Kelvin and (b) finite temperature. Reproduced from Ref. 14.

Electrons that occupy states in the conduction band are free, mobile electrons that can contribute to current. Hence, we can get a good estimate of the free electron concentration of metals if we know the position of the Fermi level. Simply multiply the probability of occupying states in the conduction band, f, by the number of states at that

energy (this function is known as the density of states, N) and integrate from a reference zero point energy to the Fermi level.

$$n_e = \int_0^{E_f} N(E) \cdot f(E) dE \qquad \text{Equation 1.20}$$

In metals, the Fermi level falls within the conduction band, whereas with semiconductors it falls between the valence and conduction bands, in the band gap. Hence there is very low probability of occupying electronic states in the conduction band for semiconductors. This gives us a new way of thinking about something we already knew: semiconductors are less conductive than metals. But now we can use this new way of thinking to manipulate the properties of the semiconductor… Instead of asking, "how can we raise the conductivity of a semiconductor?" we can ask a more pointed question, "how can we raise the Fermi level in semiconductors?"

1.2.4.2 Doping and Defect Chemistry

In order to raise the Fermi level in semiconductors, we can incorporate defects that donate electrons to the conduction band. These types of defects are called n-type or donor defects. For a dopant to be effective, it first needs to be similar enough to the host atom in terms of ionic radius and electronegativity to be able to actually replace it. In the case of my work, I studied tin-doped indium oxide (often written as Sn:In_2O_3 or ITO). Being right next to indium on the periodic table, Sn is similar in size and electronegativity to In and therefore it is easily incorporated.

For the dopant to act as a donor it must (1) have an additional valence electron in comparison to the host atom and (2) have a donor energy level, E_D, that is near the conduction band minimum, E_C. Sn has four valence electrons while In has three. By

replacing In with Sn, we've added on additional electron in comparison to undoped In_2O_3. The question then becomes if this electron ends up in the conduction band and therefore raises E_F and contributes to the concentration of free electrons, n_e. To answer this question, we must know where the energy level of the dopant's valence electron (known as the donor energy level, E_D, lies with respect to E_C (Figure 1.11) . As mentioned in the prior section, for an electron to contribute to current in a semiconductor it first needs to overcome the band gap energy, E_g. Dopants provide a source of electrons much closer to E_C such that much less energy is required for them to be excited into the conduction band and contribute to n_e.

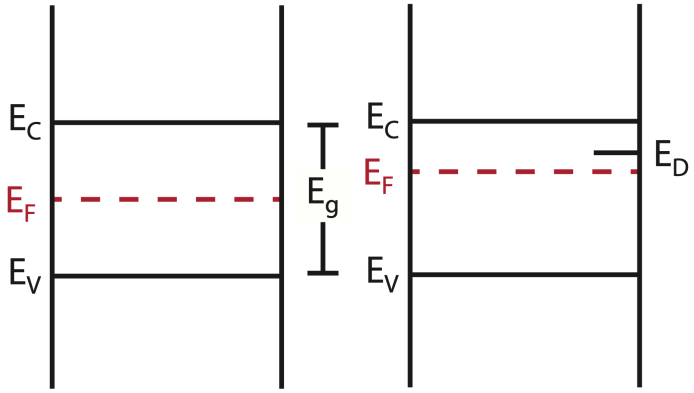

Figure 1.11: Energy level diagrams for an undoped (left) and doped (right) semiconductor. E_F: Fermi level, E_C: conduction band minimum, E_V: valence band maximum, E_g: band gap, and E_D: donor energy level.

The closer the donor energy level comes to E_C and the higher density of incorporated dopants, the more we would expect n_e to increase. This process can be tracked by the shifting of E_F in the Fermi-Dirac distribution. As more dopants are incorporated, E_F shifts to higher energies. At finite temperatures this distribution predicts the probability that states above and below E_F are populated with electrons. We can visualize the increase

in electrons by integrating the area under the Fermi-Dirac curve within the conduction and valence bands (Figure 1.12).

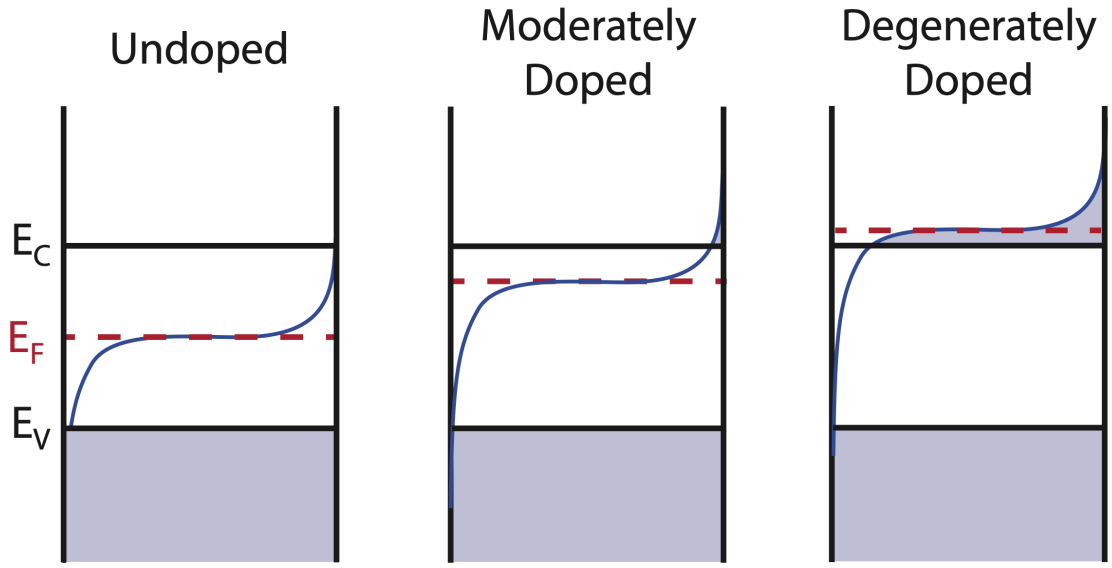

Figure 1.12: Energy level diagrams for an increasingly n-type doped (left to right) semiconductors. An approximate Fermi-Dirac distribution near room temperature is overlayed (solid blue line). Shading indicates states within the bands that are populated with electrons. A semiconductor is said to be "degenerately doped" when E_F rises above E_C.

A directly analogous process can be performed for p-type dopants. In this case, the dopants are referred to as acceptors and the acceptor energy levels are engineered to be near E_V. This makes it easier for electrons to be promoted from the valence band to the acceptor energy level which leaves available states within the valence band for electrons to move around. This motion is described as the movement of electron "holes", which have the same magnitude of charge as an electron, just positive in sign. It is for this reason that conductivity in semiconductors is dependent on "charge carrier concentration". Holes are positive charge carriers whereas electrons are negative charge carriers. Electrons can contribute to current within the conduction band whereas holes can contribute to current in the valence band.

In order to track charge balance while incorporating defects, Kroger-Vink notation was developed. The replacement of an In atom with a Sn atom can be written in this notation as

$$null \iff Sn_{In}^{\cdot} + e' \qquad \text{Equation 1.21}$$

Where the Sn indicates the present atom in the lattice, the subscript In indicates the host lattice position that the dopant occupies, and the superscript dot or dash indicate the positive or negative charge that results, respectively. Because Sn^{4+} has one additional positive charge than In^{3+} it requires the presence of an electron, e, to balance the charge. Extrinsic donor atoms such as Sn are a very common defect for metal oxides, as are vacancies and interstitial defects. For indium oxide, not all oxygen sites are actually filled with oxygen. A vacant oxygen site can also grab compensating electrons

$$null \iff V_O^{\cdot\cdot} + 2e' \qquad \text{Equation 1.22}$$

As well, oxygen can place itself in places where there are no true lattice sites in In_2O_3. This would be called an interstitial defect and it can prevent the generation of electrons from Sn dopants in In_2O_3 by compensating charge and forming a neutral defect cluster composing two Sn atoms and an interstitial oxygen

$$null \iff 2Sn_{In}^{\cdot} + O_i'' \qquad \text{Equation 1.23}$$

Thus, defects can both work for and against us in generating charge carriers. It is an essential observation, though, to realize that defects within a material can actually result in the properties that are overall dominant in the performance. Keeping track of defect chemistry is crucial for doped metal oxide NCs and it is often dependent on the synthetic conditions.

1.2.4.3 Colloidal Synthesis

A colloid is a liquid which contains non-dissolvable units that are evenly mixed throughout and remain evenly mixed, i.e. do not settle, in perpetuity. Thus the defining feature between a stable colloidal dispersion and a suspension is the duration that the non-dissolvable units stay evenly mixed. There are many benefits to synthesizing doped metal oxides as colloidal NCs as opposed to more traditional methods that synthesize them by growing films on substrates inside of high vacuum chambers at high temperatures. For one, colloidal synthesis can be carried out at lower temperatures and at ambient pressure – lowering the complexity and intensity of the synthetic conditions.

Secondly, a dispersion of NCs can act as an electronic ink, which opens up a wide array of deposition techniques. By dropcasting, spin coating, spray coating… we can deposit these NCs onto flexible substrates, allow the solvent to dry, and then harness their optoelectronic properties as coatings to make "smart" materials such as infrared-blocking windows, color changing fabric, and flexible solar cells.

Lastly, by synthesizing doped metal oxides in a solvent, we have a great deal of control over size, shape, and doping. There are crystalline phases and crystallite sizes and shapes that can be achieved in colloidal dispersion that simply cannot be done with high vacuum deposition. Each unique parameter opens the door to a new material property that can benefit performance. For one example, colloidal synthesis of V_2O_3 enabled stabilization of a rare bixbyite phase that exhibits high oxygen storage capacity that is useful in catalytic converters in automobiles.[15]

The most important concepts of colloidal synthesis involve demonstrating control over the nucleation and growth steps. There are two competing thermodynamic forces that drive dissolution and condensation of solids: surface and bulk free energy (Figure 1.13A). The surface energy is a positive contribution to the overall free energy because it is a

destabilizing, unfavorable interaction between solvent and solid, whereas the bulk energy is a negative, stabilizing contribution. At the size where the bulk free energy overcomes the surface free energy in magnitude, the overall free energy begins to decrease with increasing size. In other words, it becomes thermodynamically favorable for monomers to nucleate instead of dissolve.

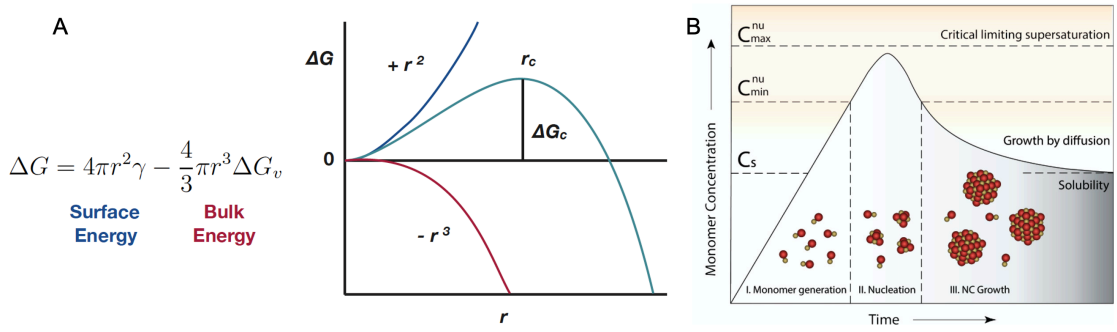

Figure 1.13: (A) Surface and bulk energy contributions to overall free energy. Figure Courtesy of Prof. Delia Milliron Lectures, University of Texas at Austin, CHE 350. (B) LaMer model for nucleation and growth. Adapted from Ref. 16.

The LaMer model utilizes this understanding of free energy to plot out a timeline of nucleation and growth in a typical colloidal nanoparticle synthesis (Figure 1.13B).[16] Nucleation does not occur until the monomer concentration, C, reaches the point that makes bulk free energy dominate surface free energy. At the point of nucleation, monomer condenses into solid and C diminishes. As long as C does not reach Cmin, additional monomer will only grow on existing nuclei instead of nucleating themselves.

Control over nucleation and growth in colloidal synthesis involves careful selection of precursor, solvent, and surfactant. In the case of the syntheses used in my thesis, the precursor is a metal acetate, which starts in the form of a metal powder but can easily be dissolved in the surfactant oleic acid. This precursor solution is slowly injected into a hot solvent, oleyl alcohol (Figure 1.14).

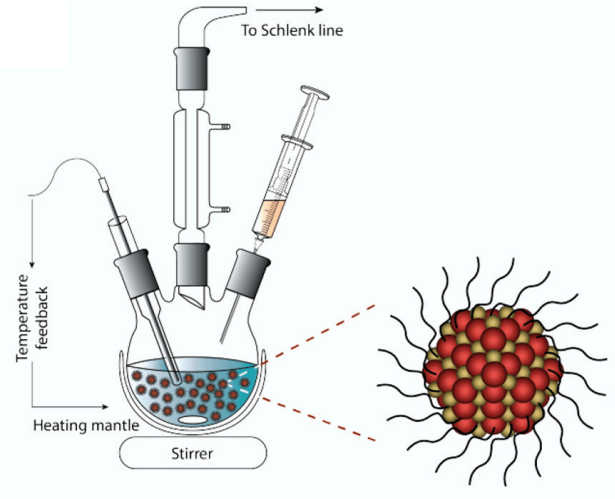

Figure 1.14: Schematic depicting typical setup for slow-injection colloidal synthesis of metal oxide NCs. The surfactant is illustrated as black lines bonded to atoms that make up the nucleated NCs. The solvent is depicted in blue and the slowly-injected precursor in yellow. Adapted from Ref. 16.

1.2.5 Near-Surface Charge Carrier Depletion[†]

While their optical properties show promise for diverse applications, the underlying plasmon physics of doped metal oxide NCs is not as well established as for metal nanoparticles. Though comparable in many ways, the distinguishing properties of doped metal oxide NCs, namely their semiconductor band structure, infrared ω_{LSPR}, and relatively low n_e, demand unique consideration. Of principal importance is the presence of depletion regions near the surface of doped metal oxide NCs. These regions have reduced n_e, even below the limit required for metallic electronic and optical properties (Figure 1.15).[17]

[†]This section contains text and figures adapted from Ref 17, which was written by Stephen L. Gibbs as lead authors in collaboration with Corey M. Staller and Delia J. Milliron. It has been adapted with permission from the authors. Copyright 2019 American Chemical Society

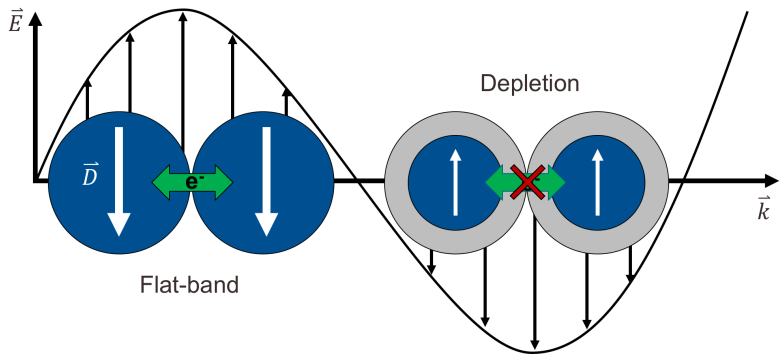

Figure 1.15: When charge carriers are depleted from the NC surface, NCs of high n_e (blue) form insulating shells of low n_e (gray) as charge carriers are depleted from the NC surface. This diminishes the extinction cross-section, weakens the dipole-dipole interactions between nearby NCs, and hinders electron transport in NC films in comparison to the non-depleted (flat-band) case.

Recent work not only confirms the presence of such depletion layers, but also establishes that they form a barrier that insulates the charge carriers from their surroundings, detrimentally effecting the performance. For example, the enhanced electric fields at the NC surface, which are responsible for sensitized spectroscopic detection of molecular vibrations in surface-enhanced infrared spectroscopy (SEIRS), will decay exponentially with depletion layer thickness, reducing sensitivity.[18,19] Moreover, when depletion layer thickness increases, conductivity in NC films diminishes because cores of high n_e are physically separated by a potential barrier that mobile carriers must overcome.[20,21] Neglecting the presence of depletion layers in metal oxide NCs has led to inaccuracies in evaluating intrinsic material properties and has clouded strategies for maximizing performance. To advance the development of doped metal oxide NCs for plasmonic-powered technologies, it is essential to deepen the understanding of their fundamental physical and chemical properties.

Space-charge layers arise at the surface of homogeneous semiconductors because changes to electronic structure arise when lattice periodicity is interrupted and surface

defects are introduced. The interaction between the uncoordinated surface atoms and nearby molecules determines the surface state energy. Space-charge layers (including depletion layers) induced by surface states or an applied surface potential are often assumed to have a spatial extent that far exceeds the radius of a NC. So much so, in fact, that n_e is taken to be independent of distance from the surface. In other words the n_e profile is assumed to be *uniform*. This is a good approximation if the NC is very small and sparsely doped; however, it becomes invalid for heavily doped or larger, moderately doped NCs. To appreciate this, Poisson's equation yields the voltage, ϕ, profile near the surface of a planar electrode (Equation 1.24) where $\rho(x)$ is the position-dependent charge density and ε_S is the relative, static dielectric constant. The built-in potential, E_{BI}, is the difference between the potential far from the surface (i.e. the bulk potential) and the surface potential. For a given E_{BI}, the depletion width, W, is defined by Equation 1.25 at ionized defect density N_d.

$$\frac{d^2\phi}{dx^2} = \frac{-\rho(x)}{\varepsilon_S \varepsilon_0} \qquad \text{Equation 1.24}$$

$$W = \sqrt{\frac{2\varepsilon_S \varepsilon_0 E_{BI}}{eN_d}} \qquad \text{Equation 1.25}$$

Consider a prototypical doped metal oxide: Sn-doped indium oxide (ITO). Taking a dopant concentration of 1 atomic% Sn ($N_d \approx 3 \times 10^{20}$cm^{-3}) and applying a potential difference of 1.0 V, the depletion width is 1.8 nm – a length scale on the order of radius for smaller NCs. The depleted region constitutes a tiny volume fraction in, for example, a ~100 nm thin film electrode, so there is a nearly negligible effect on the total number of free charge carriers – electrons, in this case. By contrast, in an electrode composed of NCs, the depleted regions constitute a large volume fraction of the overall film, meaning the total number of free electrons can be altered dramatically by modulating the surface potential.

While the space-charge width in Equation 1.25 is a reasonable approximation for NC depletion layers, to accurately calculate the number of electrons depleted and the spatial profile of the potential requires solving Poisson's equation in spherical coordinates, which is non-trivial and must be done numerically.[22]

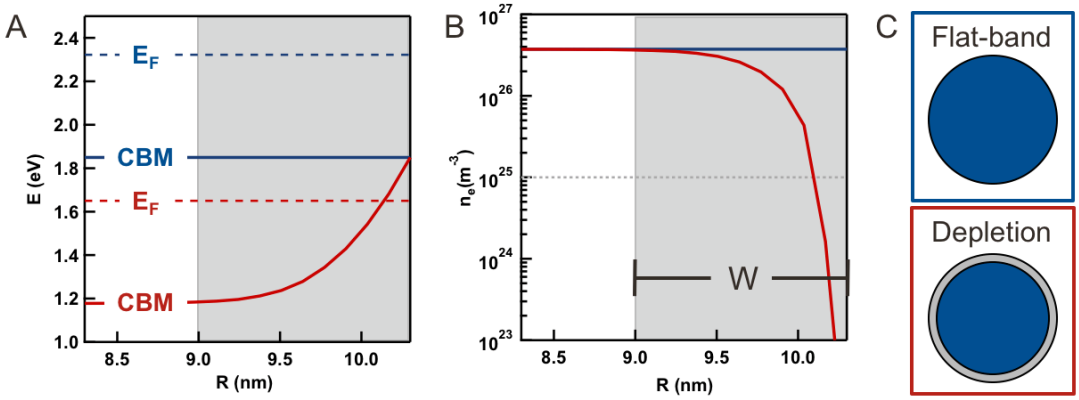

Figure 1.16: Simulated surface depletion in an ITO NC. (A) Simulated intra-NC radial potential profiles for conduction band minimum (CBM, solid lines) and Fermi level (E_F, dashed lines) for a 20.6 nm diameter 3 at% Sn ITO NC when the surface potential dictates flat-band conditions (blue) and depletion conditions (red). (B) n_e profiles at flat-band (blue) and depletion (red) conditions. The dashed gray line denotes the Mott criterion for metallic conductivity in ITO (C) 2D cross-sections of the n_e profiles in panel B at flat-band (top) and depletion (bottom) conditions.

Staller et al numerically solved Poisson's equation to simulate band profiles and n_e profiles for a range of ITO NCs (Figure 1.16).[20] Note the important difference between these graphs and those that were introduced when discussing doping and electronic structure (Figures 1.11 and 1.12). There is now an x-axis that tracks the radial coordinate inside the NC. In effect, this graph plots the electronic structure as a function of radius. These plots are referred to as band *profiles* as opposed to the earlier plots which were band *diagrams*.

The built-in potential, E_{BI}, determines whether the surface will accumulate charge, deplete charge, or remain neutral (i.e. flat-band condition, when E_{BI} is zero and therefore

W is zero). Under an oxidizing surface potential, the CBM bends upward near the surface as a result of potential gradient in the depletion layer. This band bending impacts the radial profile of n_e, which is constant at flat-band, but drops off significantly near the surface with an oxidizing potential. Even at a moderate E_{BI} of $0.67\ eV$, the NC in this example loses 17% of its electrons. The realization that the intra-NC charge carrier concentration profile is nonuniform may seem trivial at first, but this loss of charge carriers creates an insulating barrier between the plasmonic core and its surroundings, reducing the strength of their optical and electronic interaction. This impacts all plasmon-enhanced processes. My thesis work seeks to study and employ doped metal oxides as viable optoelectronic materials and this work centers around modeling and control over the nonuniform charge carrier distribution.

1.3 Dissertation Overview

"You can observe a lot by watching." That quote from Yogi Berra, Hall of Fame baseball player for the Yankees, relates to a theme present throughout my thesis: quantitative methods. If you look, or measure, carefully enough, you just might notice something that nobody else does. You might just learn something new. As you will see, my work begins simply with the goal of answering the question "how much light do these doped semiconductor nanocrystals absorb?" It turns out, the procedure required for answering this question is not so trivial, but once I figured it out, it was a launching pad for the rest of my work.

In more scientific terms, I learned how to measure the optical extinction with accuracy and reproducibility. This opened the door to applying this measurement technique to a range of samples for comparison. As fortune would have it, our lab was simultaneously adopting a colloidal synthetic technique that enabled improved size and doping control.

Naturally, these two procedures married into a happy project that explored the strength of infrared light absorption for spherical ITO NCs of sizes ranging from 5 to 20 nm in diameter and doping levels ranging from 0 to 7.5 at% Sn.

On top of reporting quantitative extinction coefficients for the first time for these materials, we uncovered unexpected trends with size and doping. To investigate the physical and chemical phenomena behind these trends we had to keep "observing by watching," this time watching even closer. We developed a model that accounted for phenomena unique to this material class that helped explain these trends and add to the overall understanding of material performance.

We then used this new understanding to engineer next-generation materials for optimal performance. In particular, we leveraged our improved colloidal synthetic techniques to segregate dopants within ITO NCs either to the core or to the shell. Initially, we did this because we expected the effect of segregating dopants to the shell to improve NC film conductivity – which it did. What we did not expect was the effect on the optical response. Segregating dopants promoted dual-mode plasmonic absorption. We were able to explain our results using the same quantitative spectroscopic techniques and a very similar optical model as before. We even showed that segregating dopants to the surface improved sensitivity to the surrounding dielectric.

In effect, I was able to use the information that I had gleaned from in depth study and characterization (Chapters 2[23] and 3[24]) to engineer a new design, namely the segregation of dopants within a NC, that promoted improved plasmonic properties (Chapter 4[25]). I hope what I've now learned can continue to be used to advance performance further. I comment on the future implications of this work in Chapter 5.

Chapter 2: Quantitative Analysis of Extinction Coefficients of Tin-Doped Indium Oxide Nanocrystals

The optical extinction coefficients of LSPR in doped semiconductor NCs have intensities determined by the density and damping mechanisms of free charge carriers. In the following chapter, we investigate the dependence of the extinction coefficient of tin-doped indium oxide (ITO) NCs on size and dopant concentration and find extinction coefficients as high as 56.6 μm^{-1} in the near-infrared for 20 nm diameter ITO NCs with 7.5 atomic% Sn. We find ITO NCs to be more efficient infrared light absorbers than metal nanoparticles or molecular dyes. We also find the intensive, volume-normalized extinction coefficient increases significantly with NC doping and NC diameter, but only up to a point of saturation in both cases. We qualitatively analyze trends in LSPR peak position and width to explain the effect of doping and size on extinction.‡

2.1 Introduction

Metal nanoparticles and semiconductor NCs with high free charge carrier concentration are widely studied for their distinct optical properties. Their strong, frequency-dependent polarizability arises from the oscillation of free charge carriers in response to incident electromagnetic radiation, known as localized surface plasmon resonance (LSPR). The efficient extinction of incident radiation by nanoscale plasmonic materials makes them ideal candidates for use in electrochromic windows[26–28], sensors[29–34], and photothermal theranostics.[35–40] In contrast to metals, doped semiconductor NCs derive free charge carriers from charge-compensated crystal defects resulting in carrier concentrations orders of magnitude lower, placing the LSPR frequency (ω_{LSPR}) in the

‡This chapter contains text and figures adapted from Ref. 23, which was written by Corey M. Staller and Stephen L. Gibbs as lead authors in collaboration with Camila A. Saez Cabezas and Delia J. Milliron. It has been adapted with permission from the authors. Copyright 2019 American Chemical Society

infrared. The carrier concentration can easily be modulated synthetically by tuning dopant concentration and post-synthetically by imposing an electrochemical bias or through photoelectrochemical charging.[16,26,41,42] Unable to significantly modulate carrier concentration, metal nanoparticle LSPR frequency is primarily tuned by manipulating particle size and geometry or by alloying.[43–46] The capability of tuning carrier concentration in semiconductor NCs allows infrared LSPR tunability independent of NC size while Au nanoparticles require sizes >200 nm or complex geometries to achieve infrared attenuation.[4,43,47–52] Using large nanoparticles can diminish extinction efficiency because increasing diameter introduces additional contributions to carrier damping such as phase retardation and multipolar excitation.[53] As well, constructive interference of incident electric fields in nanoscale gaps between neighboring plasmonic particles has proven to drastically enhance electric fields, forming "hot spots".[31] In comparison to their larger metal nanoparticle counterparts, doped semiconductor NCs can be packed at higher particle per volume to achieve higher hot spot densities in infrared applications.[49]

While several studies have investigated Au nanoparticle extinction coefficients,[38,39,43,53–55] those of most doped semiconductor NCs, particularly doped metal oxides, are not yet established. Of note, $Cu_{2-x}Se$ NC dispersions yielded an extinction coefficient of 23.5 μm^{-1} at 9399 cm^{-1} for NCs 65 nm in diameter[56] and recently the extinction coefficient for a film of tin-doped indium oxide (ITO) NCs of 10 atomic% (at%) Sn and 12 nm diameter was reported at 24.3 μm^{-1}.[57] The applications mentioned above require high extinction coefficient materials to be feasible and given that doped metal oxide NCs show promise as strong infrared absorbers, it is important to quantitatively investigate their optical extinction properties.

The far-field extinction spectrum of an ensemble of plasmonic NCs is influenced by a variety of factors. For instance, Zandi et al found films of ITO NCs display different

electrochemical modulation of optical properties depending on NC size and dopant concentration. They found smaller NCs and NCs with a lower dopant concentration to modulate significantly in peak energy *and* intensity under an electrochemically applied potential while larger, highly doped NCs primarily modulated in peak intensity.[18] These trends were explained on the basis of near-surface depletion layers (Section 1.2.5). As well, Lounis et al discovered that when comparing NCs of the same overall dopant concentration, those with dopants segregated to the surface will have fewer activated dopants and thus lower carrier concentration.[58] Depletion layers and the low activation of near-surface dopants in ITO NCs can be expected to negatively impact the strength of interaction with infrared light, especially for smaller NCs. To quantitatively assess the dependence of extinction on size and dopant concentration, and compare ITO NCs to other plasmonic nanoparticles, we measured their optical properties in dilute dispersions, thus avoiding complications due to NC-NC coupling that inevitably occur in the densely packed films, like those typically studied by spectroelectrochemistry.[18,59]

Herein, we investigate the influence of NC size and dopant concentration on the extinction peak energy, lineshape, and intensity for doped semiconductor NCs. We use ITO NCs as a model system because ITO is one of the most well-studied transparent conducting oxide (TCO) thin film materials[60] and there is a well-developed colloidal synthetic protocol that allows for size and dopant control.[61–63] Using quantitative analysis of optical spectra, we find the ITO NC extinction coefficient correlates strongly with NC size and dopant concentration. We find the extinction coefficient of 20 nm ITO NCs with dopant concentrations of 0 to 7.5 at% Sn to vary from 4.5 to 56.6 μm^{-1}. Additionally, the extinction coefficient of 5 at% Sn ITO NCs of diameter 6 to 20 nm varies from 13.6 to 51.9 μm^{-1}. These values indicate that within this size and doping range, NC size influences extinction coefficient nearly as strongly as dopant concentration. We also directly compare

these extinction coefficients to other absorbing material systems such as metal nanoparticles, chalcogenide NCs, and organic dyes and conclude that ITO NCs are more efficient for absorbing IR light.

2.2 Quantifying Extinction Coefficients in NC Dispersions

The Beer-Lambert Law defines the efficiency with which a material extinguishes light of a particular wavelength,

$$A = \frac{\epsilon f_V l}{\ln(10)} \qquad \text{Equation 2.1}$$

where A is the measured extinction in base 10 log scale, also referred to as optical density (OD), f_V is the volume fraction of the absorbing material, l is the pathlength through the sample, $ln(10)$ is included to convert extinction to natural log scale, and ϵ is the extinction coefficient (μm^{-1}). Therefore, by measuring the OD of a dilute dispersion of known concentration and pathlength, we can calculate the extinction coefficient of a NC ensemble. This metric for extinction is volume-normalized, which, as noted by Jain et. al, is a more meaningful comparison across particle sizes than other inherently size-dependent metrics such as extinction cross-section (Section 1.2.2) and molar absorption coefficient.[43] In Section 2.3 we will begin to see why it is so important to keep track of these units

Two series were prepared to investigate the role of NC size and dopant concentration on the optical properties of ITO NCs: a doping series from 0 to 7.5 at% Sn at 20 nm diameter and a size series from 6 to 20 nm diameter at 5 at% Sn. Details of NC synthesis and optical characterization are reported in Appendix A, Text A1 and A2. Details of size and shape characterization with small angle X-ray scattering (SAXS) and scanning transmission electron microscopy (STEM) are reported in Appendix A, Texts A3 & A4 and Figures A1-A3. Sn content as well as NC concentration in solution were quantified

with inductively coupled plasma-atomic emission spectroscopy, or ICP-AES (Appendix A, Text A5).

To investigate the extinction coefficient of ITO NCs, spectra were taken of dilute NC dispersions at various NC volume fractions. Figure 2.1a shows a representative dilution series at 5 different dilution factors ranging from 840x to 160x relative to a 34 mg ITO/mL stock solution. Accurate calculation of NC extinction coefficients requires the absence of NC-NC interactions such as NC-NC LSPR coupling or aggregation.[13] This condition can be tested by varying the volume fraction of NCs and inspecting extinction spectra for any response other than a linear dependence of extinction on NC concentration across all wavelengths. When normalized, spectra of all dilutions overlap nearly perfectly (Figure 2.1b). The extinction at ω_{LSPR} is shown to be linear with NC volume fraction (Figure 2.1c). These data verify that NC-NC interactions are absent in NC dispersions utilized in these studies. The extinction coefficient at ω_{LSPR} is calculated from the slope of extinction versus NC volume fraction in Figure 2.1c.

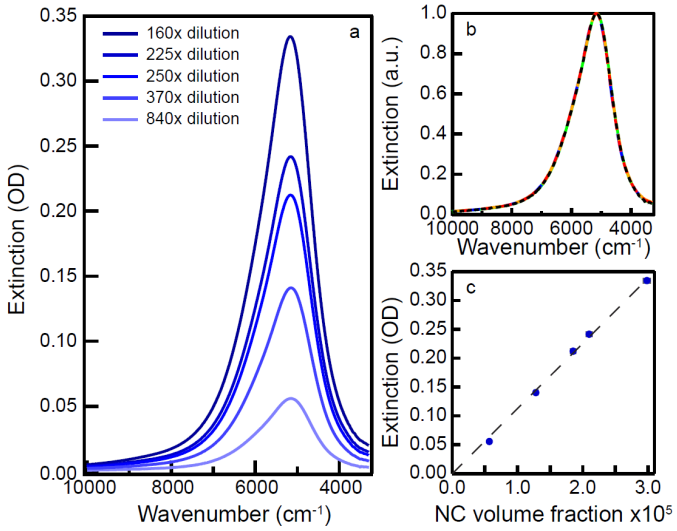

Figure 2.1: Determination of extinction coefficient. Optical spectra at various dilution factors (a), normalized spectra at each dilution (b), and linear fit to extinction v. NC volume fraction at ω_{LSPR} (c) for 6 at% Sn doped 20 nm ITO.

2.3 Doping Series

Figure 2.2a shows the quantitative extinction spectra of all samples across a series of dopant concentrations. Increasing dopant concentration manifests in a significant blue shift and increased intensity of the ITO LSPR peak. In Figure 2.2b we plot the extinction coefficient in two different units for comparison to literature values. The values on the left axis are normalized by total volume of NCs (μm^{-1}) in the dispersion and those on the right are normalized by the number of NCs ($M^{-1}cm^{-1}$) in the dispersion. These are known as the volume-normalized extinction coefficient and the molar extinction coefficient, respectively. Both data sets show the same trend: a strong, positive relationship with dopant concentration up to about 4.5 at% Sn, above which the extinction coefficient becomes nearly constant. The positive portion of the trend is rationalized using Mie theory (Section 1.2.2) for light interacting with particles much smaller than the incident wavelength, wherein the extinction coefficient increases with plasma frequency (and therefore electron

concentration). Identical trends in molar and volume-normalized extinction coefficient are expected when size-dependent effects may be neglected, as is the case here for NCs of nearly equal diameter.[13]

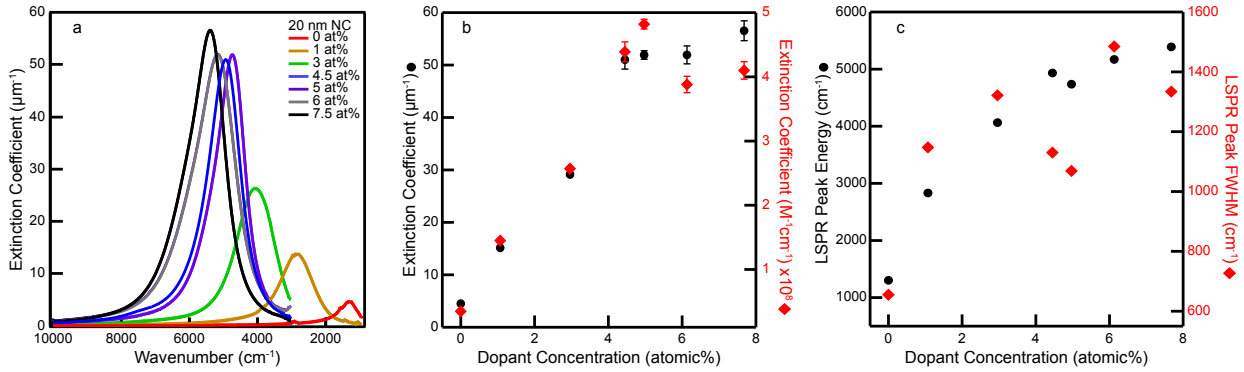

Figure 2.2: Dopant concentration series at constant NC diameter. Quantitative LSPR extinction spectra (a). Dopant concentration dependence of the extinction coefficient (b) and LSPR peak energy and FWHM (c).

The LSPR peak energy also rapidly increases with dopant concentration up to 4.5 at% Sn (Figure 2.2c). In this doping regime, LSPR peak energy is expected to blue shift proportionally with the square root of electron concentration. LSPR peak energy begins to saturate at higher dopant concentrations, consistent with the trend observed for extinction coefficient. The saturation of both of these optical parameters at high dopant concentration can be rationalized by dopant compensation. As seen on the Brouwer diagram of ITO (Figure A4), at high Sn concentration it becomes favorable for the positive charge associated with $Sn_{In}^{\bullet}$ defects to be compensated with oxygen interstitials $2Sn_{In}^{\bullet} - O_i''$ rather than with a free electron.[64,65] This interpretation is supported by an increase of the optical band gap with dopant concentration (Burstein-Moss effect) that also begins to saturate above 4.5 at% Sn (Figure A5). The LSPR peak full-width at half-maximum (FWHM) trends upward with increased dopant concentration (Figure 2.2c), consistent with

increased damping at higher dopant concentrations. In studies of ITO thin films, electron mobility, which has an inverse relationship to damping, decreases with increasing carrier concentration, in qualitative agreement with the trend in FWHM observed here.

2.4 Size Series

Increasing NC diameter results in a moderate blue shift and significantly increased intensity of the ITO LSPR peak on a per volume basis (Figure 2.3a). The volume-normalized and molar extinction coefficients are plotted against NC volume and the trends differ significantly (Figure 2.3b). For the molar extinction coefficient we observe an approximately linear increase with NC volume, as expected for particles much smaller than the wavelength of incident light in the quasi-static regime.[53] If extinction were simply a function of the total volume of absorbing material, then the volume-normalized extinction coefficient would be constant as NC size increases. However, our results show the volume-normalized extinction coefficient increases with increasing NC size before saturating for NCs above 12 nm diameter (Figure 2.3b), implying the presence of size-dependent effects on optical extinction in ITO NCs.

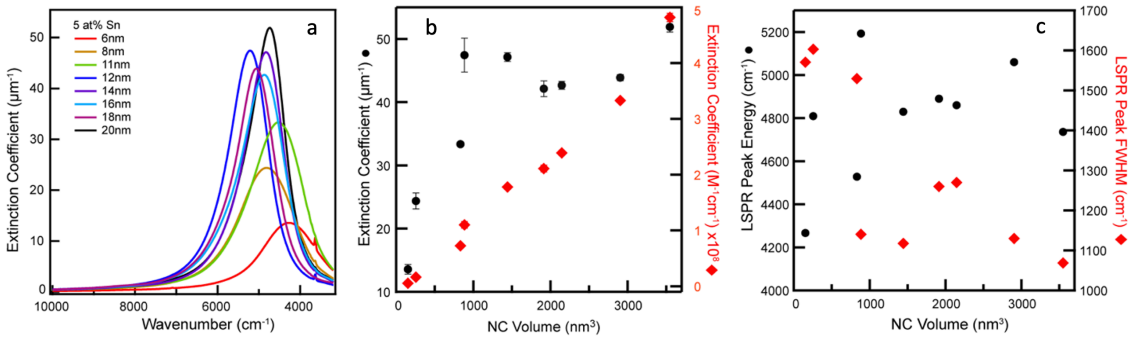

Figure 2.3: Size series at constant dopant concentration. Quantitative LSPR extinction spectra (a). Size dependence of the extinction coefficient (b) and LSPR peak energy and FWHM (c).

As we did for the doping series, we can qualitatively explain this behavior by analyzing the peak position and width, now with increasing size. The LSPR peak energy for ITO NCs generally blue shifts with increasing NC diameter (Figures 2.3a and 2.3c). The significant scatter in this trend is likely due to sample-to-sample variations in doping concentration, with the 6, 8, and 12 nm samples having higher Sn concentration, near 5.5 at%, while the 15, 16, and 18 nm samples have lower Sn concentration, near 4.7 at% (Appendix A, Table A1). Even so, the peak energy tends to increase with size. The blue shift is primarily attributed to an increase in free carrier concentration at increased NC size, which is supported by an increase of the optical band gap with NC diameter at constant 5 at% Sn (Figure A5). The origin of a size-dependent electron concentration may be attributed to the lower activation of dopants near the NC surface,[58,63,66] with a greater proportion of dopants falling in the near-surface region in smaller NCs. Surface depletion will also contribute to the size-dependent optical response because the carrier-depleted volume will consume a larger fraction of the overall NC volume for smaller sizes.[18] Both of these effects become more prominent as the surface area to volume ratio increases.

The LSPR peak tends to narrow as NC radius increases (Figure 3.3c), which has also been observed for Cr-Sn co-doped In_2O_3.[66] We can draw an interesting comparison between the size-dependent peak characteristics of ITO NCs and Au nanoparticles in this size regime. For both materials, the FWHM drops with increasing diameter due to a reduction in surface scattering. However, increasing diameter can broaden and red-shift the peak when phase retardation and multipolar excitations become prominent, which occurs as nanoparticle diameter grows beyond what is considered the quasi-static regime ($d \sim \lambda_{LSPR}/20$).[53,67] While the visible wavelength LSPR puts this transition around 25 nm in diameter for Au nanoparticles, the IR LSPR in ITO pushes it to 100 nm or larger. The NCs studied here do not approach that size and thus do not exhibit peak broadening or red-

shifting associated with increasing size. In fact, our results show increasing NC diameter improves the extinction as a result of higher carrier concentration as well as decreased damping. We would expect this trend to saturate, then, when (1) the fraction of deactivated dopants near the surface is small compared to activated dopants and (2) when surface scattering is not a strong contributor to overall damping. Based on our results, these effects are minimally important above about 12 nm in diameter for 5 at% ITO NCs.

2.5 Magnitude of ITO NC Extinction

Apart from the trends in doping and size, it is important to contextualize the magnitude of the extinction coefficients in ITO NCs. The LSPR peak in these ensembles ranges from 4.5 μm^{-1} ($3.5 \times 10^7\ M^{-1}cm^{-1}$) at 1300 cm^{-1} for 20 nm undoped indium oxide NCs to 56.6 μm^{-1} ($4.1 \times 10^8\ M^{-1}cm^{-1}$) at 5289 cm^{-1} for 20 nm 7.5 at% Sn ITO NCs. These values are high when compared to other infrared absorbing materials. Common infrared absorbing or scattering materials such as Au nanostructures ($\epsilon_{sca} = 35.5\ \mu m^{-1}$ at 8620 cm^{-1}),[43] $Cu_{2-x}Se$ NCs ($\epsilon_{abs} = 23.5\ \mu m^{-1}$ at 9399 cm^{-1}),[56] the first exciton peak of 5.5 nm PbSe QDs ($\epsilon_{abs} = 12.7\ \mu m^{-1}$ at 6250 cm^{-1}),[68] and commercially available infrared dyes ($9.8 \times 10^4\ M^{-1}cm^{-1}$ at 12,690 cm^{-1})[69] all attenuate IR light less efficiently than ITO NCs of minimum 4.5% Sn doping and 12 nm diameter. Alternative extinction coefficient units for these samples are shown in Table A1 for comparison. To our knowledge, the ITO NCs reported here have a higher volume-normalized extinction coefficient than any prior report of absorbing materials in this frequency regime. Remarkably, ITO NCs have extinction coefficient comparable to the absorption coefficient of spherical Au nanoparticles of diameter 4 – 20 nm (34.0 – 73.7 μm^{-1}) despite having a peak much lower in energy.[53,55] Furthermore, because of their relatively small size, nearly all of the extinction is light absorption by the ITO NCs in the dispersion. In contrast, Au NPs or nanoshells that are

made sufficiently large to resonate with infrared light often scatter as much or more light than they absorb.[43] Hence, for applications requiring absorption of infrared light, TCO NCs like ITO provide a compelling alternative to conventional plasmonic metal nanoparticles.

2.6 Conclusion

In conclusion, we have quantitatively analyzed the extinction of ITO NC dispersions and have reported the highest extinction coefficients for IR absorbing materials to date. The extinction coefficient of ITO NCs is shown to increase with increasing dopant concentration and increasing NC diameter. These effects are explained by variations in electron concentration and damping. A greater doping density will raise electron concentration and a larger NC diameter will reduce overall dopant deactivation, thereby raising electron concentration. A larger NC diameter will also reduce electron damping. These results indicate synthesizing large and highly doped semiconductor NCs is an optimal strategy for achieving narrow LSPR and high extinction coefficient in the IR, but for ITO each parameter reaches a point of diminishing returns around 4.5% Sn and 12 nm diameter, respectively. Balancing NC dopant concentration and diameter will be crucial to optimizing performance for these materials in IR applications like electrochromic devices, sensors, and photothermal therapy.

2.7 Future Work: Failure of Standard Fitting Procedures

The qualitative explanations for trends in FWHM, ω_{LSPR}, and ϵ with size and doping could be strengthened by fitting the LSPR spectra using a model such as the simple Drude approximation (SDA). The basic assumption of this model are outlined in Section 1.2.1. Previously reported SDA model fitting procedures require the input of pathlength and material constants that are used to fit for volume fraction, damping constant, and

plasma frequency. For smaller NC sizes, these fits yielded volume fractions that significantly differ from the measured values, so the volume fraction is instead acting as a correction (or "fudge") factor that scales the fitted extinction intensity. Realizing that this fudge factor could compromise the accuracy of the material properties extracted from the fits, we tried fitting the LSPR spectra with the SDA using a fixed volume fraction, set at the experimentally measured value. This constrained SDA was unable to produce reliable fits for a handful of spectra, especially for those of NCs with diameter 12 nm and below. As mentioned previously, this limit is around the critical diameter at which we see that size-dependent effects become prominent, indicating the SDA may be inadequate to accurately describe the optical spectra and assess associated material properties for these samples. Since the SDA is the standard for extracting electronic properties from plasmonic materials,[70–73] this limitation is an important constraint that hampers the utility of fitting procedures to gain accurate physical insight into material properties. We expected that incorporating the presence of surface depletion layers and ensemble heterogeneity in the fitting procedure would enable more quantitative analysis and this is the subject of the next chapter.

Chapter 3: Intrinsic Optical and Electronic Properties from Quantitative Analysis of Plasmonic Semiconductor Nanocrystal Optical Extinction

The optical extinction spectra arising from localized surface plasmon resonance in doped semiconductor NCs have intensities and lineshapes determined by free charge carrier concentrations and the various mechanisms for damping the oscillation of those free carriers. However, these intrinsic properties are convoluted by heterogeneous broadening when measuring spectra of ensembles. In this chapter, we reveal that the traditional Drude approximation is not equipped to fit spectra from a heterogeneous ensemble of doped semiconductor NCs and produces fit results that violate Mie scattering theory. The heterogeneous ensemble Drude approximation (HEDA) model rectifies this issue by accounting for ensemble heterogeneity and near-surface depletion. The HEDA model is applied to ITO NCs for a range of sizes and doping levels but we expect it can be employed for any isotropic plasmonic particles in the quasistatic regime. It captures individual NC optical properties and their contributions to the ensemble spectra thereby enabling the analysis of intrinsic NC properties from an ensemble measurement. Quality factors for the average NC in each ensemble are quantified and found to be notably higher than those of the ensemble. Carrier mobility and conductivity derived from HEDA fits matches that measured in the bulk thin film literature.[§]

3.1 Introduction

As mentioned above, doped semiconductor NCs are ideal candidate materials for accessing infrared frequencies, an important wavelength regime for emerging technologies

[§]This chapter contains text and figures adapted from Ref. 24, which was written by Stephen L. Gibbs and Corey M. Staller as lead authors in collaboration with Ankit Agrawal, Robert W. Johns, Camila A. Saez Cabezas, and Delia J. Milliron. It has been adapted with permission from the authors. Copyright 2020 American Chemical Society

in waveguiding for telecommunication,[74–77] molecular sensing,[31,49,78,79] and photothermal theranostics.[38,40,80] Plasmonic enhancement of these processes relies on strong light-matter interaction within a narrow bandwidth, which can be quantified as the ratio of ω_{LSPR} to the full width at half maximum (FWHM), also known as the quality factor or Q-factor.

Factors that contribute to the FWHM of LSPR in a NC ensemble include both physical properties of the individual NCs, what we refer to as *intrinsic damping*, and the particle-to-particle variations in these properties, what we refer to as *heterogeneous broadening*. Intrinsic damping is inversely proportional to electron mobility within a NC, which is dependent on the carrier concentration and the mean free path of the charge carriers. The mean free path is proposed to be dominated by surface damping in nanostructures with one or more dimensions smaller than the bulk mean free path.[13] Size-dependent damping consistent with free electron surface damping was observed in Ag[81] and Au nanoparticles.[53] Unlike their noble metal counterparts, semiconductor NCs such as tin-doped indium oxide (ITO) form depletion regions near the surface which significantly influence LSPR.[17] These near-surface depletion layers have widths on the order of a nanometer, have significantly reduced free carrier concentration, and effectively shrink the volume accessible to conduction band electrons.[19,82] We expect the extent of depletion to be an important consideration for damping in doped semiconductors because their presence is expected to reduce the mean free path of the free charge carriers.

Typical optical models used to analyze LSPR spectra convolute intrinsic damping and heterogeneous broadening into a single damping term, leading to potential misinterpretation of material electronic properties. Despite the rather narrow size distributions achieved by recent synthetic developments in nanoparticles, size polydispersity is still often nearly 10%.[61,62] Prior work has shown that the far-field extinction spectra of doped semiconductor NCs are very sensitive to NC diameter.[23,83]

When surface damping is prominent, a size distribution within an ensemble of NCs causes a distribution of intra-NC electron mobility due to variations in surface damping, contributing to heterogeneous broadening. Beyond size distribution effects, dopant incorporation also varies from NC-to-NC within an ensemble, leading to significant carrier concentration polydispersity and adding to heterogeneous broadening.[84] Indeed, when absorption spectra of single aluminum-doped zinc oxide and ITO NCs were directly measured, Johns et al. found striking variability in linewidth and in absorption peak energy within ensemble populations.[85]

The typical fit procedure for extracting material properties from LSPR extinction spectra, the simple Drude approximation (SDA), does not account for the effects of near-surface depletion layers or ensemble heterogeneity. These limitations obscure interpretation of ensemble measurements and can potentially mislead efforts to develop higher Q-factor materials. Herein, we present a model that builds on the SDA for the more incisive fitting of optical spectra of NC ensembles. The heterogeneous ensemble Drude approximation (HEDA) model uses only well-known material constants and routinely measured NC physical properties to fit for NC properties that cannot be easily measured directly, those being: carrier concentration, carrier concentration polydispersity, near-surface depletion width, and bulk mean free path. By analyzing the far-field response as a sum of contributions from individual NCs, the ensemble fit enables analysis of physical properties for individual NCs within an ensemble without the laborious effort of single NC spectroscopy. We use ITO NCs of varying dopant concentrations and sizes as a model system where fitting results can be compared to expectations from a well-established literature to establish both the validity and potential of the new analysis procedure. We find the volume-normalized extinction coefficient, as well as the Q-factor, of an average NC is significantly higher than its corresponding ensemble, mainly due to heterogeneous

broadening as a result of carrier concentration heterogeneity. Neglecting ensemble heterogeneity and near-surface depletion, the conventional SDA model failed to fit our data with physically realistic parameter values consistent with Mie scattering theory. The HEDA model rectified this inconsistency. The SDA underestimates the electron mobility of individual NCs due to the convolution of intrinsic damping and heterogeneous broadening. HEDA analysis yields an electron mobility within colloidal ITO NCs ranging from 15 to 35 $cm^2V^{-1}s^{-1}$ and extracts bulk mobility values matching those reported by Hall effect measurements in ITO thin films.[64]

3.2 METHODS

See Appendix A, Texts A1-A5 for notes on the synthesis and spectroscopy measurements as well as Figures A1-A3 for STEM images and SAXS plots.

3.2.1 Fitting Procedure.

Optical spectra were fit using both the SDA and HEDA models. HEDA model fits were solved for using the MATLAB® that can be found in the supporting information of Ref. 24. All four dilutions were fit independently for each sample and used to create error bars for fit variables. For each dilution, the volume fraction and NC size distribution were fixed to the measured values. The model then uses a least squares function to fit for four variables (described below) within fit constraints. Final fit values were found to be independent of initial guess values.

3.3 Results and Discussion

3.3.1 Fitting NC Ensemble Optical Spectra

To test the robustness of this model, we compared fit quality of the HEDA and SDA models across fifteen independently synthesized samples of ITO NCs with wide-ranging doping level and size: 0 to 7.5 at% Sn and 6 to 20 nm in diameter, respectively. The SDA model requires the input of pathlength and material constants and then fits for NC volume fraction in solution, f_V, damping constant, Γ, and plasma frequency, ω_p. These fitting procedures often yield a volume fraction that doesn't match the measured value, but instead erroneously acts as a correction factor to scale the fitted extinction intensity. To eliminate this artificial scaling factor, LSPR spectra were also fit using the SDA with f_V fixed to the independently measured value. When f_V is fixed, the SDA is unable to simultaneously fit peak intensity and lineshape (Figure 3.1). We hypothesized that these discrepancies arise because the SDA uses a single damping value and a single plasma frequency value to fit an ensemble spectrum that has a distribution of those values.[72] Hereafter, only the SDA with floating volume fraction will be discussed as it is the common method for fitting optical extinction spectra. Across a wide range of doping levels and sizes, the HEDA model, unlike the SDA, reliably fits ensemble spectra with the volume fraction *fixed* to the measured value (Appendix B, Figure B1).

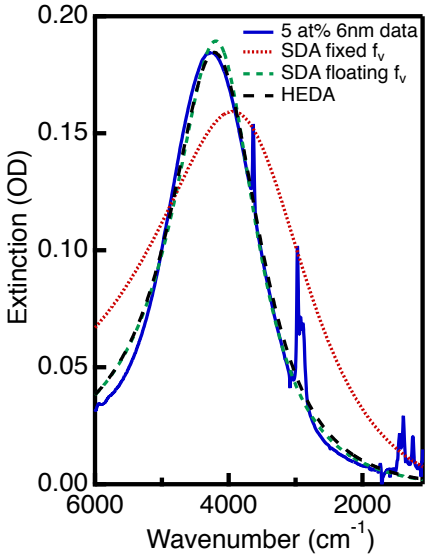

Figure 3.1: Three models for fitting extinction spectra. Simple Drude approximation (SDA) with a floating NC volume fraction f_V, SDA with f_V fixed to the measured value, and heterogeneous ensemble Drude approximation (HEDA) fits to extinction data for 5 at% Sn 6 nm ITO NCs.

Unlike the SDA, the HEDA model accounts for ensemble heterogeneity by considering that there are finite distributions for both the NC size and carrier concentration. Beyond ensemble heterogeneity, the HEDA model improves upon the SDA by explicitly considering the impact of near-surface depletion layers and surface scattering on the optical response. To do this, in addition to the basic inputs required for the SDA model, the HEDA model takes as fixed inputs the independently measured mean NC radius, NC radius standard deviation, and f_V. These parameters are routinely measured, though this information is not typically used in SDA fitting procedures. The model then fits for four variables: the average carrier concentration, n_e, the standard deviation in carrier concentration, σ_{n_e}, the electron accessible volume fraction considering surface depletion, f_e, and the mean free path of an electron in the bulk material, l_{bulk}. The effects of NC radius and each HEDA model parameter on the extinction spectra can be calculated and plotted *a priori*. (Figure 3.2)

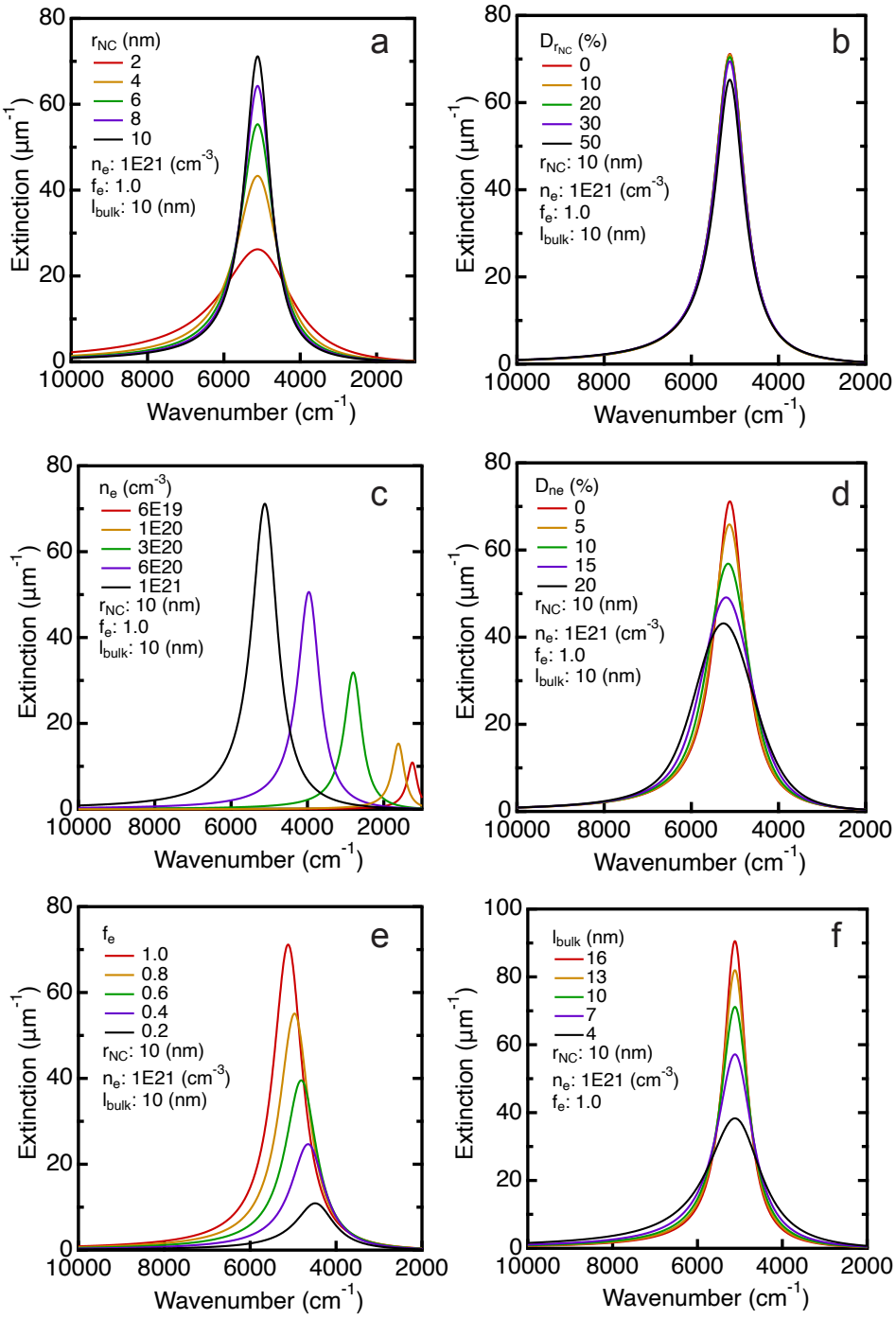

Figure 3.2: Calculated LSPR spectra. Volume-normalized extinction spectra for ITO NC ensembles of varying NC radius (a), NC radius polydispersity (b), electron concentration (c), electron concentration polydispersity, electron accessible volume fraction (e), and bulk mean free path (f).

Below we outline the how the HEDA model incorporates each of these physical phenomena illustrated in Figure 3.2.

3.3.1.1 Near-surface depletion regions

Metal oxide surfaces are commonly passivated by adsorbed water species, including surface hydroxyls, which create a density of electronic states near the NC surface. When these surface states are below the NC bulk Fermi level they cause a decreased carrier concentration near the NC surface, known as a depletion region (Figure 3.3a).[17,19,82] Due to the buildup of electrostatic potential, depletion regions near the NC surface decrease the fraction of the NC volume accessible to mobile charge carriers as evidenced by decreased conductivity in NC films when depletion regions are prevalent.[20] The HEDA model accounts for near-surface depletion by fitting for an electron accessible volume fraction, f_e. The radius of the spherical volume accessible to mobile charges is then $f_e^{1/3} r_{NC}$, where r_{NC} is the NC radius. For ITO, the mobile charges are electrons and this decreased radius is the electron accessible radius. The near-surface depletion creates a pseudo-core-shell geometry where the NC can be described as an electron-rich core with an electron-deficient shell. This geometry requires a modification to the dielectric function of these materials to successfully model their optical response.[82] The Maxwell-Garnett effective medium approximation (EMA) is used to define the dielectric function of a core-shell NC, ε_{cs}, as

$$\varepsilon_{cs}(\omega) = \varepsilon_{shell}\left(\frac{(\varepsilon_{NC} + 2\varepsilon_{shell}) + 2f_e(\varepsilon_{NC} - \varepsilon_{shell})}{(\varepsilon_{NC} + 2\varepsilon_{shell}) - f_e(\varepsilon_{NC} - \varepsilon_{shell})}\right) \qquad \text{Equation 3.1}$$

where $\varepsilon_{shell}(\omega)$ is the dielectric function of the depleted shell and $\varepsilon_{NC}(\omega)$ is the dielectric function of the core. The EMA is applicable for variable thickness of the depleted shell, converging to $\varepsilon_{NC}(\omega)$ when $f_e = 1$.

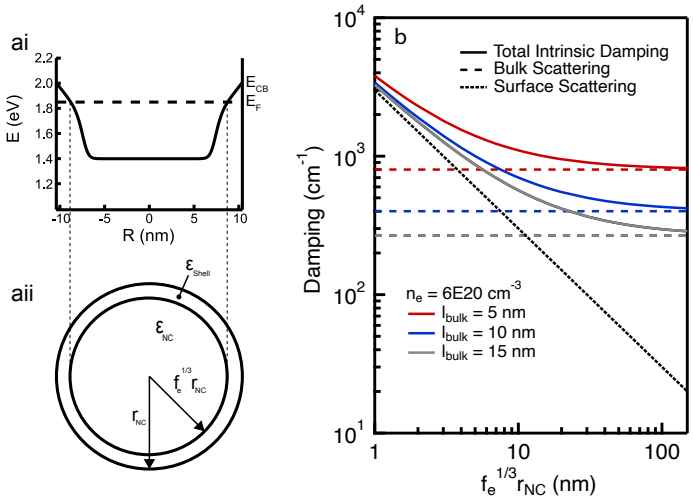

Figure 3.3: Theoretical concepts for surface depletion and surface scattering. Conduction band profile (ai) and schematic (aii) for a NC with surface depletion. Calculated total intrinsic damping and its contributions from bulk and surface scattering as a function of electron accessible radius $f_e^{1/3} r_{NC}$ for l_{bulk} = 5, 10, & 15 nm at $n_e = 6 \times 10^{20}$ cm^{-3} (b).

3.3.1.2 Intrinsic damping

The LSPR linewidth of a single spherical NC depends on the damping constant, which is the rate at which conduction electrons scatter. The damping constant, Γ, is often used as a fitting parameter; however, free carrier damping can be calculated directly from the Drude conductivity as[53,86]

$$\Gamma = \frac{(3\pi^2)^{\frac{1}{3}}\hbar}{m_e^*} n_e^{\frac{1}{3}} \left(\frac{1}{l_{MFP}}\right) \qquad \text{Equation 3.2}$$

where $\hbar$ is Planck's constant, m_e^* is the effective electron mass, n_e is the electron concentration, and l_{MFP} is the electron mean free path. For NCs of radius comparable to or less than the material's bulk mean free path, surface scattering influences the overall mean free path of NC conduction electrons (Figure 3.3b).[53,81] Assuming surface scattering to be specular and applying Matthiessen's rule, the electron mean free path is described by[13,87]

$$\frac{1}{l_{MFP}} = \left(\frac{1}{\frac{4}{3} r_{NC} f_e^{\frac{1}{3}}} + \frac{1}{l_{bulk}} \right) \qquad \text{Equation 3.3}$$

where l_{bulk} is the mean free path for the bulk material. There are many reports that measure the bulk mean free path of electrons in ITO to be anywhere from 5 to 17 nm and its dependence on electron concentration is unclear.[64,70,88,89] Due to this uncertainty, l_{bulk} is used as a fit parameter to capture its relationship to other physical parameters. Based on our search, an upper bound of 17 nm was placed on the mean free path to ensure meaningful output values and prevent small, surface scattering-dominated NCs from reporting infinite values for bulk mean free path. The intrinsic damping constant can then be defined by combining Equations 3.2 and 3.3 as

$$\Gamma = \frac{(3\pi^2)^{\frac{1}{3}} \hbar}{m_e^*} n_e^{\frac{1}{3}} \left(\frac{1}{\frac{4}{3} r_{NC} f_e^{\frac{1}{3}}} + \frac{1}{l_{bulk}} \right) \qquad \text{Equation 3.4}$$

Intrinsic damping is particularly size-dependent when surface damping dominates bulk damping, i.e., when the electron accessible radius is smaller than l_{bulk} (Figure 3.3b). For larger particles, it converges to the bulk damping value above a radius about 10 times l_{bulk}, however this is much larger than the NC radii used in this study. With l_{bulk} expected to lie between 5 and 17 nm, and the radii of the NCs in this study ranging from 3 to 10 nm, we expected surface damping to be a significant, if not dominant, factor in overall intrinsic damping.

3.3.1.3 Ensemble heterogeneity

Size heterogeneity and electron concentration heterogeneity are modeled as Gaussian distributions. To do this, we construct a two-parameter probability density function (PDF) that ranges from the mean value plus or minus three standard deviations in

NC radius and electron concentration. The PDF is then discretized with a 41x41 data point mesh containing 1681 permutations of NC radius and electron concentration. Fit results varied by less than 0.5% when the data point mesh size was changed from 31x31 to 41x41, indicating additional PDF resolution does not significantly change results. The total extinction of an ensemble is a probability-weighted sum of these 1681 NCs. To obtain the extinction for a two-dimensional matrix of NCs we first calculate the plasma frequency and damping of each NC, with electron accessible radius $r_{NC_i} f_e^{\frac{1}{3}}$ and electron concentration n_{e_j}

$$\omega_{p_j} = \sqrt{\frac{q^2 n_{e_j}}{\varepsilon_0 m_e^*}} \qquad \text{Equation 3.5}$$

$$\Gamma_{ij} = \frac{(3\pi^2)^{\frac{1}{3}}\hbar}{m_e^*} n_{e_j}^{\frac{1}{3}} \left(\frac{1}{\frac{4}{3} r_{NC_i} f_e^{\frac{1}{3}}} + \frac{1}{l_{bulk}} \right) \qquad \text{Equation 3.6}$$

where q is the electron charge and ε_0 is the permittivity of vacuum. The complex dielectric function $\varepsilon_{NC_{ij}}(\omega)$ is expressed using the Drude-Lorentz model

$$\varepsilon_{NC_{ij}}(\omega) = \varepsilon_\infty - \frac{\omega_{p_j}^2}{\omega^2 + i\omega\Gamma_{ij}} \qquad \text{Equation 3.7}$$

where ε_∞ is the high-frequency dielectric constant for a given material. As described above, the presence of a depletion layer necessitates the use of a core-shell geometry for the complex dielectric function.

$$\varepsilon_{cs_{ij}}(\omega) = \varepsilon_{shell} \left(\frac{\left(\varepsilon_{NC_{ij}} + 2\varepsilon_{shell}\right) + 2f_e\left(\varepsilon_{NC_{ij}} - \varepsilon_{shell}\right)}{\left(\varepsilon_{NC_{ij}} + 2\varepsilon_{shell}\right) - f_e\left(\varepsilon_{NC_{ij}} - \varepsilon_{shell}\right)} \right) \qquad \text{Equation 3.8}$$

In systems of non-interacting spheres, the absorption cross-section of a single particle, $\sigma_{abs_{ij}}$, is defined by Mie theory as

$$\sigma_{abs_{ij}}(\omega) = 8\pi^2 r_{NC_i}^3 \omega \sqrt{\varepsilon_m} Imag\left\{\frac{\varepsilon_{cs_{ij}}(\omega) - \varepsilon_m}{\varepsilon_{cs_{ij}}(\omega) + 2\varepsilon_m}\right\} \qquad \text{Equation 3.9}$$

where ε_m is the dielectric constant of the surrounding medium. For NCs smaller than 5% of the wavelength of incident light, scattering of incident light is negligible and therefore extinction is equal to absorption (Section 1.2.3).[13] The absorption cross-section for each of the 1681 points is probability-weighted and summed to give the effective absorption cross-section for the ensemble, σ_{abs}^{eff}, as

$$\sigma_{abs}^{eff} = \sum_i^m \sum_j^n \left(\sigma_{abs_{ij}}(\omega) p_{n_{e_j}} p_{r_{NC_i}} \Delta n_e \Delta r_{NC}\right) \qquad \text{Equation 3.10}$$

where $p_{n_{e_j}}$ and $p_{r_{NC_i}}$ are the probabilities of n_{e_j} and r_{NC_i}, respectively, Δn_e and Δr_{NC_i} are the step sizes for n_e and r_{NC}, respectively, and m and n are the mesh dimensions (41 here). The effective absorption cross-section of the ensemble is then plugged into the Beer-Lambert law,

$$A = \frac{f_V l}{\ln(10)\, V} \sigma_{abs}^{eff} \qquad \text{Equation 3.11}$$

where V is the average volume of a NC, defined as

$$V = \sum_i^m \sum_j^n \left(\frac{4}{3}\pi r_{NC_i}^3 p_{n_{e_j}} p_{r_{NC_i}} \Delta n_e \Delta r_{NC}\right) \qquad \text{Equation 3.12}$$

The HEDA model fitting procedure was demonstrated to be robust by using a variety of initial guesses for each fitted parameter. Changing the initial guesses within fit parameter constraints did not change the solution. Aside from fitting errors, one potential source of error for the HEDA model is non-physical fit parameter correlations. Our model contains multiple parameters that influence the FWHM (specifically σ_{n_e}, f_e, and l_{bulk}) and so we plotted those parameters against each other and found no correlations.

Independence of all broadening factors among a diverse set of samples supports that the HEDA model yields meaningful values and is a robust model. We note that fitting for a single f_e and l_{bulk} rather than distributions of these parameters was an appropriate simplification because the heterogeneity in these parameters is expected to be much smaller than in NC radius or carrier concentration.

3.3.2 HEDA Fit Results

The 15 investigated samples can be split into two series: a doping series from 0 to 7.5 at% Sn at 20 nm diameter and a size series from 6 to 20 nm diameter at 5 at% Sn. To account for any deviation occurring as a result of colloid preparation or spectra collection, four spectra were collected for each sample from independently prepared dilute dispersions of NCs in tetrachloroethylene (TCE). The plots and error bars illustrate the average and standard deviation of the parameters extracted from the four measurements. Sample details and fit results are summarized for the NC size (Table B1) and dopant concentration (Table B2) series. Statistically significant correlations were determined by t-test against the null hypothesis of zero correlation between variables, i.e., the slope is zero. The null hypothesis was rejected for those variables with significance values of $\alpha < 0.05$, confidently concluding the existence of a relationship between them.

3.3.2.1 Quantifying ensemble heterogeneity

The polydispersity D (defined here as the standard deviation divided by the average value in a Gaussian distribution) in radius was quantified from small angle X-ray scattering (SAXS). There was a decreasing trend in D_R with radius (Figure 3.4a) and increasing trend in D_R with dopant concentration (Figure 3.4b). The trends in size elucidate that under our synthetic conditions we can achieve the lowest polydispersity in larger, lower-doped NCs.

While D_R was measured by SAXS, the polydispersity in carrier concentration, D_{n_e}, was determined from the HEDA fitting. In the ideal case, dopant incorporation varies minimally within an ensemble and follows Poissonian statistics.[72,84] At high dopant incorporation, the standard deviation for number of dopant atoms incorporated in single NCs, N_d, is approximated by Poissonian statistics as $\sigma_{N_d} \approx \sqrt{\mu_{N_d}}$, where μ_{N_d} is the average value of N_d in the NC ensemble.[85] Converting this expectation into carrier concentration, Poissonian statistics predict a drop in carrier concentration polydispersity with increasing radius to a power law dependence $D_{n_e} \propto r^{-1.5}$ and with increasing donor density $D_{n_e} \propto {N_d}^{-0.5}$, plotted as the solid red lines in Figures 3a and 3b. Our results contradicted this expectation, showing no trend in D_{n_e} with either r_{NC} or N_d. Moreover, D_{n_e} was significantly larger across all sizes and dopant concentrations than the Poissonian expectation, consistent with the elevated dopant heterogeneity previously reported based on single particle measurements.[85] Reducing dopant heterogeneity to the Poissonian limit presents an opportunity for synthetic development to advance the utility of doped semiconductor NCs and improve ensemble optical performance. For example, peak extinction of a NC ensemble with average values r_{NC}= 10 nm and n_e= 6x10^{20} cm^{-3} would be increased by 17% when the D_{n_e} drops from 10% to the Poisson limit (2%).

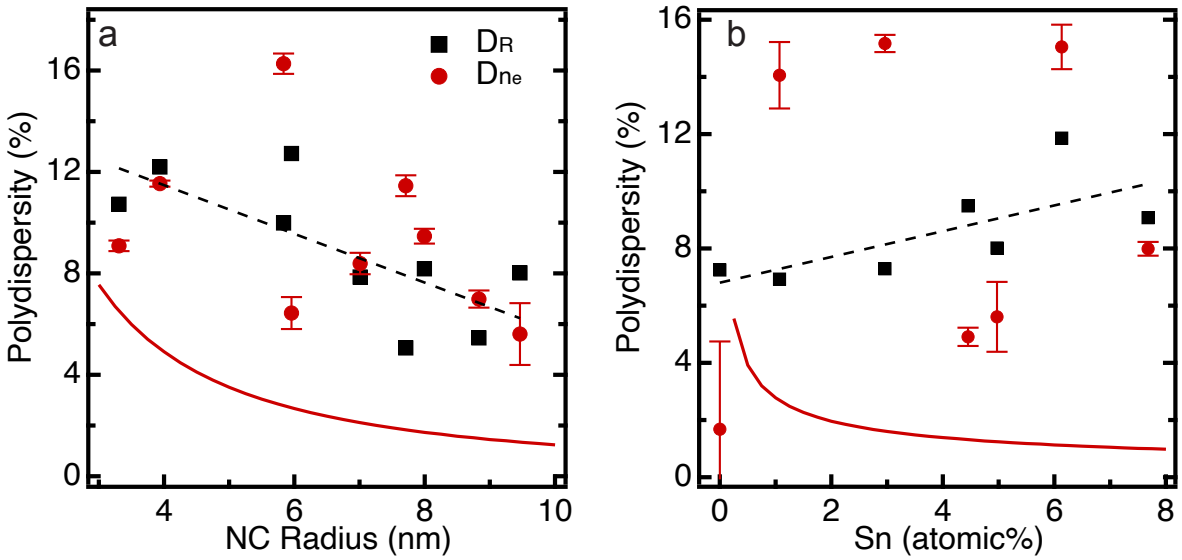

Figure 3.4: Quantification of ensemble heterogeneity. Polydispersity in radius D_R (black squares) measured by small angle X-ray scattering (SAXS) and polydispersity in carrier concentration D_{n_e} (red circles) extracted by fitting with the HEDA model as a function of NC radius (a) and at% Sn (b). Dashed lines show linear fits to each sample set with statistically significant correlation. Red, solid lines illustrate the expected polydispersity for dopant incorporation dictated by Poissonian statistics. Error bars indicate standard deviation in the results from HEDA fitting for four independently prepared dispersions of each sample.

3.3.2.2 Intrinsic properties for the average NC in an ensemble

Fitting ensemble spectra with the HEDA model enables extraction of intrinsic material properties distinguished from the convoluting effects of heterogeneous peak broadening. Application of the HEDA model to a range of ITO NCs precisely tracks the trends in fit parameters with NC size and doping. Electron concentration, n_e, increases with dopant concentration (Figure 3.5aii), but does so more slowly above 4.5 at% Sn due to decreasing dopant activation (Figure B2) which is defined as the ratio between n_e and the measured dopant concentration. Dopant activation is expected to decrease at higher dopant concentrations and increase with larger NC radius.[23,65,66] While dopant activation did increase with NC radius (Figure B2), there was no correlation between n_e and NC

radius (Figure 3.5ai). We suspect this is due to the moderate dopant concentration variations between samples in the size series (Table B1) that could obscure a trend in n_e. Electron accessible volume fraction, f_e, increases with NC radius and dopant concentration (Figures 3.5ai and 3.5aii), in agreement with prior work.[17,59,82,90] The near-surface depletion region narrows with increased NC size due to decreased surface area to volume ratio and with a higher concentration of ionized donors that screen the surface potential offset.

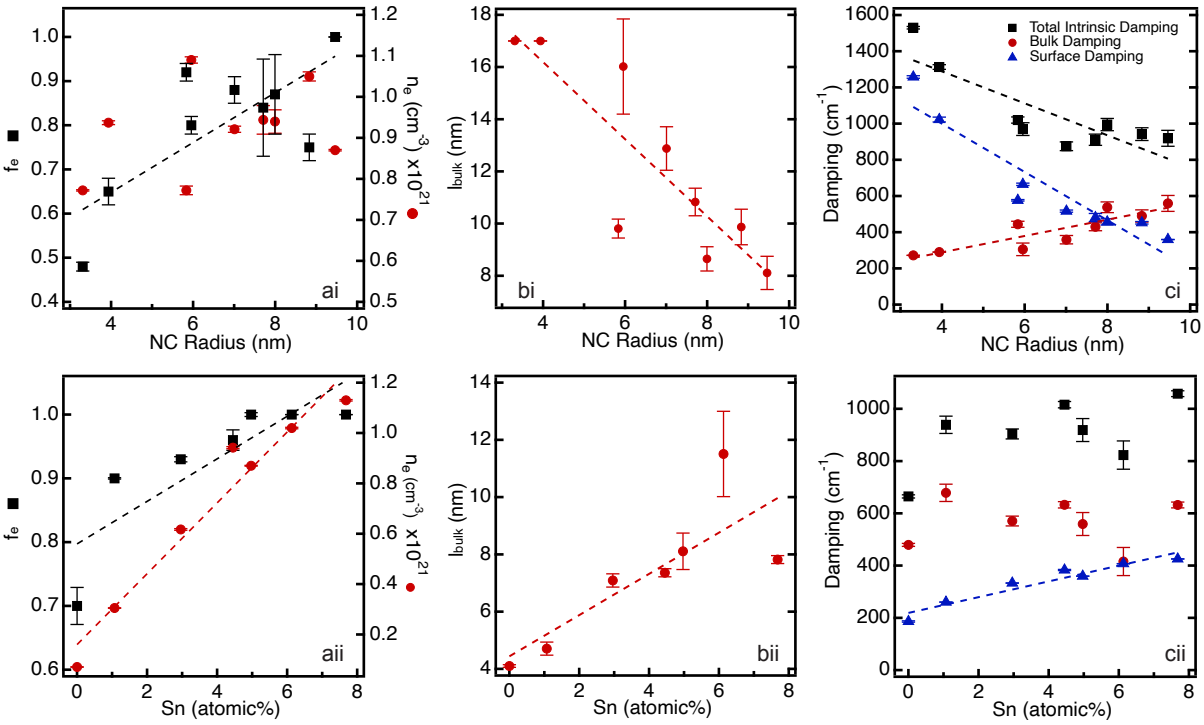

Figure 3.5: HEDA Fit results. Electron accessible volume fraction and free charge carrier concentration as a function of NC radius (ai) and doping level (aii). Bulk mean free path as a function of NC radius (bi) and doping level (bii). Total intrinsic damping as well as its substituent components, bulk and surface damping, as a function of NC radius (ci) and doping level (cii). Dashed lines show linear fits to each sample set with statistically significant correlation. Error bars indicate standard deviation in the results from HEDA fitting for four independently prepared dispersions of each sample.

The bulk mean free path, l_{bulk}, decreases with increasing radius (Figure 3.5bi). We expect the bulk damping in ITO of this dopant concentration to be dominated by electron-phonon scattering,[64] so this trend may suggest a size-dependence in the phonon behavior. However, the dominance of surface over bulk damping for smaller NCs makes this determination tentative based on the present analysis. Increasing l_{bulk} with n_e (Figure 3.5bii) has been theoretically predicted,[89] but due to the difficulty in deconvoluting the various damping mechanisms, most experimental work only reports variations in aggregate carrier damping or mobility with Sn content but does not calculate mean free path.[64] Theoretically, increasing n_e will increase the Fermi velocity of the most energetic electrons but will also increase the frequency of electron scattering events, leaving an unclear prediction for mean free path. Our experimental results suggest the dominant effect of increasing n_e is to increase the mean free path.

These fit results combine to determine the trends in intrinsic damping for ITO NCs. Intrinsic damping reflects the frequency of free electron scattering events in a single NC and can be categorized into two contributions: bulk damping, Γ_{bulk}, and surface damping, $\Gamma_{surface}$. From Equation 3.4, we define bulk and surface damping as

$$\Gamma_{bulk} = \frac{(3\pi^2)^{\frac{1}{3}}\hbar}{m_e^*} n_e^{\frac{1}{3}} \left(\frac{1}{l_{bulk}}\right) \qquad \text{Equation 3.13}$$

$$\Gamma_{surface} = \frac{(3\pi^2)^{\frac{1}{3}}\hbar}{m_e^*} n_e^{\frac{1}{3}} \left(\frac{1}{\frac{4}{3} r_{NC} f_e^{\frac{1}{3}}}\right) \qquad \text{Equation 3.14}$$

Intrinsic damping sharply drops with increasing size up to a radius of ~6 nm, above which damping becomes less size-dependent (Figure 3.5ci). This trend results from the reduction in $\Gamma_{surface}$, even with a steady increase in Γ_{bulk}. In fact, our results show that surface damping is dominant over bulk damping for NCs smaller than ~8 nm in radius.

Rising r_{NC} and f_e drive the reduction in $\Gamma_{surface}$, while diminishing l_{bulk} contributes to the moderate increase in Γ_{bulk}. Intrinsic damping was not correlated with dopant concentration (Figure 3.5cii), contrary to expectations suggested by Equation 3.2. This invariance results from l_{bulk} increasing with dopant concentration, counteracting the effects of increased n_e. The moderate trend in $\Gamma_{surface}$ with doping was not strong enough to drive a trend in total intrinsic damping. While $\Gamma_{surface}$ rises due to growing n_e, it is mitigated by increasing f_e. Reduction in surface damping due to a reduction in depletion layer thickness (increasing f_e) is a significant factor influencing the optoelectronic properties of ITO NCs and is expected to be for other degenerately doped semiconductor NCs.

By removing the contribution of heterogeneous broadening and deconvoluting surface and bulk damping, the HEDA model uncovers trends in NC material properties. It is important that the HEDA model achieves high quality fits for a range of ITO NCs without incorporating frequency-dependent damping, as previously included to modify the simple Drude dielectric function.[19,58,63,65] As ionized impurity scattering is expected to be frequency-dependent, the present success in fitting supports the idea that impurity scattering is not a dominant scattering source for ITO within this doping and size range.

3.3.3 HEDA Fit Results Align with Mie Scattering Theory

While the extinction coefficient is commonly reported on a molar (i.e., number-normalized) basis, it is helpful to report the volume-normalized basis to examine size-dependence of intrinsic properties. The volume-normalized extinction coefficient, ϵ_{NC}, is defined as

$$\epsilon_{NC} = \frac{\sigma_{abs}}{V} \qquad \text{Equation 3.15}$$

A rigorous analysis of Mie theory, as shown in the supporting information of Ref. 23, reveals that the volume-normalized extinction coefficient for a single spherical particle in the quasistatic regime and with $\omega_p \gg \Gamma$ – both conditions that are valid for the ITO NCs in this work – can be well-approximated as

$$\epsilon_{NC} = \frac{18\pi\varepsilon_m^{\frac{3}{2}}}{(\varepsilon_\infty + 2\varepsilon_m)}\left(\frac{\omega_p^2}{\Gamma(\varepsilon_\infty + 2\varepsilon_m)}\right) \qquad \text{Equation 3.16}$$

From this we can calculate the expected extinction of a single NC *a priori* given the values of ω_p and Γ. We note that, in the absence of near-surface depletion regions, extinction increases linearly with $\frac{\omega_p^2}{\Gamma}$; however, when considering the effect of depletion, extinction increases linearly with $f_e \frac{\omega_p^2}{\Gamma}$. This extinction coefficient dependence can be used to check the validity of an optical absorption fitting procedure. The volume-normalized extinction for the ensemble measurements and fit results for all samples are plotted in Figures B3 and B4.

The volume-normalized extinction coefficients extracted from the traditional SDA model with floating volume fraction compare poorly to the theoretically predicted relationship (Figure 3.6a). The disagreement indicates that the extracted fit values are not reconcilable with the expected peak extinction coefficient according to Mie theory. Near-surface depletion and ensemble heterogeneity reduce the volume-normalized extinction observed in ensemble measurements such that the SDA is insufficient to describe the essential physics underlying the LSPR. The SDA is able to simultaneously fit experimental data and yet violate Mie theory by floating f_v to non-physical values, arbitrarily scaling intensity. When the HEDA model incorporates ensemble heterogeneity and surface depletion, the predicted extinction values for the average ITO NC align exactly with that which is predicted by Equation 3.16.

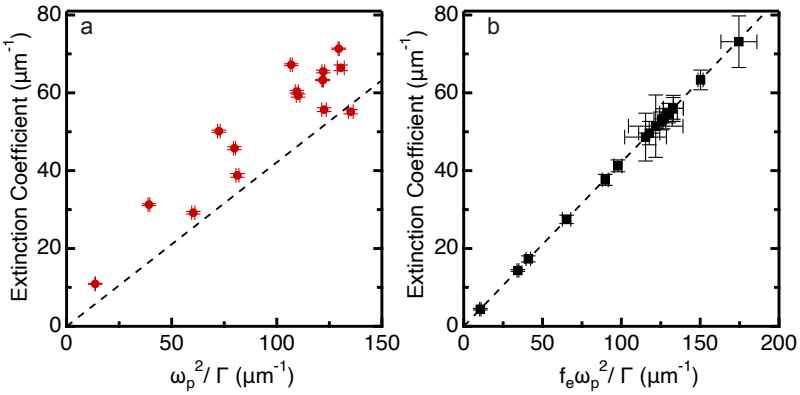

Figure 3.6: Ensemble and average NC extinction. Volume-normalized peak extinction coefficient extracted from SDA (a) and HEDA (b) fits to ensemble spectra. The dashed line indicates the expected extinction coefficient derived from Mie scattering theory. Error bars indicate standard deviation in the results from HEDA fitting for four independently prepared dispersions of each sample.

To further illustrate this point, we can calculate the peak extinction from simulated spectra in Figure 3.2. The peak extinction values (markers) fall in line with the expected value (dashed line) when varying all parameters except for D_{n_e} or f_e (Figure 3.7). The deviation from Mie theory for varying depletion layer thickness can be rectified by normalizing by f_e so that only the volume accessible to free electrons is considered. These calculations emphasize that, in particular, the ability of the HEDA model to account for D_{n_e} and f_e allows it to fit an ensemble spectrum without sacrificing the validity of intrinsic material properties or violating the expectations from Mie scattering theory.

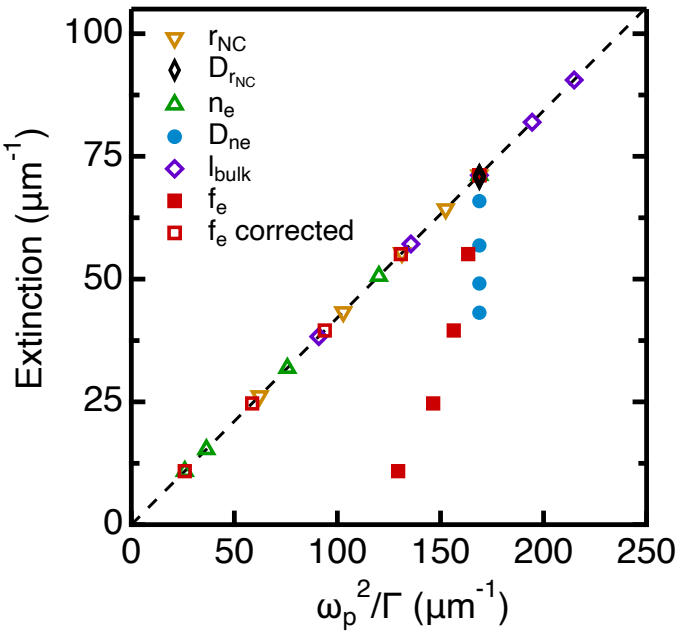

Figure 3.7: Trends in optical extinction. Peak volume-normalized extinction from all spectra plotted in Figure 3.2. The dashed line indicates the expected trend in extinction according to Mie scattering theory within the quasistatic limit for particles with $\omega_p \gg \Gamma$. Ensemble heterogeneity and charge carrier surface depletion cause the peak extinction values to deviate. Using f_e as a correction factor, the theory and calculated are in agreement.

For these reasons, when using HEDA fit parameters to calculate the volume-normalized extinction coefficient for an average (representative) NC in each ensemble, the peak extinction values fall directly in line with theory (Figure 3.6b). The success of the HEDA model in uncovering intrinsic NC properties as well as the effect of ensemble heterogeneity can elucidate the critical parameters for improving key optical and electronic properties such as Q-factor and carrier mobility.

3.3.4 Optical and Electronic Properties Derived from HEDA Model Fit Results

The Q-factor of a NC ensemble not only depends on intrinsic NC properties, but also on ensemble heterogeneity. The HEDA model diagnoses how to improve the optical performance for a batch of NCs. Because damping significantly decreases with increasing

NC radius and ω_{LSPR} blue-shifts with higher doping, it follows that the Q-factor (a ratio of ω_{LSPR} to FWHM) increases with both radius and doping (Figures 3.8a and 8b). In agreement with prior work, Q-factors for ensemble spectra ($Q_{ensemble}$) spanned the range of 2.0 to 4.6.[91] Using parameters derived from the HEDA model, the Q-factor for the average NC within each ensemble (Q_{NC}) was calculated and compared to $Q_{ensemble}$. Q_{NC} was notably higher than $Q_{ensemble}$ for nearly all samples, with the maximum ratio reaching 1.8-fold for a 6 at% Sn 20 nm ITO NC with Q_{NC} of 6.2. To our knowledge 6.2 is higher than any reports of $Q_{ensemble}$ for ITO NCs. The ratio of Q_{NC} to $Q_{ensemble}$ strongly correlates with D_{n_e} (Figure 3.8c), emphasizing the potential enhancements to ensemble quality factor achievable when narrowing the distribution in n_e. While a perfectly uniform ensemble of doped NCs is unachievable, the rise in Q-factor across nearly all samples motivates the pursuit of reducing ensemble heterogeneity.

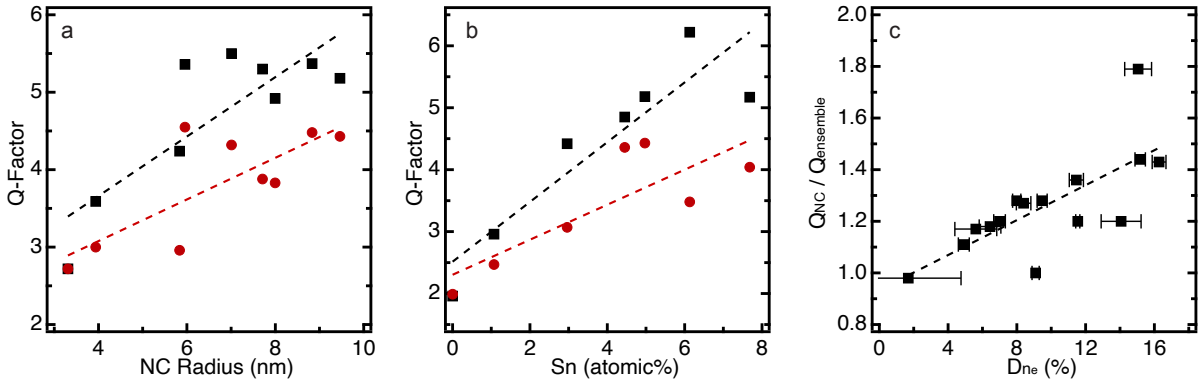

Figure 3.8: Ensemble and average NC optical properties. Q-factor calculated from the ensemble spectrum ($Q_{ensemble}$, red circles) and the spectrum of the average NC within that ensemble acquired through HEDA modeling (Q_{NC}, black squares) as a function of NC radius (a) and doping level (b). Ratio of Q_{NC} to $Q_{ensemble}$ as a function of carrier concentration polydispersity (D_{n_e}) for all ITO NC samples. Dashed lines show linear fits to each sample set with statistically significant correlation. Error bars indicate standard deviation in the results from HEDA fitting for four independently prepared dispersions of each sample.

In parallel to optical properties, quantification of electronic properties of interest, such as mobility and conductivity, benefit from decoupling the intrinsic properties from heterogeneous broadening. While the electronic properties of thin films are readily measured and understood, these properties are significantly more complicated to rationalize and define for films comprised of NCs. Optical analysis of intrinsic properties can be significantly enabling for such analyses. For example, although inter-NC charge transfer is a key bottleneck in achieving high electronic performance in thin films of NCs, it is not easily measured directly.[92] Instead, inter-NC resistance in metal oxide NC films has been calculated by measuring overall film resistance and subtracting the contribution of intra-NC resistance determined using fits to optical extinction data.[20,83,93] The accuracy of calculated values for inter-NC resistance is determined by the quality of the optical fits. The intra-NC conductivity and mobility are calculated from the electron concentration and damping constant determined by optical fitting. Once the heterogeneous contributions are eliminated, the average NC spectrum indicates the intrinsic damping is less than would be reported using a conventional SDA fitting approach. We compared damping extracted from SDA, referred to as ensemble damping ($\Gamma_{ensemble}$), to that of an average NC determined using HEDA fitting, i.e. intrinsic damping (Γ). The difference between $\Gamma_{ensemble}$ and Γ illustrates how the extracted fit parameters can differ when heterogenous broadening and intrinsic damping are convoluted and deconvoluted, respectively (Figure 3.9a). The SDA gives an ensemble damping value that is, on average, 19% higher than the intrinsic damping provided by the HEDA model. The maximum disparity between damping values was 65% for the 20 nm 6.5 at% Sn ITO sample, which also had one of the highest values of carrier concentration polydispersity (Figure 3.4b). Further, the two cases where SDA damping and HEDA intrinsic damping are in near agreement are 20 nm 0 at% Sn ITO and

6 nm 5 at% Sn ITO, which are dominated by intrinsic damping due to low carrier concentration polydispersity and high surface damping, respectively.

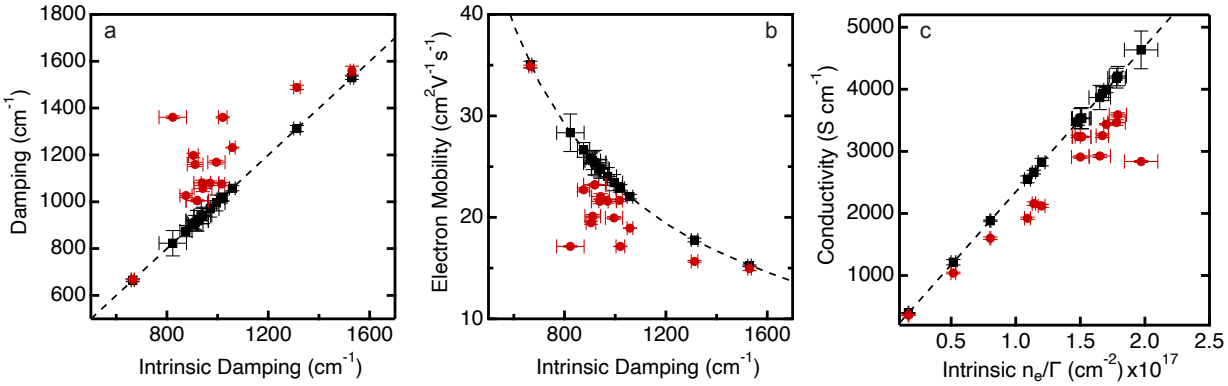

Figure 3.9: Ensemble and average NC electronic properties. Ensemble damping ($\Gamma_{ensemble}$) as fit by the SDA model with floating volume fraction (red circles) and intrinsic damping (Γ) calculated from HEDA model fit parameters (black squares) (a). Fitted damping and electron concentrations were used to calculate electron mobility (b) and conductivity (c). Dashed lines calculate the electronic parameters extrapolated beyond values extracted from our sample sets. Error bars indicate standard deviation in the results from HEDA fitting for four independently prepared dispersions of each sample.

Electron mobility is an important electronic parameter for semiconductors, describing how quickly an electron moves through a material experiencing an applied electric field. Following directly from the observed differences in damping, the SDA-derived ensemble mobility is significantly lower than the intrinsic mobility (Figure 3.9b). The HEDA-derived intrinsic mobility includes a significant contribution from surface damping, which is not present in ITO thin films where reported electron mobilities range from ~20 to ~80 cm^2/Vs. However, as described previously, the HEDA model also deconvolutes intrinsic damping into surface damping and bulk damping (Figures 3.5ci and 3.5cii). From the HEDA-derived bulk damping values, the bulk mobility calculated for these ITO NCs ranges from ~35 cm^2/Vs to ~85 cm^2/Vs, nearly identical to the range of

literature values for ITO thin films with thickness much greater than l_{bulk} (Figure B5a).[64,94] Correctly reproducing bulk ITO mobility provides is powerful evidence for the efficacy and accuracy of the HEDA model and its ability to deconvolute the contributions of various damping mechanisms.

Optically derived intra-NC conductivity is calculated from the Drude conductivity equation using electron mobility and electron concentration in both the ensemble and intrinsic cases (Figure 3.9c). The maximum ensemble intra-NC conductivity found is about 3600 S/cm. In contrast, the HEDA model derived intrinsic intra-NC conductivity has a maximum of nearly 4700 S/cm, 30% higher. Such deviations have major impacts on understanding electron conduction through NC films. For example, accurate intrinsic properties are necessary to pin down design parameters for NC films such as the critical value of inter-NC resistance, below which NC films behave as metallically conductive thin films. The bulk conductivity calculated for these NCs, setting aside the effects of surface damping, ranges from ~550 S/cm to ~13400 S/cm (Figure B5b), once again matching thin film literature.[64,94]

3.4 CONCLUSIONS

The standard SDA procedure for fitting optical extinction yields results that overestimate intrinsic damping and violate Mie scattering theory for even the most synthetically refined NC ensembles, which nonetheless have significant dopant heterogeneity and surface depletion. A novel fitting procedure was generated to rectify the shortcomings of the SDA model. The HEDA model was proven valid based on optical fits for a wide range of NC sizes and doping levels that produced results that (1) agree Mie Scattering theory and (2) derive electronic mobility and conductivity that match well with empirical thin film literature. The HEDA model quantifies how LSPR peak shape, position,

and intensity result from contributions of depletion layer thickness, surface damping, bulk damping, as well as n_e and Γ heterogeneity – a richer trove of information when compared to obtaining only ω_p and Γ from the SDA. With these values in hand, we rationalized trends in ITO NCs with varying dopant concentration and radius.

In the size regime investigated here, intrinsic damping has significant contributions from surface damping. Thus, the average size of the NC had a strong impact on overall damping, but with $D_{r_{NC}}$ at or below 10%, size polydispersity was not a strong contributor to heterogeneous broadening. Heterogeneous broadening mainly resulted from NC-to-NC variations in electron concentration. Our results suggest that to improve the ensemble extinction it will be more effective to narrow dopant heterogeneity. Because the polydispersity is significantly above that dictated by the Poisson limit, this is a physically realizable goal. When we quantified mean free path and subtracted the contribution of surface damping, our analysis recovers bulk electron mobility and conductivity values comparable to those measured in thin films. This agreement between electronic properties of NCs and conventional thin films indicates that colloidal synthesis produces materials of high electronic quality. We expect this model is valid for isotropic plasmonic particles within the quasistatic regime of any material class. By extrapolating this one-dimensional model into two or three dimensions, we expect anisotropic particles could also be reliably modeled and their properties analyzed.

Chapter 4: Segregating Dopants within Semiconductor Nanocrystals

In Chapter 3, we discussed how trap states at the NC surface can result in a significant decrease in free electron concentration near the surface (a surface depletion layer) and result in a nonuniform intra-NC electron concentration profile. In this chapter, we manipulate the intra-NC electron concentration profile by (i) "cleaning" the surface of trap states and (ii) engineering the intra-NC doping profile. These processes have dramatic effects on the electronic (Section 4.1) and optical (Section 4.2) response of ITO NCs.

4.1 Tuning Nanocrystal Surface Depletion By Controlling Dopant Distribution as a Means to Route toward Enhanced Film Conductivity

So far, we have dived deeply into optical characterization of NC dispersions, but much of doped metal oxide NC utility comes from their ability to be cast as electronic inks onto flexible substrates. This can confer their conductive and optically responsive properties to a wide range of materials. However, to remain stable in dispersion, colloidal NCs are typically capped with organic ligands that then act as insulating barriers to electronic conduction when cast into films. It is essential to understand how to enhance conductivity between neighboring NCs in order to enable their application in flexible electronics.[**]

4.1.1 Mitigating Depletion through Chemical Modification of the NC Surface

As mentioned earlier, TCO films represent a potential application of doped metal oxide NCs, for which conductivity is an essential design parameter. Electron transport in NC films typically proceeds through a series of inelastic tunneling events, so-called

**This section contains text and figures adapted from Ref. 17, which was written by Stephen L. Gibbs as lead author in collaboration with Corey M. Staller and Delia J. Milliron. It has been adapted with permission from the authors. Copyright 2019 American Chemical Society

hopping conduction, and depletion layers pose a barrier at each hopping step.[95,96] Hopping conduction is described in the most general case by the Miller-Abrahams model:[97]

$$\sigma \propto Aexp\left(-\frac{2r_{ij}}{a}\right)\ exp\left(-\frac{E_{ij}}{k_B T}\right) \qquad \text{Equation 4.1}$$

where σ is conductivity, A is a material-dependent constant, r_{ij} is the distance between sites i and j, a is the inverse of the wavefunction decay rate (i.e. the electron localization length), and E_{ij} is the energetic barrier encountered moving from site i to j. The depletion layer separates the electron localization volumes in neighboring NCs, increasing r_{ij} and consequentially decreasing film conductivity.

Measuring electronic conductivity of NC films can be a sensitive tool for monitoring changes to depletion width and determining their chemical and physical origins. Thimsen et al observed that highly resistive films of bare 6.5 nm zinc oxide (ZnO) NCs were made >8 orders of magnitude less resistive following the deposition of alumina by atomic layer deposition (ALD).[98] They proposed this effect was the result of trimethylaluminum (TMA) reacting with adsorbed water species (i.e. surface hydroxyls), which form mid-band gap surface states on metal oxide surfaces. Based on the discussion above, alumina deposition may therefore be expected to alleviate depletion, thereby reducing barriers to electron hopping. Another possibility, namely that alumina causes interfacial doping of ZnO NCs, was acknowledged by the authors. Following up, Ephraim et al ruled out interfacial doping and further substantiated that removal of adsorbed water species is responsible for enhanced conductivity in alumina ALD-capped NC films.[21] First, the possibility of n-type doping due to formation of substitutional defects, $Al_{Zn}^{\bullet}$, was eliminated by depositing alumina on ITO, Al_{In}^{x}, NC films (Figure 4.1A). A 1-2 order of magnitude decrease in sheet resistance was observed. The modest improvement to ITO NC

film sheet resistance compared to ZnO NC films is attributed to the higher dopant concentration in ITO NCs resulting in a thinner depletion layer before ALD.

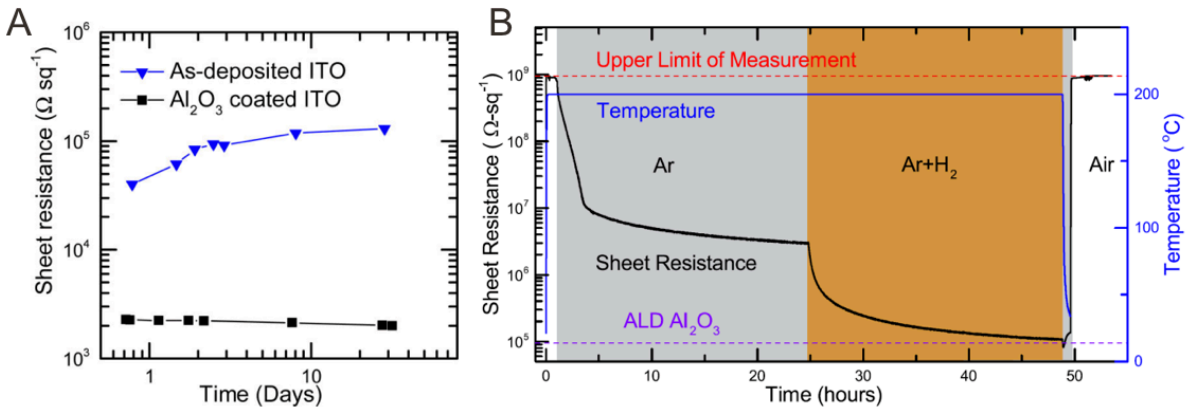

Figure 4.1: Identifying adsorbed water species as a surface state in metal oxide NCs using in situ sheet resistance measurements. (A) Bare and alumina-capped ITO NC films. (B) ZnO NC films during exposure to inert and forming gas. Adapted from Ref 21. Copyright 2016 American Chemical Society.

Second, Ephraim et al conducted *in situ* measurements of bare ZnO NC films under exposure to Ar gas and 15% H_2 in Ar gas (forming gas) at 200°C (Figure 4.1B). Heating to 200°C in Ar removes physisorbed water from the NC surfaces, resulting in a >2 order of magnitude decrease in sheet resistance. Forming gas is known to remove chemisorbed water species from metal oxides. The NC film sheet resistance, upon exposure to forming gas, asymptotically approaches the sheet resistance of a ZnO NC film with alumina-capped surfaces. These results confirmed the decrease in NC film resistivity was due to the removal of hydroxyls at the metal oxide surface.

4.1.2 Tuning the Depletion Width by Controlling Intra-NC Dopant Distribution

Because hydroxylation of metal oxide surfaces is spontaneous in ambient conditions, strategies for controlling *W* are of high importance. For many applications,

embedding NCs in alumina is not feasible as it renders the NCs non-dispersible and prevents access to the NC surface for sensing, detection, and catalysis. Hence, the ability to control depletion without modifying the surface is valuable. We've discussed the narrowing of depletion width in highly doped NCs; however, depletion layer compression is possible even for lightly doped NCs if the dopants are concentrated in the near-surface region where they can screen the surface potential. Staller et al leveraged advances in metal oxide NC synthesis[61–63] to control the radial dopant distribution in 20 nm ITO NCs while holding the overall NC dopant concentration at 3 at% Sn.[20] This control was afforded by a slow-injection synthesis in which NC cores of a given dopant concentration and size are synthesized and purified, then used as seeds for a shelling procedure, where the shell dopant concentration and thickness are tunable.

The conductivity of bare NC films was found to exponentially depend on near-surface dopant concentration over a conductivity range spanning about an order of magnitude (Figure 4.2A). This trend supports the hypothesis that W is reduced as near-surface dopant concentration increases. This explanation was verified by passivating NC surfaces by alumina ALD to ameliorate the effects of depletion on NC film conductivity, after which all samples showed a 1-2 order of magnitude increase in conductivity. Importantly, the alumina-capped films show no apparent dependence of film conductivity on near-surface dopant concentration, consistent with the conclusion that, at constant overall doping, the extent of the depletion layer is the determining factor in electronic conductivity.

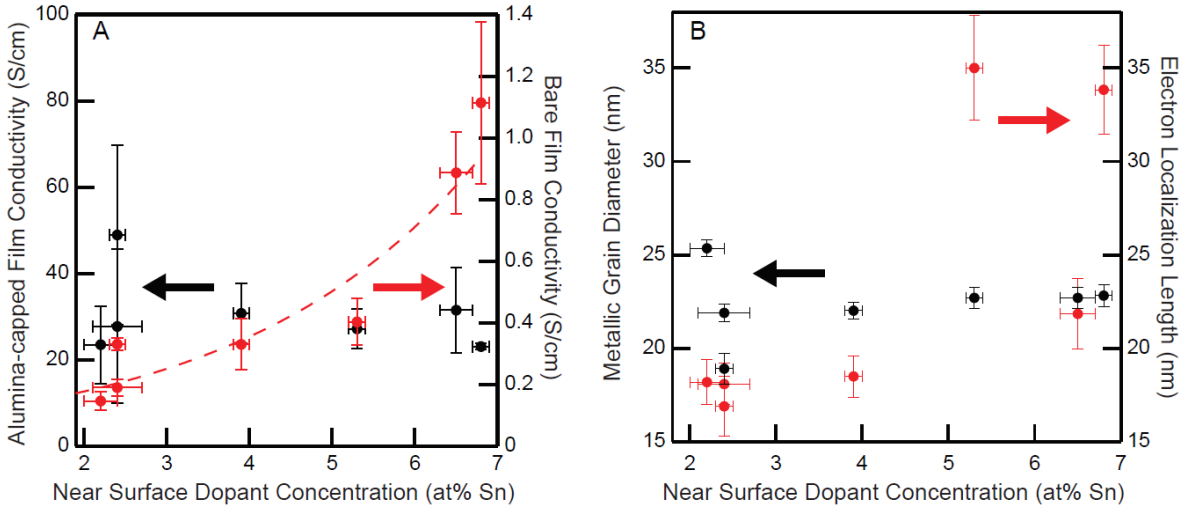

Figure 4.2: NC film conductivity dependence on near-surface dopant concentration before and after alumina ALD. (A) Room temperature conductivity of bare ITO NC films (red) and alumina-capped ITO NC films (black). Note that the scales of the two y-axes are very different (B) Extracted values for electron localization length in bare NC films (red) and metallic grain diameter in alumina-capped NC films (black). Adapted from Ref. 20. Copyright 2018 American Chemical Society.

Fits to variable temperature conductivity support the conclusions drawn from room temperature measurements about how depletion impacts electron transport in NC films. Based on the temperature dependence, bare NC films were found to conduct electrons through Efros-Shklovskii variable range hopping with a Gaussian dispersion of energy levels (ES-VRH-GD).[99] In this conduction mechanism, the diameter of the non-depleted core is defined by the electron localization length. By fitting to the ES-VRH-GS model, the electron localization lengths of bare NC films were determined to be longer for higher near-surface dopant concentration, consistent with a compression of *W* (Figure 4.2B). After capping with alumina by ALD, film conductivity increased by 1-2 orders of magnitude and electron transport in NC films was found to follow a granular metal conduction mechanism.[100,101] In this conduction mechanism, the analogous metric to localization length is the metallic grain size. Figure 4.2B shows the metallic grain size for

alumina-capped films is independent of near-surface dopant concentration and is approximately equal to the NC diameter (20 nm), meaning W is nearly zero. This confirms that the dependence of bare NC film conductivity on near-surface dopant concentration arises from variation in depletion layer thickness.

Going one step further, carrier concentration profiles were simulated in COMSOL Multiphysics ® for some of these samples. The simulations illustrate carrier concentration profiles for 3 at% Sn, 20 nm diameter ITO NCs of differing radial doping profiles (Figure 4.3).

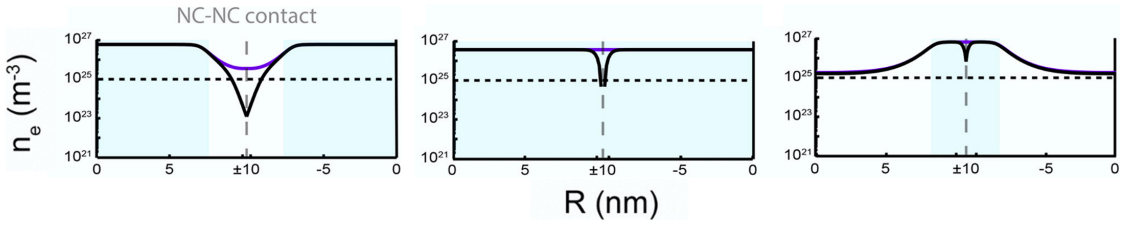

Figure 4.3: Carrier concentration profiles for NCs of different radial doping distribution. All NCs have ~3 at% Sn overall and are ~20 nm in diameter. The core-doped NC (left) has a 14.4 nm core of 8% Sn with an undoped indium oxide shell. The uniformly doped NC has 3 at% Sn throughout, and the shell-doped sample (right) has an undoped core of 16.5 nm and an 8 at% Sn shell. Adapted from Ref 20. Copyright 2018 American Chemical Society.

The simulations show that marching the dopant density outward, from core to surface, not only mitigates the depletion width, but alters the carrier concentration profile throughout the NC. This had the effect of increasing localization length and increasing NC film conductivity, but how could this effect the optical properties?

4.2 Dual-Mode Infrared Absorption by Segregating Dopants within Plasmonic Semiconductor Nanocrystals

We have now seen that when aliovalent dopants are sufficiently segregated to the core or near the surface of semiconductor nanocrystals, charge carriers donated by the dopants are also segregated to the core or near the surface, respectively. In ITO, we find

that this contrast in free charge carrier concentration creates a core and shell with differing dielectric properties and results in two distinctly observable plasmonic extinction peaks. The trends in this dual-mode optical response with shell growth differ from core/shell nanoparticles composed of traditional plasmonic metals such as Au and Ag. We developed a model employing a core/shell effective medium approximation that can fit the dual-mode spectra and explain the trends in the extinction response. Lastly, we show dopant segregation can improve sensitivity of plasmon spectra to changes in refractive index of the surrounding environment.††

4.2.1 Introduction

Plasmonic nanoparticles efficiently collect incident light and confine it to nanoscale volumes, which can drive enhanced electric fields,[30,102,103] localized heating,[39,104] and hot electron transfer.[105–107] Degenerately doped semiconductor NCs have proven to be efficient infrared plasmonic materials due to their intrinsically low plasmon damping and their low and easily tunable charge carrier concentration.[16,67] The plasmonic response of doped semiconductor NCs of various sizes, shapes, and compositions has been well-studied,[108–110] but the distribution of dopants within a NC can also tune the optical behavior.[58,63] With the recent advent of slow-addition synthetic techniques for doped metal oxide NCs, we have greater control over the intra-NC radial doping profile than ever before.[61–63] This control elucidated that deliberately segregating aliovalent dopants to the surface (core) also segregates the majority of the charge-compensating free carriers derived from those dopants to the surface (core).[17,20] The potential established by space-charge buildup at the interface of the doped and undoped regions prevents charge carriers from distributing

††This section contains text and figures adapted from Ref 25, which was written by Stephen L. Gibbs as lead author in collaboration with Christopher Dean, Joey Saad, Bharat Tandon, Corey M. Staller, Ankit Agrawal, and Delia J. Milliron. It has been adapted with permission from the authors. Copyright 2020 American Chemical Society

homogeneously throughout the nanocrystal. In other words, an inhomogeneous doping profile leads to an inhomogeneous charge carrier profile, even within a single nanocrystal. Leveraging this knowledge, the conductivity of NC films has been improved by segregating dopants near the NC surface (Section 4.1).[20] Motivated by these results, we sought to understand how engineering the intra-NC carrier concentration profile through dopant segregation impacts the plasmonic response.

Plasmonic structures with radially inhomogeneous compositions have already been employed to tune the optical response for traditional plasmonic materials such as Au and Ag. Most notably, silica@Au (core@shell) nanoshells were synthesized to bring the LSPR peak of Au from the visible to the near-IR therapeutic window, enabling the demonstration of photothermal therapy in animal tissue.[39] Beyond shifting the peak extinction to lower energy, fundamental studies uncovered a dual-mode extinction spectrum from silica@Au nanoshells. More recently, bimetallic core@shell nanoparticles were synthesized and also exhibited dual-mode extinction.[111–113] These distinct modes arise because, unlike a homogeneous sphere, the core and shell are distinguishable due to the abrupt change in composition and dielectric properties at the core/shell boundary. Two surfaces emerge that can support plasmonic modes: the core/shell boundary and the nanoparticle outer surface.[114,115] In a similar way, herein we prove that the segregation of dopants, and therefore charge carriers, within metal oxide nanocrystals creates an epitaxial core/shell boundary that promotes a dual-mode plasmonic response. The observed trends in the plasmonic extinction spectrum differ from those seen in silica@Au and bimetallic core@shell nanoparticles due to unique considerations of doped semiconductor NCs including dopant activation and charge carrier diffusion.

Specifically, we investigate the effect of intra-NC radial dopant distribution on the optical response of ITO NCs. We use this material as a model system for degenerately

doped metal oxides because it is an industrially relevant transparent conductive oxide and colloidal synthesis of both undoped indium oxide (IO) and ITO NCs is well-developed.[61,62] We synthesize two series, one with an undoped core and a doped shell of increasing thickness and another with a doped core and an undoped shell of increasing thickness. We observe a dual-mode plasmonic extinction response in both cases. After building a model that accounts for a radially nonuniform intra-NC charge carrier profile, we were able to reliably fit all collected spectra and extract electronic parameters that explain the evolution of the dual-mode spectra. We show that dopant segregation expands the synthetic tunability of the optical response and enhances sensitivity to the surroundings when compared to uniform doping. Lastly, these findings may resolve the origin of anomalous, asymmetric lineshapes of plasmonic doped metal oxide NCs that have gone unexplained in previous literature.[63,66,116]

4.2.2 Shell-Doped Series

Radial segregation of dopants has been shown to influence peak position, peak width, and peak asymmetry,[58,63,65,66] but no published studies of dopant segregated NCs have identified dual-mode extinction spectra. In the shell-doped (SD) series, aliquots were taken as a shell of 5 at% Sn was epitaxially grown over an undoped IO core as detailed in Appendix C, Text C1. Additional material characterization, including ICP-AES, X-ray photoelectron spectroscopy (XPS), and visible & infrared spectroscopy is detailed in Appendix C, Text C2-C4. During shell growth we observe the appearance and progressive strengthening of a secondary extinction mode at substantially higher energy than the main LSPR peak (Figure 4.4a). Relatively weak peaks between 2000 and 4000 cm^{-1} are assigned to molecular vibrational modes for species on or near the NC surface (Appendix C, Figure C1).

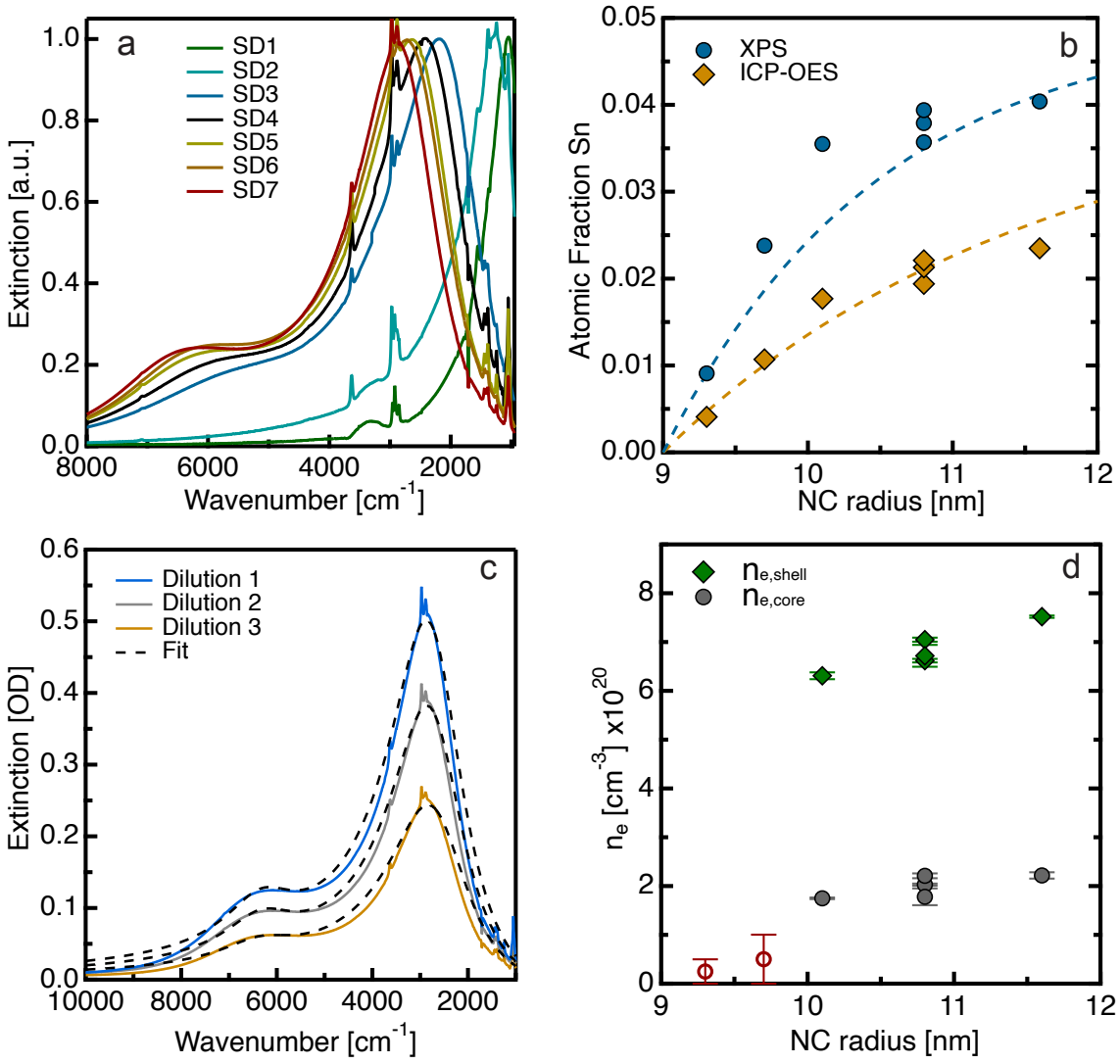

Figure 4.4: Experimental trends in shell-doped NCs. (a) Normalized experimental extinction spectra for the shell-doped series. (b) ICP-OES and XPS quantification of at% Sn for each sample. Dashed lines indicate theoretical values based on measured STEM diameters and a photoelectron escape depth 1.5 nm. (c) Fits to spectra of SD7 at three NC concentrations. (d) Carrier concentration values for the core and the shell extracted by fitting to the core/shell MG-EMA model. Red, hollow circles indicate samples that were fit to a uniform dielectric function – not a core/shell effective medium approximation. Error bars represent the standard deviation in fit results when fitting the optical response of three independently prepared dispersions of varying NC concentration.

XPS and ICP-AES quantified near-surface Sn and overall Sn, respectively. The data confirms that the dopants are indeed segregated to the surface, with near-surface Sn

concentration exceeding the overall Sn concentration by a factor of two on average for all samples (Figure 4.4b). In fact, our experimental results match very well with the theoretically calculated values for both XPS and ICP-AES (dashed lines). To calculate these theoretical values we used the diameters meaured using STEM and approximated the photoelectron escape depth as 1.5 nm.[117] Sample details are reported in Table 4.1, with radius, shell thickness, and core volume fraction ($F_{v,core}$) calculated from particle sizes acquired through STEM (Figure 4.5).

Table 4.1: Experimentally measured properties of shell-doped samples.

Sample	Radius ± 1σ [nm]	Shell Thick ± 1σ [nm]	$F_{v,core}$ ± 1σ	at% Sn by ICP-OES ± 1σ	at% Sn by XPS
SD0	9.0 ± 0.7	0	1	-	-
SD1	9.3 ± 0.7	0.3 ± 0.9	0.92 ± 0.28	0.41 ± 0.01	0.9
SD2	9.7 ± 0.7	0.7 ± 1.0	0.79 ± 0.24	1.07 ± 0.03	2.4
SD3	10.1 ± 0.6	1.1 ± 0.9	0.71 ± 0.19	1.77 ± 0.07	3.6
SD4	10.8 ± 1.0	1.9 ± 1.2	0.57 ± 0.20	1.94 ± 0.05	3.6
SD5	10.8 ± 0.8	1.8 ± 1.0	0.58 ± 0.17	2.13 ± 0.03	3.8
SD6	10.8 ± 0.6	1.8 ± 0.9	0.58 ± 0.15	2.21 ± 0.03	3.9
SD7	11.6 ± 0.7	2.6 ± 1.0	0.47 ± 0.13	2.35 ± 0.04	4.0

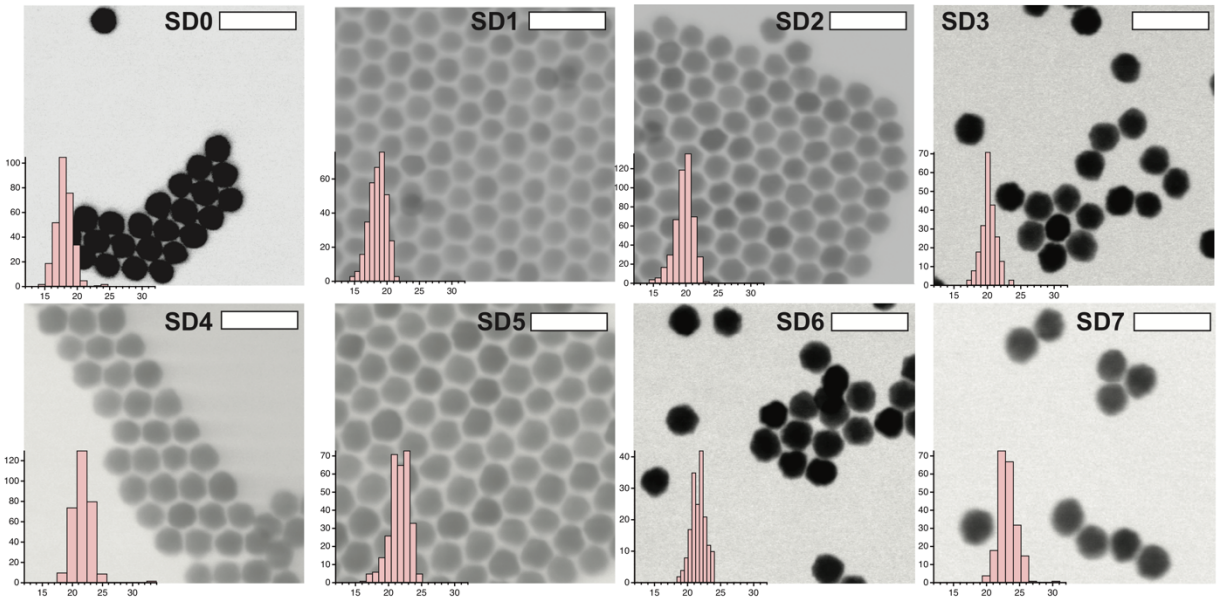

Figure 4.5: STEM images and size histograms of the shell-doped series. Scale bars 50 nm.

The difference in Sn content measured by the two techniques suggests that the change in Sn concentration is abrupt between core and shell, more than reported previously.[63] In that case, a temporally varying precursor composition was slowly injected in a single-pot reaction to control the radial Sn doping profile, but without the extra step of isolating and purifying the undoped cores before starting shell growth – as is done in this work. We conclude that the isolation of NC cores as an intermediate product is an important step in sharpening the dopant profile at the core/shell interface while still maintaining epitaxial growth of single crystal nanoparticles.[20,61]

A sharper dopant profile creates a steeper step in the electrostatic potential and a stronger segregation of charge carriers to the doped region.[17,20] This sharp delineation is reminiscent of the aforementioned silica@Au nanoshells and bimetallic core@shell nanoparticles that also supported two distinct modes. However, the evolution of the two modes is not what we expected based on the plasmon hybridization theory.[114] According

to this theory, as the thickness of the metallic shell grows, the higher energy mode should red-shift and the lower energy mode should blue-shift, bringing them closer together. We observe a blue-shift in both modes (Figure 4.4a). This discrepancy is not surprising because we know that the carrier concentration in ITO NCs increases with size due to increased dopant activation.[23,58] Dopant activation is the ratio between the free electron concentration, n_e, and the dopant concentration. Near-surface dopants are more likely to be "inactive", meaning they are charge-compensated by a mechanism other than with free charge carriers. The fraction of near-surface Sn drops with doped shell growth due to diminishing surface area to volume ratio, causing dopant activation and n_e to increase. No analogous change in n_e is expected for growth of Au or Ag shells. We sought to fit the spectra to a model that could account for changing dielectric properties of the core and shell.

4.2.3 Extracting Electronic Parameters

We built a model to fit our experimental spectra to extract electronic parameters and examine their evolution with shell thickness. The code can be found in the supporting information of Ref. 25. Using a least squares fit function in MATLAB®, we fit for plasma frequency, ω_p, and damping, Γ, in both the core and the shell. The polarizability of a spherical particle with a core and shell having different dielectric properties can be well-approximated using an electromagnetic mixing formula known as the Maxwell-Garnett effective medium approximation (MG-EMA),[118] described briefly in Appendix C, Text C5. Also, because the carrier profile is expected to deviate slightly from the doping profile due to diffusion of free electrons, we fit for the volume fraction of the core instead of using $F_{v,core}$ values calculated from STEM diameters. The deceasing trend in $F_{v,core}$ with shell growth determined by fitting the LSPR spectra agrees with the STEM-derived

values (Appendix C, Figure C2). As well, the fitted values consistently fall above the STEM-derived values for the shell-doped nanocrystals. We attribute this offset to diffusion of carriers from the higher n_e shell to the lower n_e core, causing the shell volume to shrink. While there is some diffusion of carriers across the core/shell boundary, the majority of carriers derived from Sn n-type donors are still localized to the shell. The physics governing this diffusion are directly analogous to an n/n+ junction wherein free electrons redistribute locally in the near-junction space-charge region.[20]

Our model reliably fit experimental data for all samples and produced consistent fit results for independently prepared dispersions of varying NC concentration (Figures 4.4c). For fits to all spectra, see the supporting information of Ref 25. We note that samples SD1 and SD2 show only unimodal extinction and so these spectra were fit with the traditional Drude model for particles with a uniform dielectric function. The very low energy peaks are indicative of low n_e throughout the entire NC volume (Figure 4.4d). For samples SD3 – SD7, the trends in n_e clarify the underlying physicochemical changes leading to the emergence and progressive blue-shift in the secondary mode. As the ITO shell grows in thickness, n_e in the shell also increases. As expected, this upward trend results from increasing activation of Sn for thicker shells where a smaller fraction of the dopants are near-surface. For the same reason, uniformly doped 5 at% Sn ITO NCs were previously found to have increasing n_e up to a radius of 12 nm.[23] The carrier concentration in the undoped core is also impacted by growth of an ITO shell, surpassing a value of 2×10^{20} cm^{-3} or about three times the n_e that has been reported for IO NCs with no shell.[23] We understand this elevated n_e to be due to diffusion of electrons from the high carrier concentration shell into the core, the same phenomenon driving the difference between STEM-derived and fit-derived values for $F_{v,core}$. Increasing dopant activation and carrier

diffusion from the shell to the core explain the discrepancy of our results with the plasmon hybridization theory used for Ag and Au core@shell particles.

4.2.4 Core-Doped Series

For the core-doped (CD) series, an undoped IO shell was grown around a 5 at% ITO core. XPS and ICP-AES data once again confirm that the dopants are well-segregated – this time to the core. Near-surface Sn concentration is nearly identical to overall Sn for CD0, indicating uniform distribution of dopants in the ITO core, but as the IO shell thickness grows, values quickly diverge with near-surface Sn becoming undetectable for samples CD6 and CD7 (Figure 4.6b). Sample details and STEM images are reported in Table 4.2 and Figure 4.6.

Segregating dopants to the core will also concentrate the high n_e region to the core. Unlike a dielectric@metal particle, such as silica@Au, a metal@dielectric particle, such as Au@silica, does not produce a dual-mode extinction spectrum because there is only one surface to sustain LSPR. However, as noted for the SD series, the IO region contains a significant, albeit lower than the doped region, population of free electrons and so behaves like a metal, not an insulating dielectric. This metallicity explains the otherwise unexpected appearance and growth of a second mode with IO shell growth (Figure 4.6a). Simulations of bimetallic core@shell particles with the metal of higher ω_p in the core (analogous to our CD series) have shown that with increasing shell thickness, the high energy peak red-shifts and the low energy peak blue-shifts, bringing the peaks closer together. In our CD series, both modes red-shift with shell growth. Once again, the trend in our dual-mode spectra does not match that which is expected for a traditional metal core@shell particle. Using the same core@shell MG-EMA model as for the SD series, we sought to explain the discrepancy.

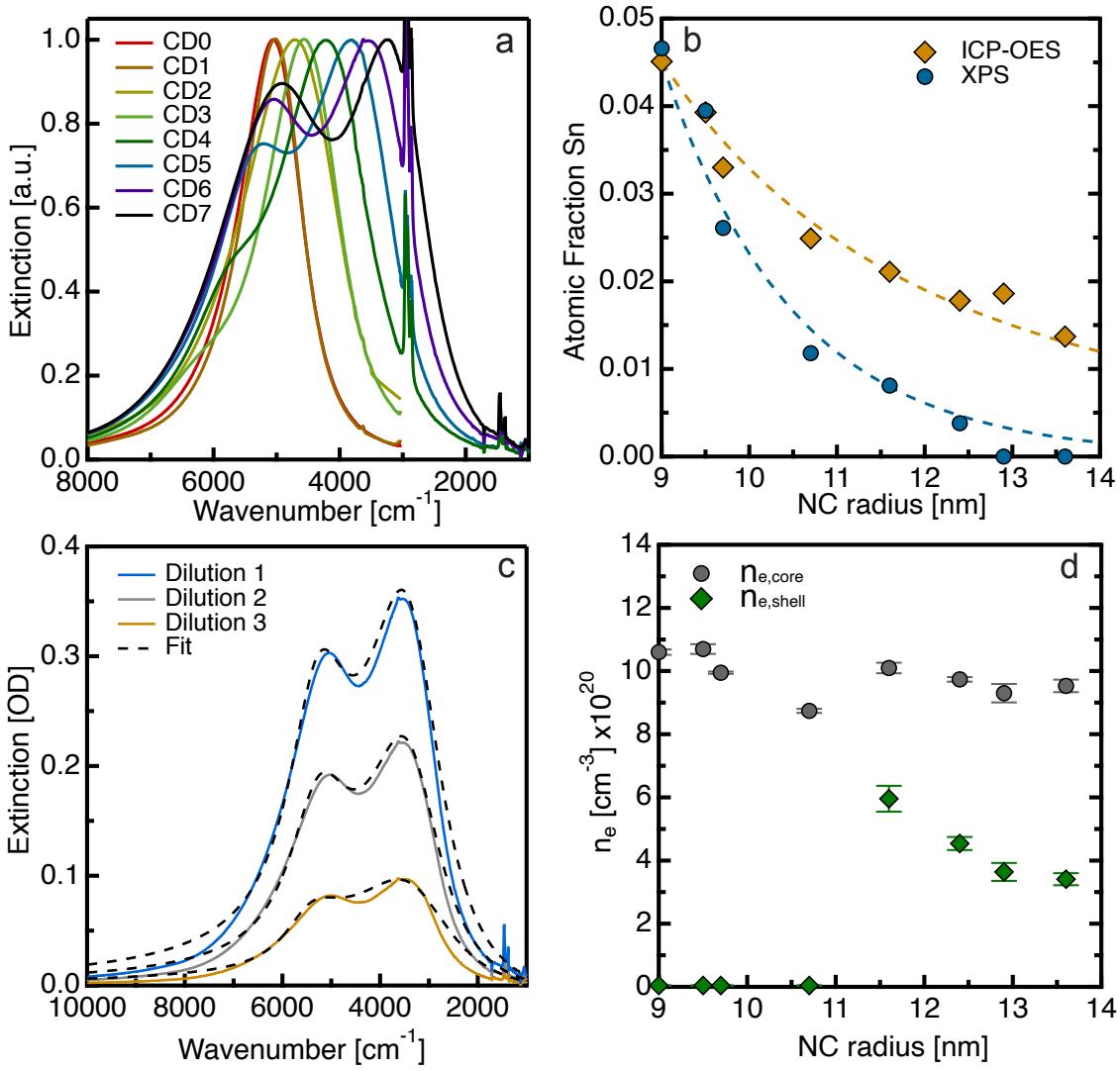

Figure 4.6: Experimental trends in core-doped NCs. (a) Normalized experimental extinction spectra for the core-doped series. (b) ICP-OES and XPS quantification of at% Sn for each sample in the CD series. Dashed lines indicate theoretical values based on measured STEM diameters, a photoelectron escape depth 1.5 nm, and growth of an undoped shell. (c) Fits to spectra of CD6 at three NC concentrations. (d) Carrier concentration values for the core and the shell extracted by fitting to the core/shell MG-EMA model. Error bars represent the standard deviation in fit results when fitting the optical response of three independently prepared dispersions of varying NC concentration.

Table 4.2: Experimentally measured properties of core-doped samples.

Sample	Radius ± 1σ [nm]	Shell Thick ± 1σ [nm]	$F_{v,core}$ ± 1σ	at% Sn by ICP-OES ± 1σ	at% Sn by XPS
CD0	9.0 ± 1.1	0	1	4.51 ± 0.09	4.7
CD1	9.5 ± 0.9	0.6 ± 1.4	0.83 ± 0.39	3.93 ± 0.26	4.0
CD2	9.7 ± 1.0	0.7 ± 1.5	0.79 ± 0.38	3.30 ± 0.14	2.6
CD3	10. ± 1.1	1.8 ± 1.6	0.58 ± 0.28	2.49 ± 0.17	1.2
CD4	11.6 ± 0.9	2.7 ± 1.4	0.46 ± 0.20	2.11 ± 0.19	0.8
CD5	12.4 ± 1.0	3.4 ± 1.5	0.38 ± 0.17	1.78 ± 0.07	0.4
CD6	12.9 ± 1.2	3.9 ± 1.6	0.34 ± 0.16	1.86 ± 0.37	~0
CD7	13.6 ± 0.8	4.7 ± 1.4	0.29 ± 0.12	1.37 ± 0.06	~0

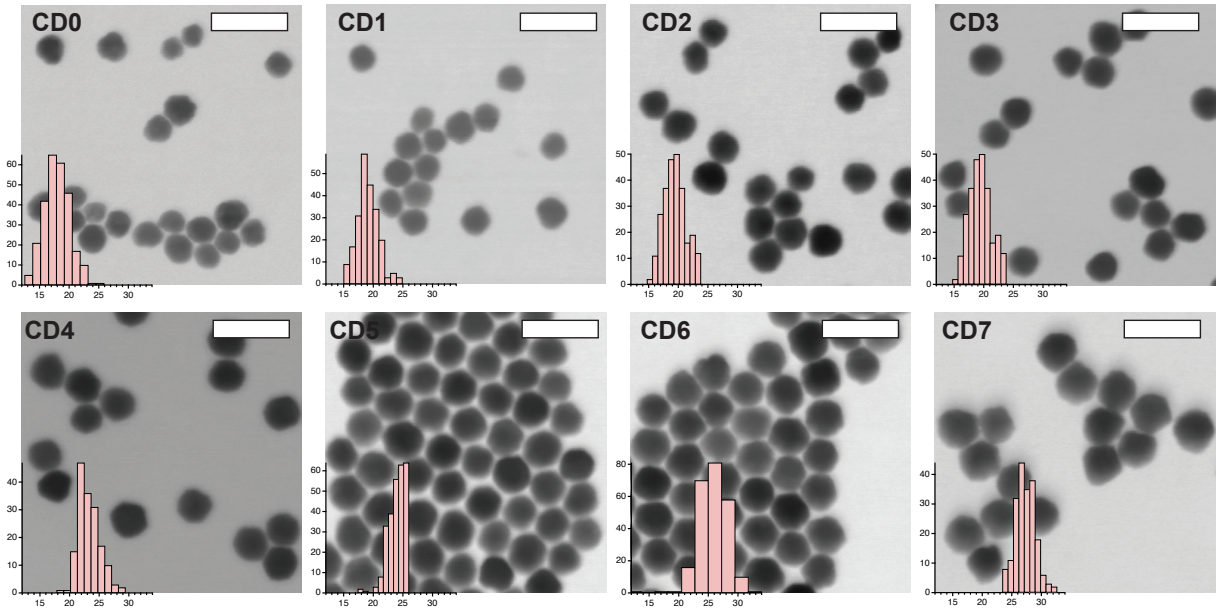

Figure 4.7: STEM images and size histograms of the core-doped series. Scale bars 50 nm.

We achieved excellent fits to the experimental data (Figures 4.6c) and extracted the trends in n_e for the core and shell (Figure 4.6d) as well as $F_{v,core}$. For fits to all spectra, see the supporting information of Ref 25. Consistent with the SD series, the fitted $F_{v,core}$ values trend with the STEM-derived values (Appendix C, Table C2 and Figure C2). Also, the fitted $F_{v,core}$ values consistently fall below the STEM-derived values, indicating carriers diffused from the higher n_e core to the lower n_e shell.

For samples CD0 – CD3 the secondary mode is either absent or subtle, which our model attributes to a high n_e core and a shell nearly devoid of all free electrons, i.e., a surface depletion layer.[17,82] However, when the IO shell reaches a critical thickness, around 2.7 nm, it contains a high enough n_e to support a strong secondary mode. Though n_e in the shell is higher than expected for undoped IO, the core n_e still well-exceeds it. As in the shell-doped NCs, the elevation of n_e in the IO region is understood to originate with diffusion of carriers from ITO. Carrier redistribution near the core/shell interface also explains the decrease in shell n_e with shell thickness for samples CD4 – CD7: for thicker shells the space-charge region near the IO/ITO junction comprises a smaller fraction of the shell volume, causing average n_e across the entire shell to decrease. Just as in the shell-doped case, it is necessary to account for the changing n_e profile with size to rationalize the evolution of the peaks.

In summary, while these experiments illustrated that sufficiently sharp dopant segregation can lead to dual-mode extinction in ITO NCs, we found that the interface still allows some local redistribution of carriers that impacts the optical response. After extracting n_e from the fits, consideration of (1) near-surface dopant activation and (2) charge carrier diffusion at the IO/ITO interface were required to explain why the trends in peak position deviated from the established plasmon hybridization theory for metallic shells and bimetallic core@shell particles. As a first indication of how carrier segregation influences near-field optical properties of doped metal oxide NCs, we next investigated the response of their spectra to a changing dielectric environment.

4.2.5 Dielectric Sensitivity

Plasmonic nanoparticles are commonly employed as sensors because the LSPR peak frequency, ω_{LSPR}, shifts when the dielectric constant of the surroundings changes.[30]

The magnitude of the peak shift is indicative of the strength of the enhanced electric field at the particle surface, i.e., the near-field enhancement.[119–121] The strength of the electric field near the surface determines the effectiveness of many plasmonically powered processes. Principle among these are surface enhanced infrared spectroscopy (SEIRS)[4,31,122,123], enhanced light emission,[102,124] and interparticle coupling.[125–127]

For core@shell particles exhibiting dual-mode extinction (both dielectric@metal and metal@metal), the lower energy mode extends the majority of electric field enhancement outside the particle, whereas the higher energy mode confines much of the enhancement to the core/shell interface.[111] Therefore we expect the lower energy modes to be more sensitive to changes in the surrounding refractive index. To compare dielectric sensitivity for samples of differing dopant distribution, we synthesized uniformly doped, shell-doped, and core-doped samples (Appendix C, Figure C4) with similar ω_{LSPR} for the primary (more intense) peak (Figure 4.8a). We collected spectra for these samples dispersed in four different solvents (Appendix C, Figure C5). The sensitivity factor, $\boldsymbol{S}$, (Table 4.3) is calculated by taking the slope of the line for peak wavelength as a function of solvent refractive index (Figure 4.8b).

Because the primary peak for the shell-doped sample is the lower energy mode and that of the core-doped sample is the higher energy mode, we expect the primary peak of the shell-doped particle to have higher refractive index sensitivity. This is indeed the case. The shell-doped sample is also more sensitive than the uniformly doped sample. We rationalize this difference based on the insulating effect of near-surface depletion.[19,82] While there is notable error in the linear fits to the data, the difference is slopes is large enough to conclude with 95% confidence that the difference in slopes, and therefore the sensitivity factors, is statistically significant. Supporting this understanding, when we fit the optical response of the uniformly doped NCs in TCE using the MG-EMA core@shell

model, we find there is a shell nearly devoid of carriers (Appendix C, Table C3). This insulating effect is mitigated when a higher dopant concentration is segregated near the surface thereby compressing the depletion layer thickness.[20]

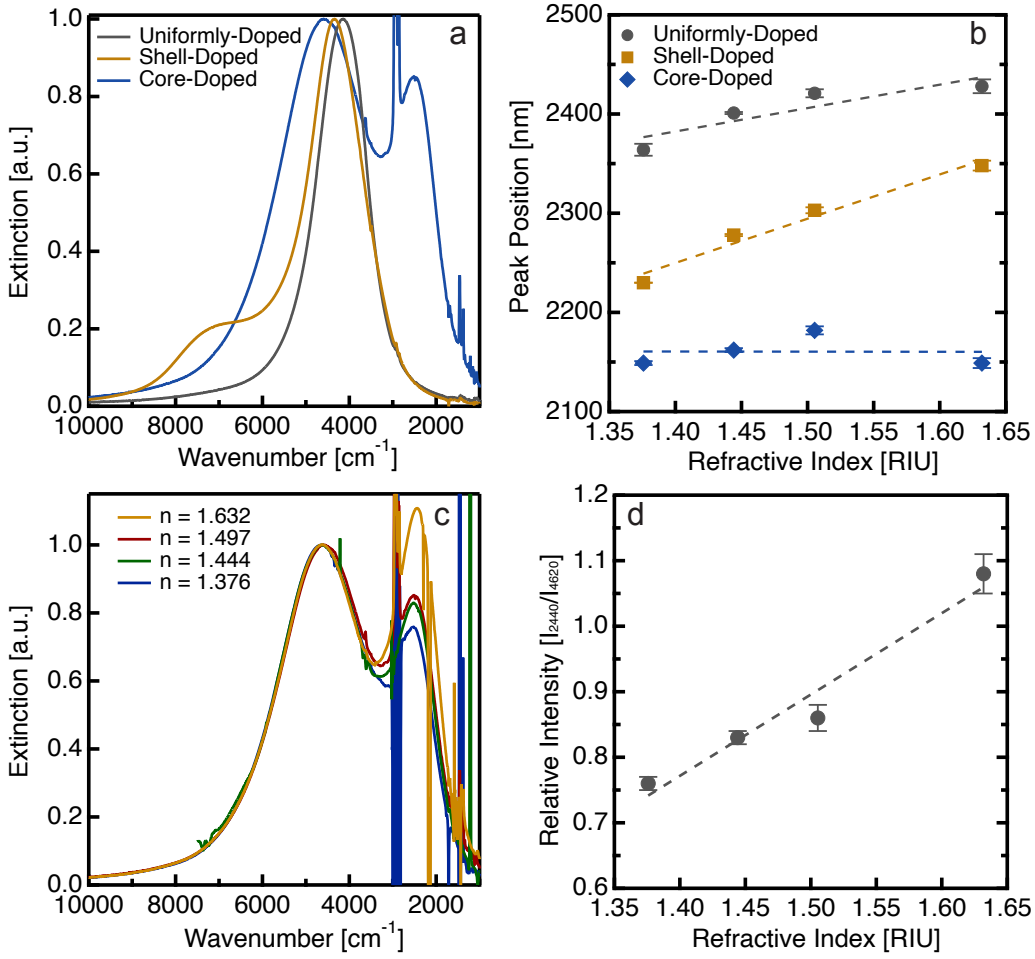

Figure 4.8: Dielectric sensitivity of dopant segregated NCs. (a) Normalized spectra for uniformly doped, shell-doped, and core-doped ITO NCs of similar ω_{LSPR} dispersed in TCE (b) Primary peak positions measured when each sample was dispersed in solvents of differing refractive index. (c) Core-doped spectra, normalized to the high energy mode, for NCs dispersed in all four solvents. (d) Relative intensity of the low energy mode with respect to the high energy mode as a function of refractive index for the core-doped sample shown in panel c. Error bars represent the standard deviation in peak position for three independently prepared dispersions of varying NC concentration. Dashed lines show linear fits.

Table 4.3: A comparison of the dielectric sensitivity of nanocrystals with differing dopant segregation.

Doping Profile	Core Diameter ± 1σ [nm]	Overall Diameter ± 1σ [nm]	at% Sn by ICP-OES ± 1σ	at% Sn by XPS	S ± S.E. [nm/RIU]	
					Exp.	Sim.
Core-Doped	18.9 ± 1.7	30.2 ± 1.6	1.11 + 0.09	~0	-2 ± 101	155 ± 14
Uniformly Doped	n/a	19.4 ± 1.5	3.22 + 0.05	4.5	236 ± 84	734 ± 15
Shell-Doped	13.7 ± 0.9	23.4 ± 2.4	4.03 + 0.05	6.4	446 ± 56	784 ± 24

*S.E. denotes the standard error in the slope of the linear regression

We also fit the spectra for the core- and shell-doped samples dispersed in TCE. Using these extracted parameters, we simulated how the spectra are expected to shift in these different solvents (Appendix C, Figure C5). The simulated sensitivity values show the same trend as the experimental values, however they are higher in all cases. This quantitative disagreement is likely due to the insulating effects of ligands[72] and the convoluting effects of ensemble heterogeneity,[85] neither of which is accounted for in the simulation.

From these results it can be inferred that at a given ω_{LSPR}, shell-doped nanocrystals have the highest near-field enhancement at the surface and are best suited for coupling to vibrational or electronic transitions in nearby molecules or particles. When comparing peak sensitivity of the shell-doped and uniformly doped NCs to other plasmonic materials, we find it falls within the range observed for metallic nanoparticle ensemble measurements, which have ranged from 90 to 801 nm/RIU.[30,128] For these metals, ω_{LSPR} ranges from the visible to the near-infrared, with the lowest energy being 5570 cm^{-1}. Whereas in this work, using only ITO and maintaining spherical NCs under 30 nm in diameter, we've shown tunability in peak position from 6000 cm^{-1} to 1000 cm^{-1}, emphasizing the utility of doped metal oxide NCs in the near to mid-infrared.

The sensitivity of the secondary (lower intensity) modes of the core- and shell-doped samples also matches the expectation based on enhanced electric field distribution in metallic core@shell particles. The higher energy mode in the shell-doped sample does not change significantly with surrounding refractive index, while the lower energy mode in the core-doped sample appreciably changes intensity in comparison to the primary mode (Figure 4.8c). Modulation in relative peak intensity is useful for ratiometric sensing, wherein the relative peak intensities at two wavelengths are compared to monitor the surroundings. These sensors can be advantageous over single-mode sensors because they are internally referenced and thus less susceptible to noise from the environment.[129–131] Their sensitivity can be quantified by measuring the ratio of peak intensities vs refractive index (Figure 4.8d). In this case, our simulation again matched the trends in the experimental spectra, however the sensitivity for our experiment (1.2) *exceeded* that of the simulation (0.35). We hypothesize the quantitative disagreement results from an increase in shell n_e with rising dielectric of the solvent. Prior work reported that increasing the dielectric constant of the surroundings can lower the ionization energy of defects, increasing n_e.[132]

4.2.6 Conclusion

Engineering dopant distribution within doped metal oxide NCs changes the intra-NC charge carrier profile and the corresponding optical response. Varying the thickness of epitaxially grown shells, we observed the evolution of dual-mode infrared extinction due to intra-NC dopant segregation. After fitting spectra with a MG-EMA core@shell model, the extracted n_e profile informed us that dopant activation and carrier diffusion, two factors unique to doped semiconductor NCs, explain the deviation in trends from metallic core@shell particles. Moreover, the dual-mode response resulting from dopant-segregation

enhanced sensitivity to the surroundings in comparison to the single mode response from uniform doping.

But more than simply changing the spectral lineshape, segregation of dopants creates NCs that are optically and electronically inhomogeneous on an ultrafine length scale – all within a single crystal. The optical and electronic inhomogeneity investigated here must be considered in doped semiconductor NC analysis to accurately interpret their measured properties and to fully maximize their potential. For example, the ability to establish an intra-NC dielectric gradient even at relatively low doping levels makes intra-NC dopant placement an enticing opportunity for deeply subwavelength confinement, an exciting prospect for infrared waveguiding.[133,134] Segregating charge carriers to the surface creates an infrared plasmonic nanoantenna with strong near-field enhancement, an ideal candidate for SEIRS. This could also prove useful for plasmon-enhanced photocatalysis[105,135–138] wherein photon absorption promotes an energetic distribution of hot charge carriers that can be transferred to catalyze reactions. These hot carriers typically equilibrate with the lattice on picosecond time scales,[53,139] so surface segregation will reduce the carrier diffusion length to the catalytic surface.

Chapter 5: Looking Ahead for Nonuniform Carrier Concentration in Nanomaterials

Much of the colloidal NC community thinks of semiconductor NCs as exhibiting properties derived from either the *bulk* or from the *surface*. Broadly speaking, a bulk material property should remain constant with changes in size and a surface-related property should change with size – as particle size increases, the ratio of surface area to volume decreases and the overall contribution of the surface effects diminishes. Take the quintessential quantum dot band gap absorption as an example. The bulk material property, the band gap, changes when the system becomes small enough to be quantum confined. In this scenario, the quantum dot radius is smaller than the exciton Bohr radius and thus the surface confines the exciton and raises its energy. Further, the efficiency of this absorption is hindered by surface defect "trap" states. As the size of a quantum dot increases, the band gap shifts to lower energy and the effect of surface trap states diminishes up to a certain point wherein the bulk (size/surface-independent) band gap absorption is reached. My work shows that for doped semiconductor plasmonics, we must add another layer to this picture – the transition from surface to bulk. It is difficult to believe that for materials of order 5 to 10 nm in radius, there is any type of significant "transition" region within it, but my work proves just that. The electronic structure contrast and resulting dielectric contrast that results simply from rearranging dopant atoms within ITO NCs causes a stark change in optoelectronic properties. I hope that this new understanding of the effect of defect distribution within semiconductor NCs can (1) shed light on previously misunderstood results and (2) open the door to new applications.

One recent example that might benefit from investigating intra-NC defect distribution is that of dual mode plasmonic CdO NCs resulting from oxygen vacancy defects (Figure 5.1).[116] While Sn defects are placed deliberately in ITO, for a self-doped

material, such metal oxides with oxygen vacancies or copper chalcogenides with cation vacancies, a nonuniform spatial distribution of defects would likely produce a nonuniform charge carrier profile and altered optical and electronic behavior. I suspect that the appearance of anomalous secondary modes and asymmetric lineshapes in recent literature may be due to unrecognized intra-NC defect segregation.[63,66,116]

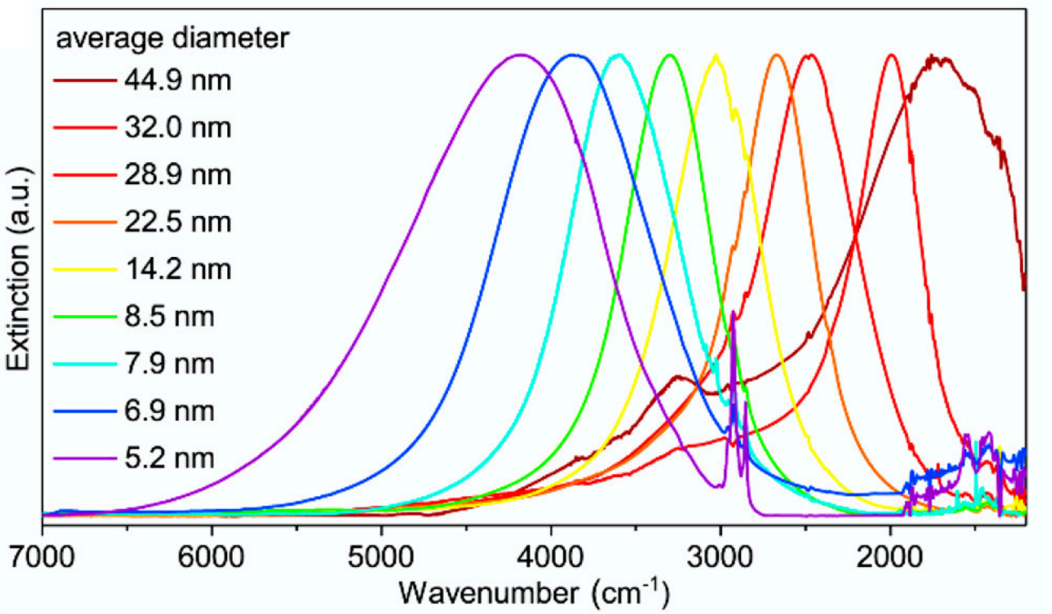

Figure 5.1: Normalized extinction spectra for dispersions of CdO NCs of increasing size. An unexplained secondary mode appears at larger sizes even though the particles remain spherical. Adapted from Ref 116. Copyright 2020 American Chemical Society.

As for new applications, engineering nonuniform intra-NC doping profiles can open the door to novel spectral signatures from dynamic electrochemical plasmonic modulation. Capacitive charging and discharging of doped metal oxides has made them valuable materials for electrochromic window coatings, but the capacitive nature makes it such that the carrier profile can only be changed from the surface. Radial control over doping now gives us the ability to change the carrier profile from the inside out (Figure 5.2). Together with electrochemical modulation of surface potential, altering the intra-NC

doping profiles will enable dynamic plasmonic modulation across near and mid-infrared that has been unachievable up to this point.

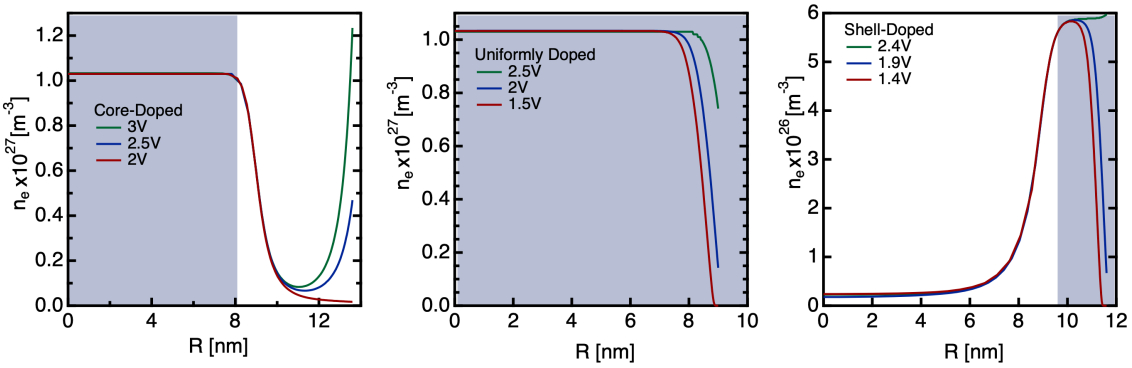

Figure 5.2: COMSOL Multiphysics® simulated carrier concentration profiles for ITO NCs of different radial doping distribution. The shaded region indicates a region doped with 4.5 at% Sn. Each NC is subjected to three different applied surface potentials to simulate the effect of capacitive charging. Simulations courtesy of Christopher Dean.

Even with these recent strides in understanding nonuniform doping profiles, there is still much left to be explored. Of note, most of our knowledge comes from a single material system – ITO. While we expect most doped metal oxides to behave similarly, it is almost certain that there will be certain target advantages for moving to another crystal system such as In:CdO or Al:ZnO. The potential for improved optoelectronic performance merits the continued exploration of dopant-segregated semiconductor NCs.

Appendices

APPENDIX A: SUPPORTING INFORMATION TO CHAPTER 2‡‡

Text A1: Synthesis of ITO NCs

ITO NCs were synthesized by modification of methods published by the Hutchison group.[62,63] NC cores were synthesized by adding 4.7 mmol of metal precursor (In(III)acetate and Sn(IV)acetate) to 10 mL of oleic acid in a round bottom flask. This will be referred to as the precursor flask. The precursor flask is then put under vacuum and heated to 110°C for 1 hour with one nitrogen purge midway through the hour. The precursor flask is then put under nitrogen and heated to 150°C for 2 hours to generate In- and Sn-oleate. Concurrently, 12 mL of oleyl alcohol is put in a second round bottom flask, called the reaction flask. The reaction flask is put under vacuum and heated to 150°C for 2 hours with one nitrogen purge midway through. The reaction flask is then heated to 290°C under nitrogen. Once the In- and Sn-oleate reaction has finished, the contents of the precursor flask are pulled into a syringe for slow injection into the reaction flask. The injection rate is set to 0.2 mL/min and the injection volume depends on the desired NC size. Following the injection, the reaction flask is allowed to stay at 290°C for 20 min before being cooled to room temperature. NCs are purified by 5 cycles of flocculating NCs with ethanol, centrifuging at 7500 RPM, and redispersing in hexane. Overall NC size and size polydispersity were measured by small-angle x-ray scattering (SAXS) and verified by scanning transmission electron microscopy (STEM) image analysis. Overall dopant incorporation was quantified by elemental analysis using inductively coupled plasma-atomic emission spectroscopy (ICP-AES).

‡‡This section contains text and figures adapted from Ref 23, which was written by Corey M. Staller and Stephen L. Gibbs as lead authors in collaboration with Camila A. Saez Cabezas and Delia J. Milliron. It has been adapted with permission from the authors. Copyright 2019 American Chemical Society

Text A2: Spectroscopy measurements

Stock NC dispersions for optical measurements were prepared in a solution of 1.8 mM oleic acid in tetrachloroethylene (TCE). Dilute dispersions in 1.8 mM oleic acid in TCE were prepared from stock solutions immediately before optical measurement and dilution factors were calculated using mass fractions of stock to total solution for each sample. Optical measurements were taken on dilute dispersions in a 0.5 mm pathlength liquid cell. Infrared (650-4000 cm^{-1}) and UV-visible-near infrared (3031-37000 cm^{-1}) extinction were measured using a Bruker Vertex 70 FTIR spectrophotometer and Agilent Cary series UV-vis-NIR spectrophotometer, respectively. All spectra were taken in transmission mode and are reported as extinction. Spectra were backgrounded to a clean solution of 1.8 mM oleic acid in tetrachloroethylene (TCE) before each dilution series. The liquid cell was washed through with 1.8 mM oleic acid in TCE after each dilution series followed by the collection of an after spectrum to confirm the lack of NC deposition. All series reported in this work showed no evidence of deposition on the windows of the cell. NC volume fraction was determined using ICP-AES measurements of stock solutions

Text A3: Small-angle X-ray scattering measurements (SAXS)

SAXS measurements were performed in transmission configuration on a SAXSLAB Ganesha instrument using Cu K_{α} radiation. The sample-detector distance was 1 m and 0.475 m for the NC doping series and NC size series, respectively. ITO NCs were dispersed in a 1:10 volume ratio of TCE:hexane and enclosed in glass capillaries (Charles-Supper Company, Boron Rich, 1.5 mm diameter, 0.01 mm wall thickness) sealed with epoxy. A capillary containing neat 1:10 volume ratio of TCE:hexane was used for background subtraction. Scattering patterns were calibrated using a silver behenate standard[140] and were converted into 1D data by circular averaging using the Igor Pro-based

Nika software for two-dimensional data reduction.[141] The Irena tool suite for modeling and analysis in Igor Pro was used for background subtraction[142] and for fitting the NC form factor following a procedure described in a previous publication.[143]

Text A4: Scanning transmission electron microscopy (STEM) measurements

STEM images were taken with a Hitachi S-5500. Samples for STEM measurements were drop cast on copper TEM grids with carbon supports (400 mesh, Ted Pella).

Text A5: Inductively coupled plasma-atomic emission spectroscopy (ICP-AES) measurements

The overall tin dopant concentration and volume fraction of ITO NCs were characterized by ICP-AES on a Varian 720-ES ICP Optical Emission Spectrometer after digesting the NCs with aqua regia. The volume fraction of ITO was calculated from the concentration of In and Sn in the analyte using an assumed stoichiometry of $(In+Sn)_2O_3$ and density of 7140 mg/mL.

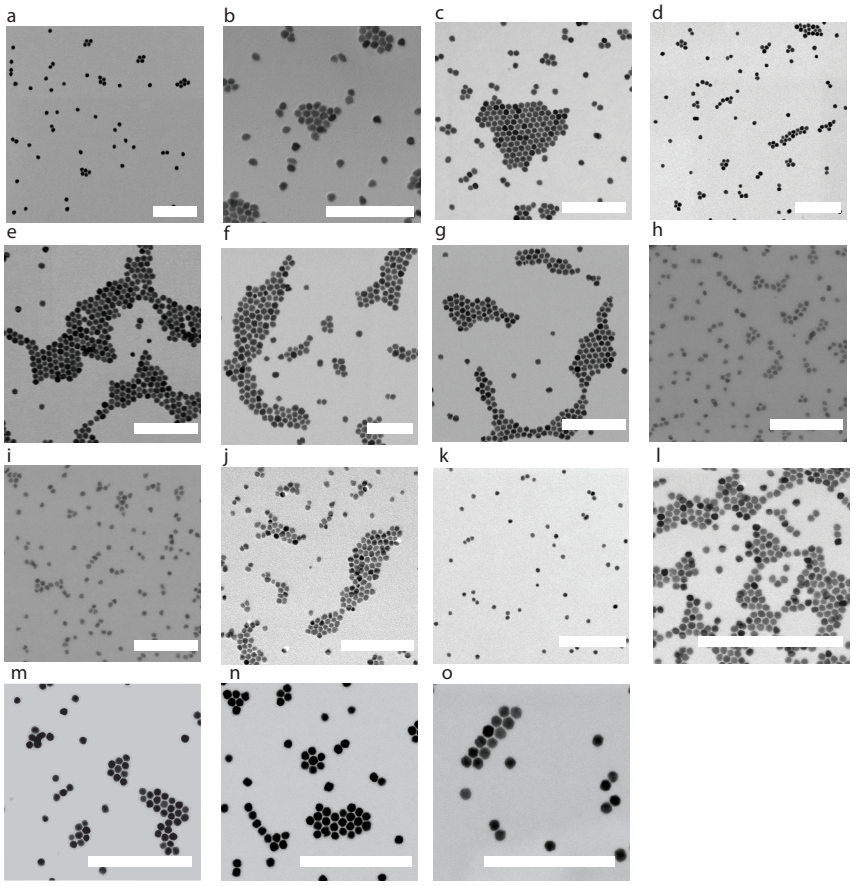

Figure A1: STEM images of 20 nm 0 at% (a), 1 at% (b), 3 at% (c), 4.5 at% (d), 5 at% (e), 6 at% (f), and 7.5 at% (g) ITO NCs and 6 nm (h), 8 nm (i), 11 nm (j), 12 nm (k),14 nm (l), 15 nm (m), 16 nm (n), and 18 nm (o) 5 at% ITO NCs. Scale bars represent 200 nm.

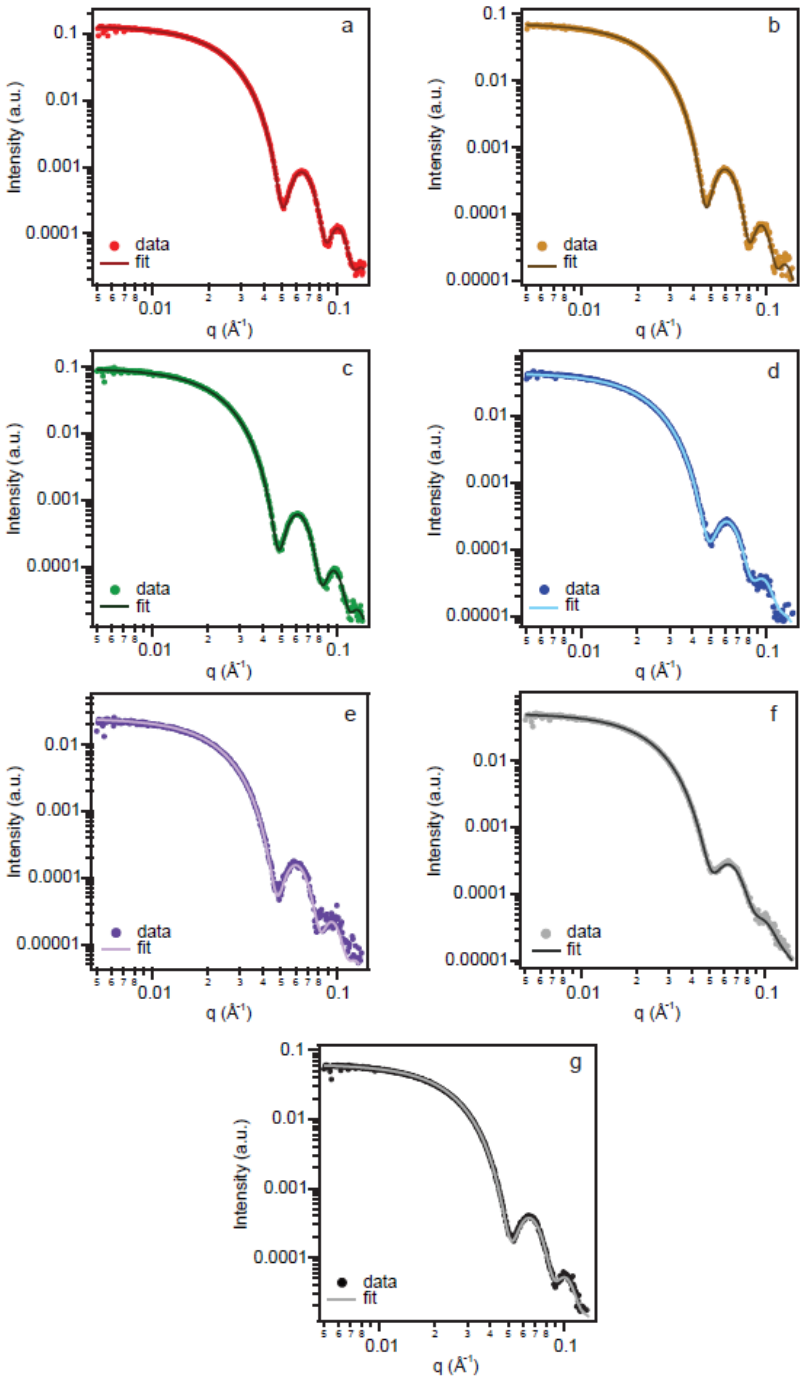

Figure A2: SAXS of 20 nm 0 at% (a), 1 at% (b), 3 at% (c), 4.5 at% (d), 5 at% (e), 6 at% (f), and 7.5 at% (g) ITO NCs.

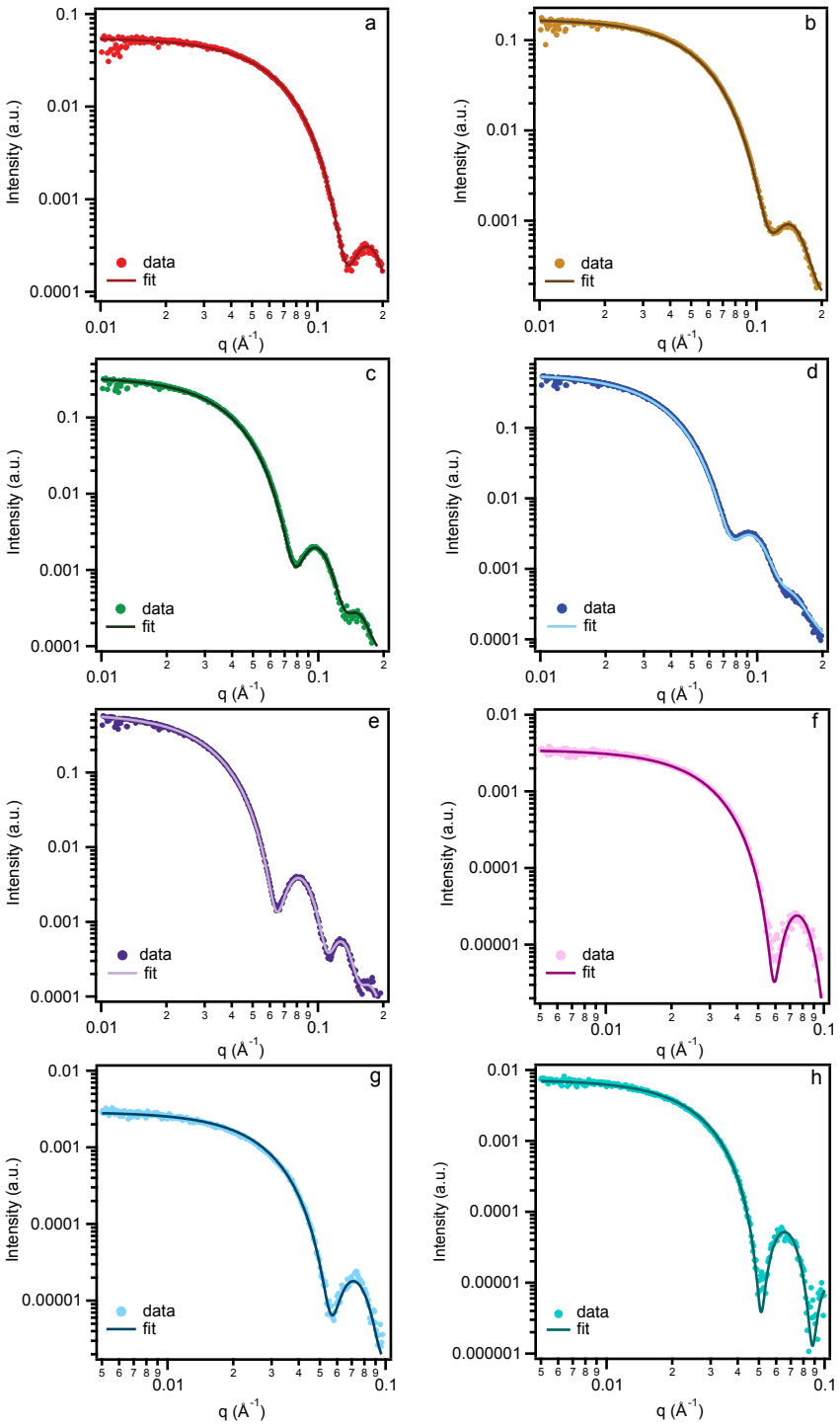

Figure A3: SAXS of 6 nm (a), 8 nm (b), 11 nm (c), 12 nm (d),14 nm (e), 15 nm (f), 16 nm (g), and 18 nm (h) 5 at% ITO NCs.

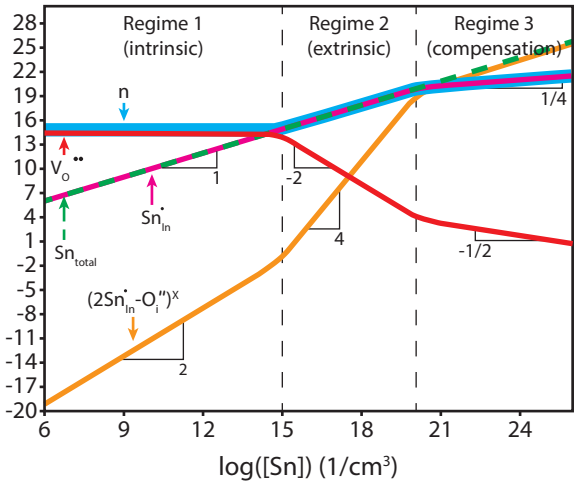

Figure A4: Brouwer Diagram showing the concentration dependence of various defects in ITO with respect to Sn concentration. Adapted from Ref 65 Main Text. Copyright 2014 American Chemical Society.

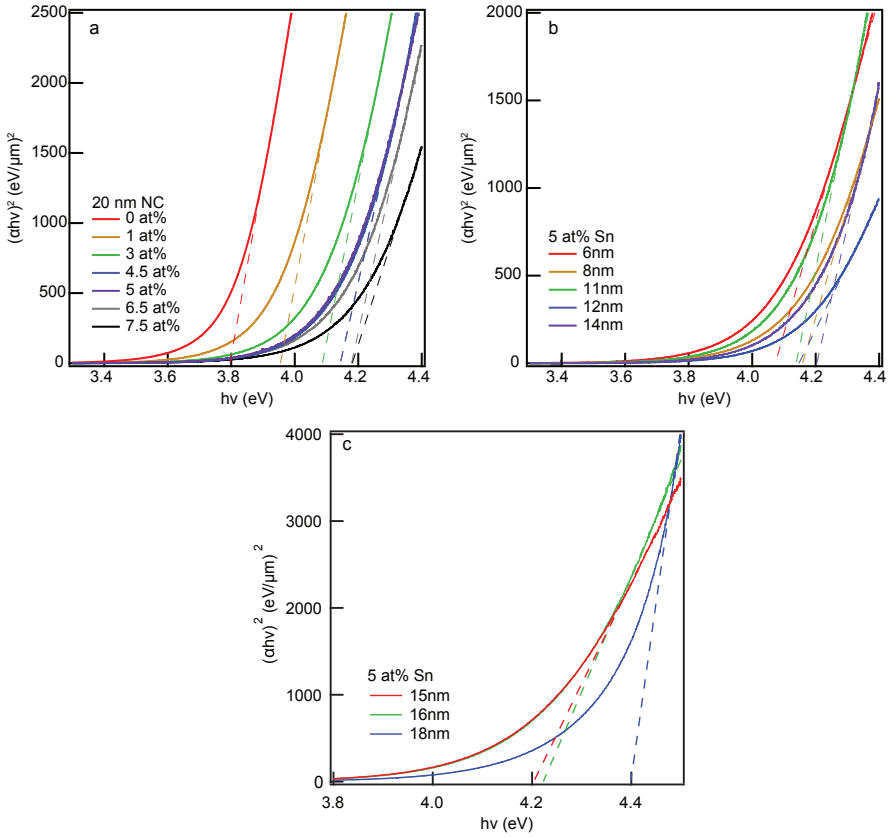

Figure A5: Tauc plots of ITO NCs showing optical bandgap widening with increasing dopant concentration (a) and NC radius (b and c).

Table A1: Comparison of extinction efficiency across materials.

			Extinction coefficient	Extinction cross section		Molar extinction coefficient	Extinction coefficient
	atomic% Sn	r_{NC} (nm)	ϵ (μm^{-1})	um^2	m^2	$M^{-1}cm^{-1}$	$mL\ mg^{-1}cm^{-1}$
ITO NCs	Doping Series						
	0	8.9	4.51	1.3E-05	1.3E-17	7.77E+05	2.74
	1.07	9.6	15.14	5.5E-05	5.5E-17	1.45E+08	9.21
	2.96	9.3	29.12	9.8E-05	9.8E-17	2.57E+08	17.71
	4.45	9.2	51.02	1.7E-04	1.7E-16	4.39E+08	31.03
	*4.97	9.5	51.91	1.8E-04	1.8E-16	4.82E+08	31.57
	6.13	8.8	51.94	1.5E-04	1.5E-16	3.88E+08	31.59
	7.68	8.7	56.55	1.6E-04	1.6E-16	4.10E+08	34.40
	Size Series						
	5.42	3.3	13.58	2.1E-06	2.1E-18	5.38E+06	8.26
	5.54	3.9	24.37	6.2E-06	6.2E-18	1.63E+07	14.82
	5.03	5.8	33.36	2.8E-05	2.8E-17	7.26E+07	20.29
	5.36	6.0	47.45	4.2E-05	4.2E-17	1.10E+08	28.86
	5.03	7.0	47.14	6.8E-05	6.8E-17	1.78E+08	28.68
	4.79	7.7	42.13	8.1E-05	8.1E-17	2.11E+08	25.63
	4.74	8.0	42.67	9.2E-05	9.2E-17	2.39E+08	25.59
	4.61	8.8	43.89	1.3E-04	1.3E-16	3.33E+08	26.70
	*4.97	9.5	51.91	1.8E-04	1.8E-16	4.82E+08	31.57
Au spherical NPs[53]	-	10.0	73.70	3.1E-04	3.1E-16	8.07E+08	16.58
Cu2-xSe NCs[56]	-	17.5	23.50	5.3E-04	5.3E-16	1.38E+09	15.01
PbSe QDs[68]	-	2.75	12.70	1.1E-06	1.1E-18	2.89E+06	6.81
Commercial IR Dye[69]	-	-	-	-	-	9.8E+04	-

*Sample included in both doping and size series

APPENDIX B: SUPPORTING INFORMATION TO CHAPTER 3[§§]

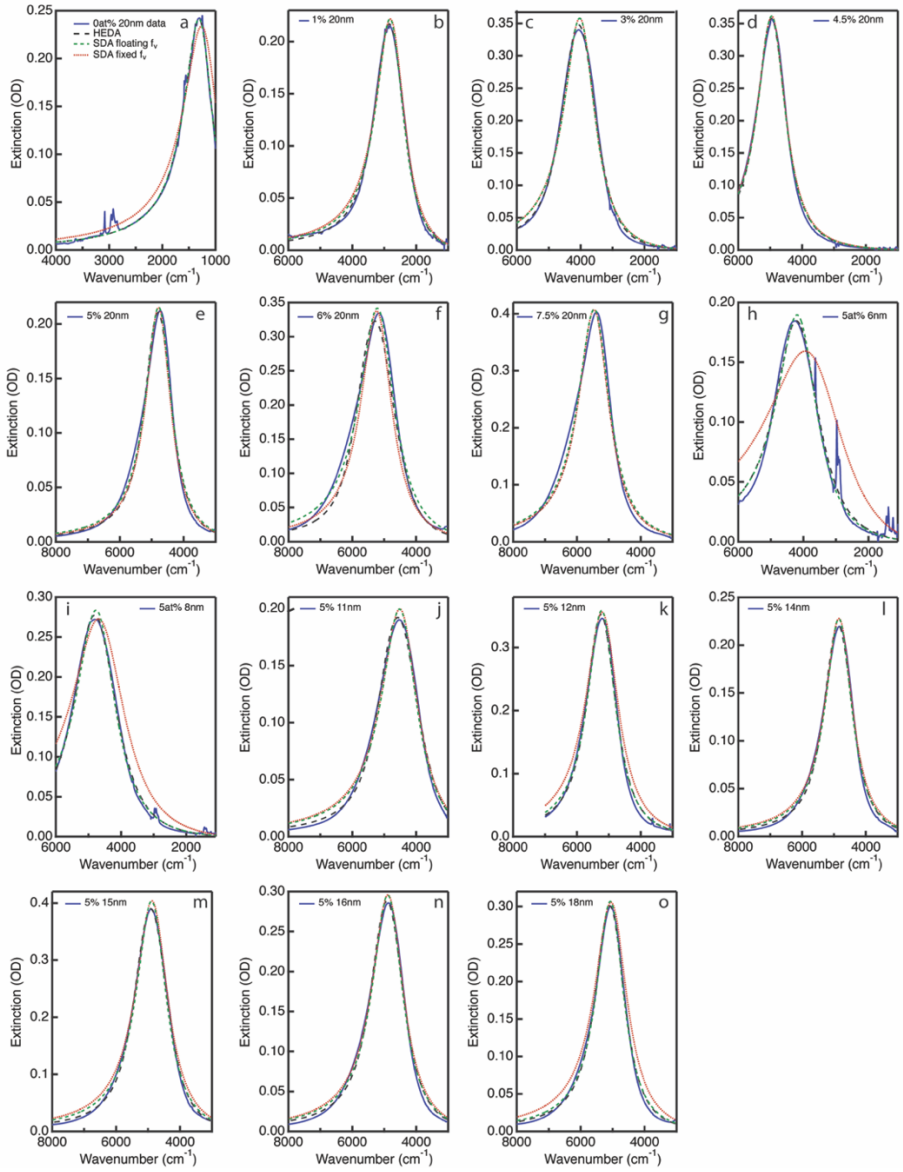

Figure B1: Optical extinction fits for SDA with a floating NC volume fraction, SDA with measured NC volume fraction, and HEDA model for 20 nm 0 at% (a), 1 at% (b), 3 at% (c), 4.5 at% (d), 5 at% (e), 6 at% (f), and 7.5 at% (g) ITO NCs and 6 nm (h), 8 nm (i), 11 nm (j), 12 nm (k),14 nm (l), 15 nm (m), 16 nm (n), and 18 nm (o) 5 at% ITO NCs.

[§§]This section contains text and figures adapted from Ref. 24, which was written by Stephen L. Gibbs and Corey M. Staller as lead authors in collaboration with Ankit Agrawal, Robert W. Johns, Camila A. Saez Cabezas, and Delia J. Milliron. It has been adapted with permission from the authors. Copyright 2020 American Chemical Society

Table B1: Size series fit parameters and calculated properties.

Sample Details	**Nominal Diameter (nm)**	**6**	**8**	**11**	**12**	**14**	**15**	**16**	**18**
	μ_r (nm)	**3.31**	**3.94**	**5.83**	**5.96**	**7.01**	**7.71**	**7.99**	**8.83**
	σ_r (nm)	0.36	0.48	0.76	0.58	0.55	0.39	0.65	0.48
	at% Sn	5.42	5.54	5.03	5.36	5.03	4.79	4.74	4.61
SDA w/ Floating fv	w_p (cm^{-1})	12231	13875	13151	15240	14147	14256	14275	14812
	Γ (cm^{-1})	1561	1488	1360	1080	1027	1160	1169	1057
	n_e (cm^{-3})	6.7E20	8.6E20	7.7E20	1.0E21	8.9E20	9.1E20	9.1E20	9.8E20
SDA w/ Fixed fv	w_p (cm^{-1})	11487	13629	13136	15197	14126	14207	14241	14742
	Γ (cm^{-1})	2962	2071	1389	1254	1091	1275	1261	1274
	n_e (cm^{-3})	5.9E20	8.3E20	7.7E20	1.0E21	8.9E20	9.0E20	9.1E20	9.7E20
HEDA	μ_{ne} (cm^{-3})	7.7E20 ±1.5E18	9.4E20 ±4.6E18	7.7E20 ±1.1E19	1.1E21 ±7.8E18	9.2E20 ±7.4E18	9.4E20 ±3.5E19	9.4E20 ±2.9E19	1.1E21 ±1.1E19
	σ_{ne} (cm^{-3})	7.0E19 ±1.6E18	1.1E20 ±1.0E18	1.3E20 ±2.5E18	7.0E19 ±6.9E18	7.7E19 ±3.8E18	1.1E20 ±1.4E18	8.9E19 ±1.2E18	7.4E19 ±3.5E18
	f_e	0.49 ±0.00	0.65 ±0.03	0.92 ±0.02	0.80 ±0.02	0.88 ±0.03	0.84 ±0.12	0.87 ±0.1	0.75 ±0.03
	l_{bulk}(nm)	17.0	17.0	9.8±0.4	16.0±1.8	12.9±0.8	10.8±0.5	8.7±1	9.9±0.7
	Γ (cm^{-1})	1530±6	1313±12	1021±10	973±28	877±23	914±16	997±6	944±23

Table B2: Dopant concentration series fit parameters and calculated properties.

Sample Details	**at% Sn**	**0**	**1.07**	**2.97**	**4.45**	**4.97**	**6.13**	**7.68**
	μ_r (nm)	8.91	9.56	9.31	9.23	9.46	8.80	8.72
	σ_r (nm)	0.65	0.66	0.68	0.88	0.76	1.05	0.792
SDA w/ Floating fv	w_p (cm^{-1})	3805	8208	11750	14458	13959	15213	15928
	Γ (cm^{-1})	669	1081	1198	1076	1005	1361	1232
	n_e (cm^{-3})	6.5E19	3.0E20	6.2E20	9.3E20	8.7E20	1.0E21	1.1E21
SDA w/ Fixed fv	w_p (cm^{-1})	3640	8172	11750	14454	13965	15276	15942
	Γ (cm^{-1})	821	1139	1200	1090	979	1177	1176
	n_e (cm^{-3})	5.9E19	3.0E20	6.2E20	9.3E20	8.7E20	1.0E21	1.1E21
HEDA	μ_{ne} (cm^{-3})	7.1E19 ±1.0E18	3.1E20 ±1.1E18	6.2E20 ±3.2E18	9.4E20 ±4.1E18	8.7E20 ±1.7E18	1.0E21 ±2.8E18	1.1E21 ±3.1E18
	σ_{ne} (cm^{-3})	1.2E18 ±2.2E18	4.3E19 ±3.5E18	9.4E19 ±1.8E18	4.6E19 ±3.0E18	4.9E19 ±1.1E19	1.5E20 ±7.9E18	9.0E19 ±2.7E18
	f_e	0.70 ±0.03	0.90 ±0.00	0.93 ±0.00	0.96 ±0.02	1.00 ±0.00	1.00 ±0.00	1.00 ±0.00
	l_{bulk}	4.1±0.0	4.7±0.2	7.1±0.2	7.4±0.1	8.1±0.6	11.5±1.5	7.8±0.1
	Γ (cm^{-1})	665±6	940±33	904±18	1016±13	921±44	828±54	1058±11

μ_r and σ_r are the mean NC radius and its standard deviation, ω_p is the plasma frequency, Γ is the damping frequency, n_e is the free electron concentration, μ_{ne} and σ_{ne} are the mean electron concentration and its standard deviation, f_e is the fraction of electron accessible volume, and l_{bulk} is the bulk mean free path.

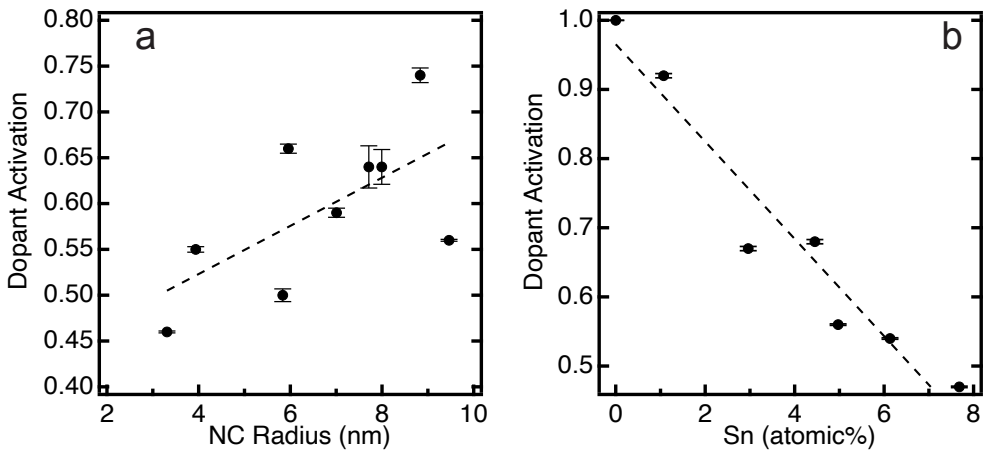

Figure B2: Dopant activation. After quantifying Sn atoms per NC from by ICP-AES, the fraction of Sn dopants that contribute a free electron to the conduction band was plotted versus the NC radius (a) and Sn doping level (b).

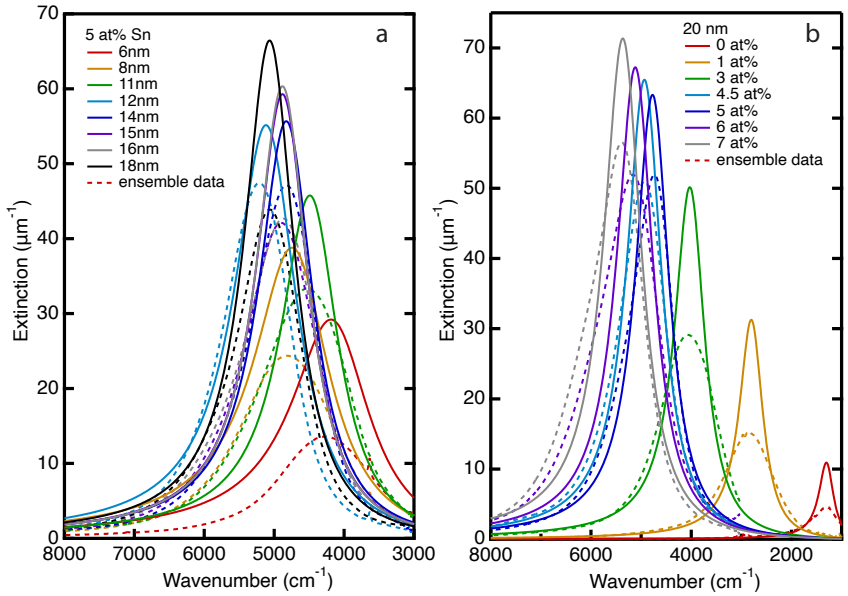

Figure B3: SDA volume-normalized extinction compared to the ensemble spectrum. Calculated extinction based of SDA fit results (solid) is significantly higher than that of the measured ensemble extinction (dashed) for samples in the size series (a) and the doping series (b).

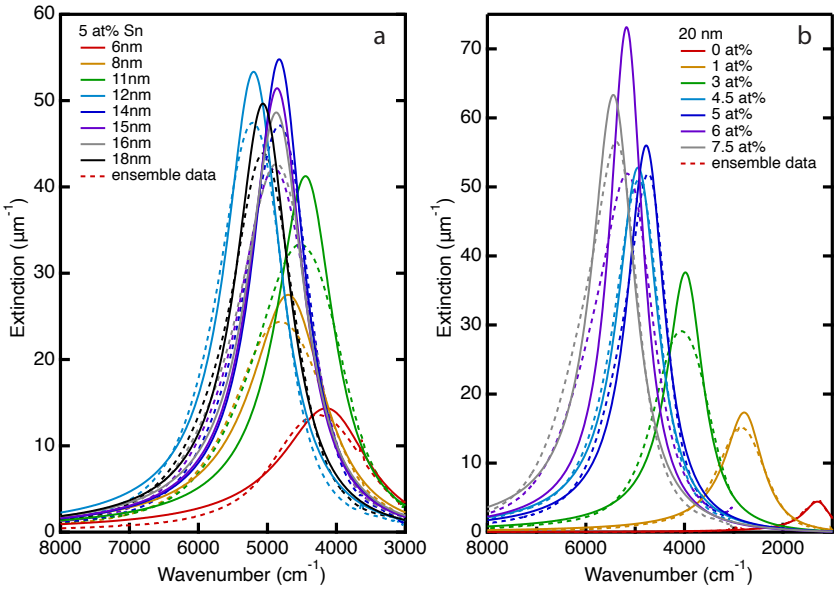

Figure B4: HEDA-derived average NC extinction spectra compared to ensemble. Average NC extinction coefficient (solid) is higher and shows a narrower lineshape than ensemble absorption coefficient (dashed) for samples in both the size series (a) and the doping series (b).

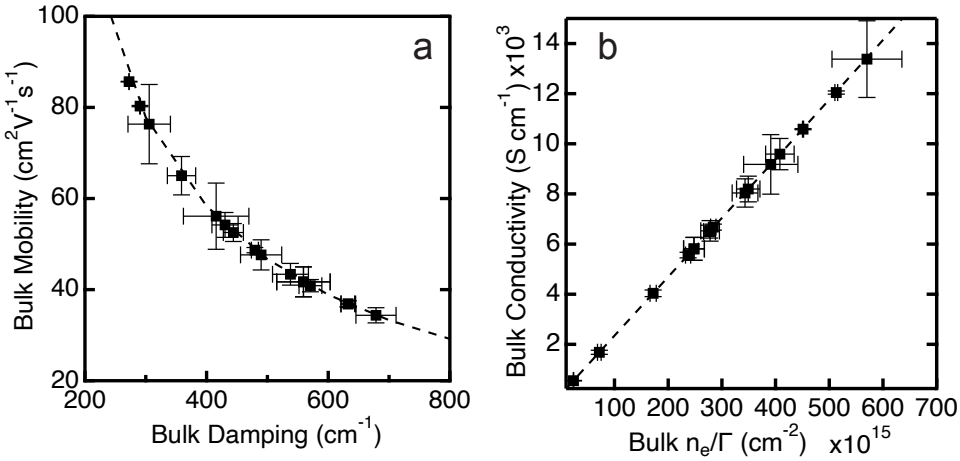

Figure B5: Bulk ITO electronic properties. After removing the effects of surface scattering, the bulk mobility (a) and bulk conductivity (b) are calculated from values extracted from the HEDA model for all ITO samples in this work. Dashed lines calculate the electronic parameters extrapolated beyond values extracted from our sample sets. Error bars indicate standard deviation in the results from HEDA fitting for four independently prepared dispersions of each sample.

APPENDIX C: SUPPORTING INFORMATION TO CHAPTER 4[***]

Text C1: Nanocrystal Synthesis

The slow-injection synthetic approach pioneered by the Hutchison group has served as a powerful platform for studying doping and size effects on the plasmonic response of tin-doped indium oxide (ITO) nanocrystals (NCs).[61–63] For this work, we leveraged this synthetic technique to make two batches of NCs, one with tin dopants segregated to near the surface (shell-doped) and one with tin dopants segregated to the core (core-doped). Briefly, a metal-oleate precursor is slowly injected into a hot bath of oleyl alcohol. After nucleation, the continuous injection drives growth of the NCs without forming new nuclei, producing narrow size distributions. By temporally varying the ratio of Sn to In in the metal oleate precursor, we can control the intra-NC dopant profile. In the shell-doped series, the undoped cores were removed from the reaction mixture to wash away any unreacted precursor. Then the cores were reintroduced in fresh oleyl alcohol and a metal oleate precursor containing 5 at% Sn oleate was slowly injected to grow the doped shell. In the core-doped series, the doped cores were similarly removed and washed before slow injection of purely indium oleate precursor to grow the undoped shell. A more detailed description of the synthetic conditions is reported tin Text A1.

In both syntheses, aliquots were taken during shell growth and quenched in hexane. The aliquots were washed by flocculating with ethanol as an antisolvent, spinning in a centrifuge at 9000 rpm, and redispersing in hexane three times. After a fourth and final precipitation, the NCs were redispersed in the infrared transparent solvent TCE. This

***This section contains text and figures adapted from Ref. 25, which was written by Stephen L. Gibbs as lead author in collaboration with Christopher Dean, Joey Saad, Bharat Tandon, Corey M. Staller, Ankit Agrawal, and Delia J. Milliron. It has been adapted with permission from the authors.

dispersion served as the stock solution from which all subsequent characterization was conducted.

Text C2: Inductively Coupled Plasma-Atomic Emission Spectroscopy (ICP-AES)

A known mass of stock solution was dried in a test tube for each sample. That dried pellet was digested with aqua regia for 2 days and then diluted to 2% acid with Milli-Q water. By calibrating to standards prepared from Sigma Aldrich (TraceCERT® 1000mg In/L nitric acid and 1000mg Sn/L nitric acid), the concentration of In and Sn ions was quantified in a Varian 720-ES ICP-OES. This data was used to calculate the overall doping percentage of each sample. As well, after assuming a density of 7.14 g/mL for indium oxide, we calculated the volume fraction of NCs in the TCE stock solution. This volume fraction was used for calculating NC concentration for dispersions measured by spectroscopy and was incorporated into fitting.

Text C3: X-ray Photoelectron Spectroscopy (XPS)

50 mL of stock solution was dropcast onto a silicon substrate and dried on a hot plate at moderate temperature to evaporate the solvent. The samples were analyzed in a Kratos x-ray photoelectron spectrometer (axis ultra DLD) using an Al K_α x-ray source. Peaks were calibrated to the carbon 1s peak at 284.8 eV binding energy. Near-surface Sn was calculated by fitting the Sn 3d and In 3d peaks in CasaXPS (http://www.casaxps.com/) and taking the ratio of the area of the Sn 3d peaks to that of the Sn 3d and In 3d combined, factoring in the sensitivity factors for each.

Text C4: Visible and Infrared Spectroscopy

Three dispersions of different NC concentration for each sample were made by diluting from the TCE stock solution. These dispersions were loaded in a liquid cell that

consisted of two KBr plates separated by a 0.5 mm Teflon spacer. To collect spectra at lower energies, the liquid cell was loaded in a Bruker Vertex 70 Fourier Transform Infrared (FT-IR) spectrophotometer (350-6500 cm^{-1}) in transmission mode. To collect at higher energy, the cell was also loaded into an Agilent Cary series ultraviolet-visible-near infrared (UV-Vis-NIR) spectrophotometer (3032-10000 cm^{-1}) in transmission mode. In some cases, data was stitched together to plot a spectrum ranging from mid-IR to near-IR.

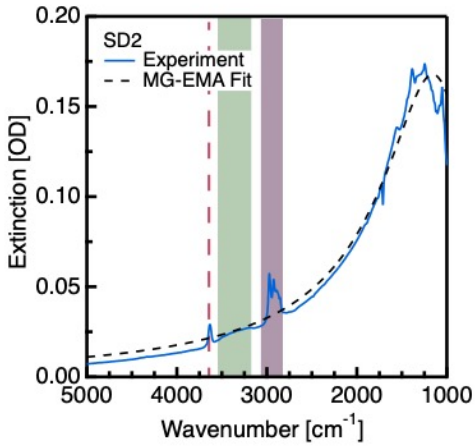

Figure C1: Assigning molecular vibrational modes. The dashed line at 3630 cm^{-1} marks O-H stretching from free alcohol groups.[144] The broad peak ranging from 3500-3200 cm^{-1} (green bar) marks a range of stretches for physisorbed water/hydroxyls that are known to adsorb to metal oxide surfaces.[21] The peaks ranging from 3030-2800 cm^{-1} (purple bar) mark C-H stretching bands from oleic acid ligands.[144]

Text C5: Effective Medium Theory

For impingent broadband light, the optical response of any material is modeled using a frequency- dependent dielectric function $\varepsilon(\omega)$. For metals, the dielectric response is dominated by the polarizability of free electrons in response to incident photons, which takes the following form:

$$\varepsilon(\omega) = \varepsilon_\infty - \frac{\omega_p^2}{\omega^2 + i\omega\Gamma} \qquad \text{Equation C1}$$

Here, ε_∞ is the high frequency dielectric constant, ω_p is the plasma frequency, and Γ is the frequency of electron scattering events. The plasma frequency is dependent on the electron concentration n_e in the following way:

$$\omega_p = \sqrt{\frac{e^2 n_e}{\varepsilon_0 m_e^*}} \qquad \text{Equation C2}$$

Where e is the charge of an electron, ε_0 is the permittivity of free space, and m_e^* is the effective mass of an electron. The dielectric response heavily depends on the concentration of free electrons. So, for a NC with a nonuniform n_e profile, the dielectric function itself becomes nonuniform. The polarizability of a spherical particle with a core and shell having different dielectric properties can be well-approximated using an electromagnetic mixing formula known as the Maxwell-Garnett effective medium approximation (MG-EMA). Therein, the core and shell can be combined into a single dielectric function. Note that this effective dielectric function (ε_{eff}) no longer follows the Drude form of Equation C1, but is instead:

$$\varepsilon_{eff}(\omega) = \varepsilon_{shell}\left(\frac{(\varepsilon_{core} + 2\varepsilon_{shell}) + 2F_{v,core}(\varepsilon_{core} - \varepsilon_{shell})}{(\varepsilon_{core} + 2\varepsilon_{shell}) - F_{v,core}(\varepsilon_{core} - \varepsilon_{shell})}\right) \qquad \text{Equation C3}$$

Where $F_{v,core}$ is the volume of the core normalized by the volume of the entire particle. Lastly, employing Mie scattering theory we can calculate the extinction cross-section using Equation C4.

$$\sigma_{ext}(\omega) = 3Vk\sqrt{\varepsilon_{env}}Imag\left\{\frac{\varepsilon_{eff}(\omega) - \varepsilon_{env}}{\varepsilon_{eff}(\omega) + 2\varepsilon_{env}}\right\} \qquad \text{Equation C4}$$

Here, k is the wavevector and ε_{env} is the dielectric constant of the surroundings.

Table C1: Average and standard deviation of fit results for shell-doped samples for three independently prepared dispersions of varying NC concentration.

Sample	$\omega_{p,core}$ [cm^{-1}]	$\omega_{p,shell}$ [cm^{-1}]	$F_{v,core}$	Γ_{core} [cm^{-1}]	Γ_{shell} [cm^{-1}]
SD1	2372 ± 103	0	1.00	700 ± 19	0
SD2	3353 ± 25	0	1.00	1263 ± 8	0
SD3	6266 ± 28	11886 ± 67	1.00	2228 ± 83	1956 ± 143
SD4	6744 ± 32	12176 ± 33	0.93 ± 0.01	2145 ± 19	1865 ± 17
SD5	7038 ± 77	12566 ± 37	0.88 ± 0.02	2141 ± 55	1912 ± 47
SD6	6304 ± 305	12269 ± 204	0.69 ± 0.07	1389 ± 508	1958 ± 421
SD7	7049 ± 102	12978 ± 20	0.78 ± 0.02	2018 ± 85	1865 ± 58

Table C2: Average and standard deviation of fit results for core-doped samples for three independently prepared dispersions of varying NC concentration.

Sample	$\omega_{p,core}$ [cm^{-1}]	$\omega_{p,shell}$ [cm^{-1}]	$F_{v,core}$	Γ_{core} [cm^{-1}]	Γ_{shell} [cm^{-1}]
CD0	15439 ± 62	1000	0.73 ± 0.03	1117 ± 1	10000
CD1	15506 ± 109	1000	0.67 ± 0.05	1044 ± 6	10000
CD2	14929 ± 29	1000	0.74 ± 0.01	1124 ± 34	10000
CD3	13993 ± 52	1000	0.72 ± 0.02	1441 ± 21	10000
CD4	15024 ± 123	11549 ± 397	0.23 ± 0.08	161 ± 43	2234 ± 176
CD5	14768 ± 54	10082 ± 231	0.28 ± 0.04	658 ± 191	2553 ± 202
CD6	14427 ± 227	9030 ± 350	0.32 ± 0.10	995 ± 328	2266 ± 439
CD7	14610 ± 153	8742 ± 244	0.23 ± 0.04	845 ± 235	2673 ± 320

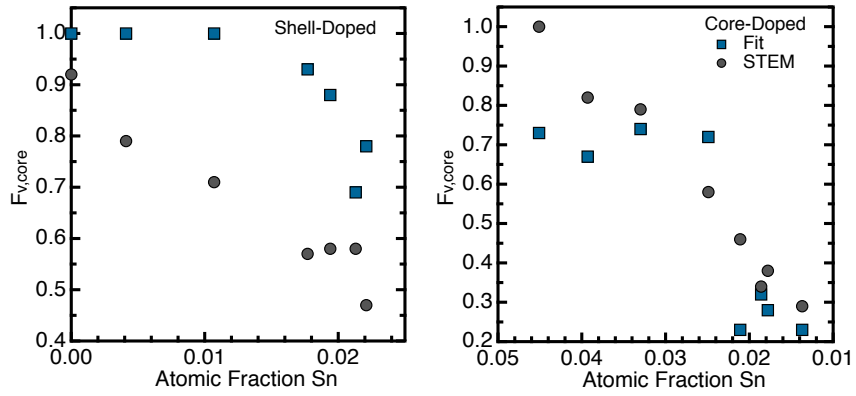

Figure C2: Comparison of calculated values for $F_{v,core}$ based on STEM imaging (gray circles) and based on fitting optical spectra (blue squares).

We do not expect $F_{v,core}$ values from STEM and from spectral fitting to exactly match. The values from STEM represent the fraction of the NC volume that has no dopants (shell-doped) or that has dopants (core-doped). On the other hand, the fitted $F_{v,core}$ reflects the charge carrier profile. Because the model makes the simplifying assumption that there is a stepwise change in carrier concentration, the radius at which the model places the core/shell boundary is somewhat arbitrarily placed in the transition region. While our two-layer model prevents us from drawing a resolved carrier profile from core to surface, the experimental data can still be fit rather well and the results trend with what is expected. First, fitted $F_{v,core}$ values trend downward with shell growth. As well, for the shell-doped NCs, the fitted values consistently fall above the values for $F_{v,core}$ calculated from STEM imaging. This offset is logical considering there is carrier diffusion from the ITO shell to the IO core that will effectively shrink the volume of the high carrier concentration shell. Likewise, the fitted values for the core-doped samples are below the corresponding values from STEM – effectively shrinking the volume of the high carrier concentration core due to carrier diffusion from the ITO core to the IO shell.

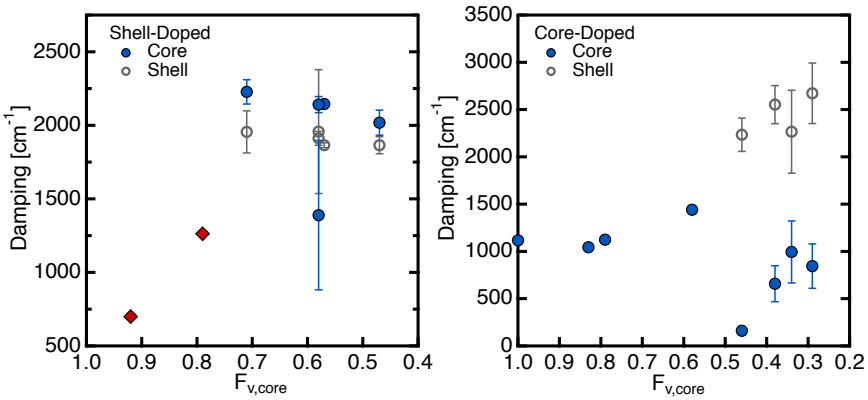

Figure C3: Extracted values for damping in the core and shell for the shell-doped (left) and core-doped (right) series. Red diamonds indicate samples that were fit to a uniform dielectric function – not a core-shell.

The two main contributors to carrier damping within a NC are the bulk scattering, which determines the intrinsic mean free path, and the frequency of surface scattering. Due to the reduced physical dimensions, we expect surface scattering to increase for carriers segregated to a shell, compared to those in the core.[145] For the core-doped series that is indeed the case. However, for the shell-doped series we see the difference in damping between core and shell is not nearly as significant. In fact, the damping of the IO core is greater than that of the ITO shell. This indicates that the mean free path of carriers in ITO is greater than that in indium oxide. While there is no consensus on the trend of mean free path with carrier concentration, this trend has been seen in calculations for ITO films.[89] This insight suggests that Sn^{4+} as an ionized impurity in ITO may not be the dominant contributor to carrier scattering at these concentrations and, further, that increasing dopant incorporation suppresses the concentration of doubly charged oxygen vacancies that are stronger contributors to damping. Reduced damping resulting from elimination of oxygen vacancies in indium oxide has been reported previously.[109,146]

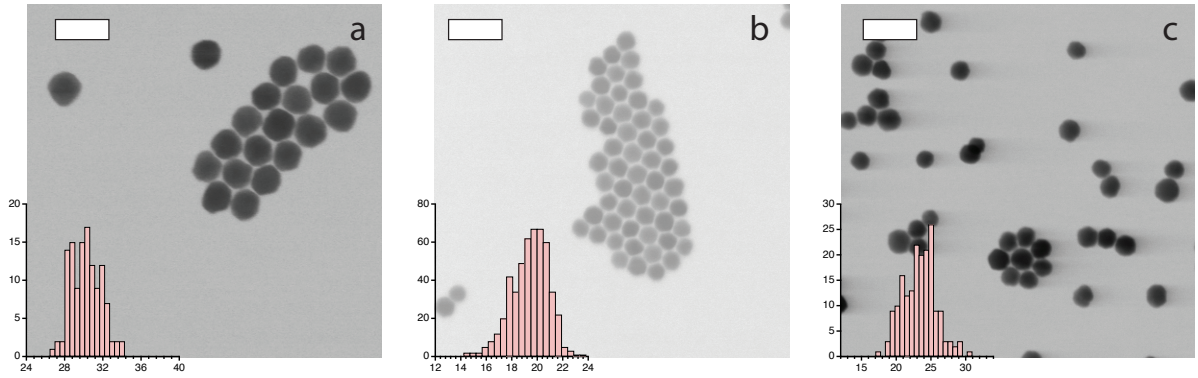

Figure C4: STEM images and size histograms for samples made for dielectric sensitivity measurements for (a) core-doped, (b) uniformly-doped, and (c) shell-doped ITO. Scale bars are 50 nm.

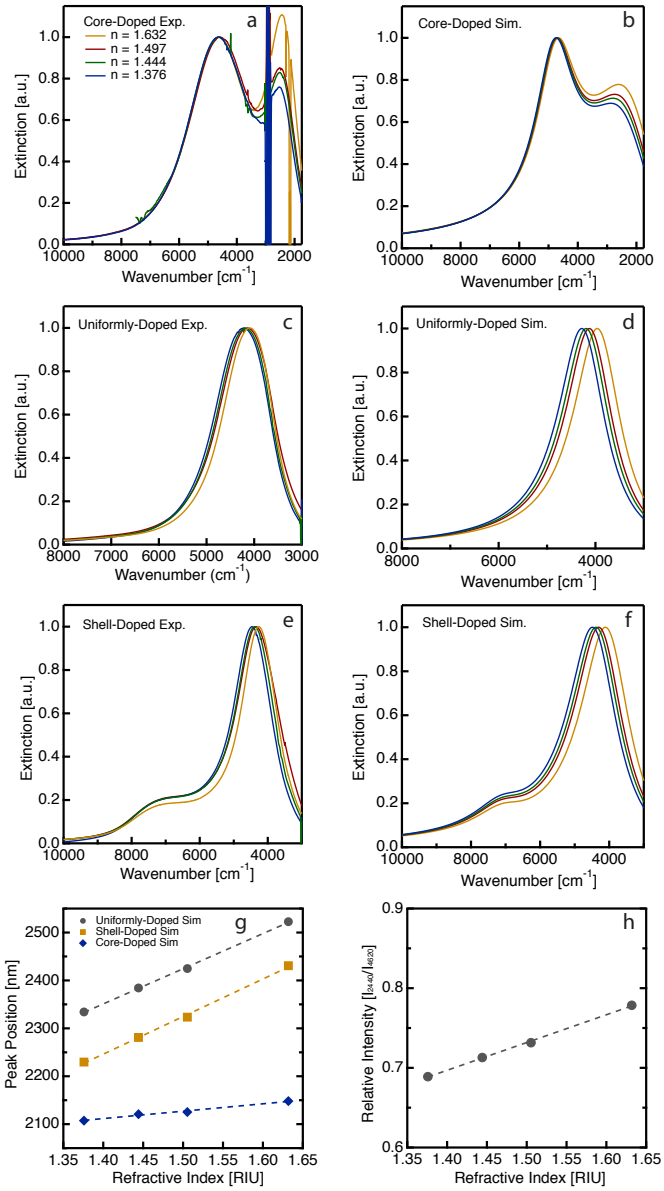

Figure C5: Experimental and simulated graphs for changes to optical response with a changing surrounding refractive index. Plotted above are the spectra from core-doped (a) experiment and (b) simulation, uniformly doped (c) experiment and (d) simulation, and shell-doped (e) experiment and (f) simulation. (g) The slope of the peak wavelength as a function of RIU quantifies the sensitivity for the simulated peak shifts – these results were compared to the experimental peak shifts. (h) Simulated peak intensities for the core-doped sample. The slope of the relative peak intensities vs. RIU can be used as an alternative metric for sensitivity to the surroundings.

Table C3: Average and standard deviation of fit results for three independently prepared dispersions of varying NC concentration for each sample.

Sample	$\omega_{p,core}$ [cm^{-1}]	$\omega_{p,shell}$ [cm^{-1}]	$F_{v,core}$	Γ_{core} [cm^{-1}]	Γ_{shell} [cm^{-1}]
Core-Doped	14078 ± 33	6744 ± 18	0.18 ± 0.01	1174 ± 87	2908 ± 77
Uniformly-Doped	12185 ± 176	1000	0.85 ± 0.13	1204 ± 26	1000
Shell-Doped	10181 ± 260	14918 ± 50	0.47 ± 0.04	1622 ± 96	1810 ± 92

References

(1) Introduction to the Electromagnetic Spectrum | Science Mission Directorate https://science.nasa.gov/ems/01_intro (accessed Apr 23, 2021).

(2) Rastinehad, A. R.; Anastos, H.; Wajswol, E.; Winoker, J. S.; Sfakianos, J. P.; Doppalapudi, S. K.; Carrick, M. R.; Knauer, C. J.; Taouli, B.; Lewis, S. C.; Tewari, A. K.; Schwartz, J. A.; Canfield, S. E.; George, A. K.; West, J. L.; Halas, N. J. Gold Nanoshell-Localized Photothermal Ablation of Prostate Tumors in a Clinical Pilot Device Study. *Proc. Natl. Acad. Sci.* **2019**, *116* (37), 18590–18596. https://doi.org/10.1073/pnas.1906929116.

(3) Shaik, F.; Peer, I.; Jain, P. K.; Amirav, L. Plasmon-Enhanced Multicarrier Photocatalysis. *Nano Lett.* **2018**, *18* (7), 4370–4376. https://doi.org/10.1021/acs.nanolett.8b01392.

(4) Adato, R.; Altug, H. In-Situ Ultra-Sensitive Infrared Absorption Spectroscopy of Biomolecule Interactions in Real Time with Plasmonic Nanoantennas. *Nat. Commun. Lond.* **2013**, *4*, 2154. http://dx.doi.org/10.1038/ncomms3154.

(5) Qian, Z.; Kang, S.; Rajaram, V.; Cassella, C.; McGruer, N. E.; Rinaldi, M. Zero-Power Infrared Digitizers Based on Plasmonically Enhanced Micromechanical Photoswitches. *Nat. Nanotechnol.* **2017**, *12* (10), 969–973. https://doi.org/10.1038/nnano.2017.147.

(6) Capacitance. *Wikipedia*; 2021.

(7) Paul Drude. *Annalen der Physik* **1900**, No. 1, 556–613.

(8) Paul Drude. *Annalen der Physik* **1900**, No. 3, 369–402.

(9) Neil W. Ashcroft; N. David Mermin. *Solid State Physics*; Brooks/Cole, 1976.

(10) Stefan A. Maier. *Plasmonics: Fundamentals and Applications*; Springer Science+Business Media LLC, 2007.

(11) Mie, G. Beiträge Zur Optik Trüber Medien, Speziell Kolloidaler Metallösungen. *Ann. Phys.* **1908**, *330* (3), 377–445. https://doi.org/10.1002/andp.19083300302.

(12) Lycurgus Cup. *Wikipedia*; 2020.

(13) Bohren, C.; Huffman, D. *Absorption and Scattering of Light by Small Particles*; Wiley, 1983.

(14) Brian S. Mitchell. *An Introduction to Materials Engineering and Science For Chemical and Materials Engineers*; John Wiley & Sons, Inc, 2004.

(15) Bergerud, A.; Selbach, S. M.; Milliron, D. J. Oxygen Incorporation and Release in Metastable Bixbyite V2O3 Nanocrystals. *ACS Nano* **2016**, *10* (6), 6147–6155. https://doi.org/10.1021/acsnano.6b02093.

(16) Agrawal, A.; Cho, S. H.; Zandi, O.; Ghosh, S.; Johns, R. W.; Milliron, D. J. Localized Surface Plasmon Resonance in Semiconductor Nanocrystals. *Chem. Rev.* **2018**, *118* (6), 3121–3207. https://doi.org/10.1021/acs.chemrev.7b00613.

(17) Gibbs, S. L.; Staller, C. M.; Milliron, D. J. Surface Depletion Layers in Plasmonic Metal Oxide Nanocrystals. *Acc. Chem. Res.* **2019**, *52* (9), 2516–2524. https://doi.org/10.1021/acs.accounts.9b00287.

(18) Zandi, O.; Agrawal, A.; Shearer, A. B.; Reimnitz, L. C.; Dahlman, C. J.; Staller, C. M.; Milliron, D. J. Impacts of Surface Depletion on the Plasmonic Properties of Doped Semiconductor Nanocrystals. *Nat. Mater.* **2018**, 1. https://doi.org/10.1038/s41563-018-0130-5.

(19) Agrawal, A.; Kriegel, I.; Runnerstrom, E. L.; Scotognella, F.; Llordes, A.; Milliron, D. J. Rationalizing the Impact of Surface Depletion on Electrochemical Modulation of Plasmon Resonance Absorption in Metal Oxide Nanocrystals. *ACS Photonics* **2018**, *5* (5), 2044–2050. https://doi.org/10.1021/acsphotonics.7b01587.
(20) Staller, C. M.; Robinson, Z. L.; Agrawal, A.; Gibbs, S. L.; Greenberg, B. L.; Lounis, S. D.; Kortshagen, U. R.; Milliron, D. J. Tuning Nanocrystal Surface Depletion by Controlling Dopant Distribution as a Route Toward Enhanced Film Conductivity. *Nano Lett.* **2018**, *18* (5), 2870–2878. https://doi.org/10.1021/acs.nanolett.7b05484.
(21) Ephraim, J.; Lanigan, D.; Staller, C.; Milliron, D. J.; Thimsen, E. Transparent Conductive Oxide Nanocrystals Coated with Insulators by Atomic Layer Deposition. *Chem. Mater.* **2016**, *28* (15), 5549–5553. https://doi.org/10.1021/acs.chemmater.6b02414.
(22) Seiwatz, R.; Green, M. Space Charge Calculations for Semiconductors. *J. Appl. Phys.* **1958**, *29* (7), 1034–1040. https://doi.org/10.1063/1.1723358.
(23) Staller, C. M.; Gibbs, S. L.; Saez Cabezas, C. A.; Milliron, D. J. Quantitative Analysis of Extinction Coefficients of Tin-Doped Indium Oxide Nanocrystal Ensembles. *Nano Lett.* **2019**, *19* (11), 8149–8154. https://doi.org/10.1021/acs.nanolett.9b03424.
(24) Gibbs, S. L.; Staller, C. M.; Agrawal, A.; Johns, R. W.; Saez Cabezas, C. A.; Milliron, D. J. Intrinsic Optical and Electronic Properties from Quantitative Analysis of Plasmonic Semiconductor Nanocrystal Ensemble Optical Extinction. *J. Phys. Chem. C* **2020**, *124* (44), 24351–24360. https://doi.org/10.1021/acs.jpcc.0c08195.
(25) Gibbs, S. L.; Dean, C.; Saad, J.; Tandon, B.; Staller, C. M.; Agrawal, A.; Milliron, D. J. Dual-Mode Infrared Absorption by Segregating Dopants within Plasmonic Semiconductor Nanocrystals. *Nano Lett.* **2020**, *20* (10), 7498–7505. https://doi.org/10.1021/acs.nanolett.0c02992.
(26) Garcia, G.; Buonsanti, R.; Runnerstrom, E. L.; Mendelsberg, R. J.; Llordes, A.; Anders, A.; Richardson, T. J.; Milliron, D. J. Dynamically Modulating the Surface Plasmon Resonance of Doped Semiconductor Nanocrystals. *Nano Lett.* **2011**, *11* (10), 4415–4420. https://doi.org/10.1021/nl202597n.
(27) Wang, Y.; Runnerstrom, E. L.; Milliron, D. J. Switchable Materials for Smart Windows. *Annu. Rev. Chem. Biomol. Eng.* **2016**, *7* (1), 283–304. https://doi.org/10.1146/annurev-chembioeng-080615-034647.
(28) Llordés, A.; Garcia, G.; Gazquez, J.; Milliron, D. J. Tunable Near-Infrared and Visible-Light Transmittance in Nanocrystal-in-Glass Composites. *Nature* **2013**, *500* (7462), 323–326. https://doi.org/10.1038/nature12398.
(29) Anker, J. N.; Hall, W. P.; Lyandres, O.; Shah, N. C.; Zhao, J.; Van Duyne, R. P. Biosensing with Plasmonic Nanosensors. In *Nanoscience and Technology*; Co-Published with Macmillan Publishers Ltd, UK, 2009; pp 308–319. https://doi.org/10.1142/9789814287005_0032.
(30) Mayer, K. M.; Hafner, J. H. Localized Surface Plasmon Resonance Sensors. *Chem. Rev.* **2011**, *111* (6), 3828–3857. https://doi.org/10.1021/cr100313v.
(31) Neubrech, F.; Huck, C.; Weber, K.; Pucci, A.; Giessen, H. Surface-Enhanced Infrared Spectroscopy Using Resonant Nanoantennas. *Chem. Rev.* **2017**, *117* (7), 5110–5145. https://doi.org/10.1021/acs.chemrev.6b00743.

(32) Willets, K. A.; Van Duyne, R. P. Localized Surface Plasmon Resonance Spectroscopy and Sensing. *Annu. Rev. Phys. Chem.* **2007**, *58* (1), 267–297. https://doi.org/10.1146/annurev.physchem.58.032806.104607.
(33) Stiles, P. L.; Dieringer, J. A.; Shah, N. C.; Van Duyne, R. P. Surface-Enhanced Raman Spectroscopy. *Annu. Rev. Anal. Chem.* **2008**, *1* (1), 601–626. https://doi.org/10.1146/annurev.anchem.1.031207.112814.
(34) Kneipp, K.; Wang, Y.; Kneipp, H.; Perelman, L. T.; Itzkan, I.; Dasari, R. R.; Feld, M. S. Single Molecule Detection Using Surface-Enhanced Raman Scattering (SERS). *Phys. Rev. Lett.* **1997**, *78* (9), 1667–1670. https://doi.org/10.1103/PhysRevLett.78.1667.
(35) Harris, N.; Ford, M. J.; Cortie, M. B. Optimization of Plasmonic Heating by Gold Nanospheres and Nanoshells. *J. Phys. Chem. B* **2006**, *110* (22), 10701–10707. https://doi.org/10.1021/jp0606208.
(36) Herzog, J. B.; Knight, M. W.; Natelson, D. Thermoplasmonics: Quantifying Plasmonic Heating in Single Nanowires. *Nano Lett.* **2014**, *14* (2), 499–503. https://doi.org/10.1021/nl403510u.
(37) Donner, J. S.; Thompson, S. A.; Alonso-Ortega, C.; Morales, J.; Rico, L. G.; Santos, S. I. C. O.; Quidant, R. Imaging of Plasmonic Heating in a Living Organism. *ACS Nano* **2013**, *7* (10), 8666–8672. https://doi.org/10.1021/nn403659n.
(38) Cole, J. R.; Mirin, N. A.; Knight, M. W.; Goodrich, G. P.; Halas, N. J. Photothermal Efficiencies of Nanoshells and Nanorods for Clinical Therapeutic Applications. *J. Phys. Chem. C* **2009**, *113* (28), 12090–12094. https://doi.org/10.1021/jp9003592.
(39) Hirsch, L. R.; Stafford, R. J.; Bankson, J. A.; Sershen, S. R.; Rivera, B.; Price, R. E.; Hazle, J. D.; Halas, N. J.; West, J. L. Nanoshell-Mediated near-Infrared Thermal Therapy of Tumors under Magnetic Resonance Guidance. *Proc. Natl. Acad. Sci.* **2003**, *100* (23), 13549–13554. https://doi.org/10.1073/pnas.2232479100.
(40) Gobin, A. M.; Lee, M. H.; Halas, N. J.; James, W. D.; Drezek, R. A.; West, J. L. Near-Infrared Resonant Nanoshells for Combined Optical Imaging and Photothermal Cancer Therapy. *Nano Lett.* **2007**, *7* (7), 1929–1934. https://doi.org/10.1021/nl070610y.
(41) Schimpf, A. M.; Lounis, S. D.; Runnerstrom, E. L.; Milliron, D. J.; Gamelin, D. R. Redox Chemistries and Plasmon Energies of Photodoped In_2O_3 and Sn-Doped In_2O_3 (ITO) Nanocrystals. *J. Am. Chem. Soc.* **2015**, *137* (1), 518–524. https://doi.org/10.1021/ja5116953.
(42) Schimpf, A. M.; Ochsenbein, S. T.; Buonsanti, R.; Milliron, D. J.; Gamelin, D. R. Comparison of Extra Electrons in Colloidal N-Type Al3+-Doped and Photochemically Reduced ZnO Nanocrystals. *Chem. Commun.* **2012**, *48* (75), 9352–9354. https://doi.org/10.1039/C2CC34635D.
(43) Jain, P. K.; Lee, K. S.; El-Sayed, I. H.; El-Sayed, M. A. Calculated Absorption and Scattering Properties of Gold Nanoparticles of Different Size, Shape, and Composition: Applications in Biological Imaging and Biomedicine. *J. Phys. Chem. B* **2006**, *110* (14), 7238–7248. https://doi.org/10.1021/jp057170o.
(44) Lee, K.-S.; El-Sayed, M. A. Gold and Silver Nanoparticles in Sensing and Imaging: Sensitivity of Plasmon Response to Size, Shape, and Metal Composition. *J. Phys. Chem. B* **2006**, *110* (39), 19220–19225. https://doi.org/10.1021/jp062536y.

(45) Nehl, C. L.; Hafner, J. H. Shape-Dependent Plasmon Resonances of Gold Nanoparticles. *J. Mater. Chem.* **2008**, *18* (21), 2415–2419. https://doi.org/10.1039/B714950F.
(46) Chen, H.; Kou, X.; Yang, Z.; Ni, W.; Wang, J. Shape- and Size-Dependent Refractive Index Sensitivity of Gold Nanoparticles. *Langmuir* **2008**, *24* (10), 5233–5237. https://doi.org/10.1021/la800305j.
(47) Aksu, S.; Yanik, A. A.; Adato, R.; Artar, A.; Huang, M.; Altug, H. High-Throughput Nanofabrication of Infrared Plasmonic Nanoantenna Arrays for Vibrational Nanospectroscopy. *Nano Lett.* **2010**, *10* (7), 2511–2518. https://doi.org/10.1021/nl101042a.
(48) Neuman, T.; Huck, C.; Vogt, J.; Neubrech, F.; Hillenbrand, R.; Aizpurua, J.; Pucci, A. Importance of Plasmonic Scattering for an Optimal Enhancement of Vibrational Absorption in SEIRA with Linear Metallic Antennas. *J. Phys. Chem. C* **2015**, *119* (47), 26652–26662. https://doi.org/10.1021/acs.jpcc.5b08344.
(49) Abb, M.; Wang, Y.; Papasimakis, N.; de Groot, C. H.; Muskens, O. L. Surface-Enhanced Infrared Spectroscopy Using Metal Oxide Plasmonic Antenna Arrays. *Nano Lett.* **2014**, *14* (1), 346–352. https://doi.org/10.1021/nl404115g.
(50) Bukasov, R.; Shumaker-Parry, J. S. Silver Nanocrescents with Infrared Plasmonic Properties As Tunable Substrates for Surface Enhanced Infrared Absorption Spectroscopy. *Anal. Chem.* **2009**, *81* (11), 4531–4535. https://doi.org/10.1021/ac900477p.
(51) Adato, R.; Yanik, A. A.; Amsden, J. J.; Kaplan, D. L.; Omenetto, F. G.; Hong, M. K.; Erramilli, S.; Altug, H. Ultra-Sensitive Vibrational Spectroscopy of Protein Monolayers with Plasmonic Nanoantenna Arrays. *Proc. Natl. Acad. Sci.* **2009**, *106* (46), 19227–19232. https://doi.org/10.1073/pnas.0907459106.
(52) Kundu, J.; Le, F.; Nordlander, P.; Halas, N. J. Surface Enhanced Infrared Absorption (SEIRA) Spectroscopy on Nanoshell Aggregate Substrates. *Chem. Phys. Lett.* **2008**, *452* (1), 115–119. https://doi.org/10.1016/j.cplett.2007.12.042.
(53) Link, S.; El-Sayed, M. A. Spectral Properties and Relaxation Dynamics of Surface Plasmon Electronic Oscillations in Gold and Silver Nanodots and Nanorods. *J. Phys. Chem. B* **1999**, *103* (40), 8410–8426. https://doi.org/10.1021/jp9917648.
(54) Bardhan, R.; Grady, N. K.; Ali, T.; Halas, N. J. Metallic Nanoshells with Semiconductor Cores: Optical Characteristics Modified by Core Medium Properties. *ACS Nano* **2010**, *4* (10), 6169–6179. https://doi.org/10.1021/nn102035q.
(55) Rance, G. A.; Marsh, D. H.; Khlobystov, A. N. Extinction Coefficient Analysis of Small Alkanethiolate-Stabilised Gold Nanoparticles. *Chem. Phys. Lett.* **2008**, *460* (1), 230–236. https://doi.org/10.1016/j.cplett.2008.06.010.
(56) Ding, X.; Fu, D.; Kuang, Y.; Zou, Y.; Yang, X.; Feng, L.; Sun, X.; Wu, H.; Jiang, J. Seeded Growth of Cu2-XSe Nanocrystals and Their Size-Dependent Phototherapeutic Effect. *ACS Appl. Nano Mater.* **2018**. https://doi.org/10.1021/acsanm.8b00516.
(57) Qu, J.; Livache, C.; Martinez, B.; Gréboval, C.; Chu, A.; Meriggio, E.; Ramade, J.; Cruguel, H.; Xu, X. Z.; Proust, A.; Volatron, F.; Cabailh, G.; Goubet, N.; Lhuillier, E. Transport in ITO Nanocrystals with Short- to Long-Wave Infrared Absorption for Heavy-Metal-Free Infrared Photodetection. *ACS Appl. Nano Mater.* **2019**, *2* (3), 1621–1630. https://doi.org/10.1021/acsanm.9b00067.

(58) Lounis, S. D.; Runnerstrom, E. L.; Bergerud, A.; Nordlund, D.; Milliron, D. J. Influence of Dopant Distribution on the Plasmonic Properties of Indium Tin Oxide Nanocrystals. *J. Am. Chem. Soc.* **2014**, *136* (19), 7110–7116. https://doi.org/10.1021/ja502541z.
(59) Tandon, B.; Agrawal, A.; Heo, S.; Milliron, D. J. Competition between Depletion Effects and Coupling in the Plasmon Modulation of Doped Metal Oxide Nanocrystals. *Nano Lett.* **2019**. https://doi.org/10.1021/acs.nanolett.9b00079.
(60) Ellmer, K. Past Achievements and Future Challenges in the Development of Optically Transparent Electrodes. *Nat. Photonics* **2012**, *6* (12), 809–817. https://doi.org/10.1038/nphoton.2012.282.
(61) Ito, D.; Yokoyama, S.; Zaikova, T.; Masuko, K.; Hutchison, J. E. Synthesis of Ligand-Stabilized Metal Oxide Nanocrystals and Epitaxial Core/Shell Nanocrystals via a Lower-Temperature Esterification Process. *ACS Nano* **2014**, *8* (1), 64–75. https://doi.org/10.1021/nn401888h.
(62) Jansons, A. W.; Hutchison, J. E. Continuous Growth of Metal Oxide Nanocrystals: Enhanced Control of Nanocrystal Size and Radial Dopant Distribution. *ACS Nano* **2016**, *10* (7), 6942–6951. https://doi.org/10.1021/acsnano.6b02796.
(63) Crockett, B. M.; Jansons, A. W.; Koskela, K. M.; Johnson, D. W.; Hutchison, J. E. Radial Dopant Placement for Tuning Plasmonic Properties in Metal Oxide Nanocrystals. *ACS Nano* **2017**, *11* (8), 7719–7728. https://doi.org/10.1021/acsnano.7b01053.
(64) Frank, G.; Köstlin, H. Electrical Properties and Defect Model of Tin-Doped Indium Oxide Layers. *Appl. Phys. A* **1982**, *27* (4), 197–206. https://doi.org/10.1007/BF00619080.
(65) Lounis, S. D.; Runnerstrom, E. L.; Llordés, A.; Milliron, D. J. Defect Chemistry and Plasmon Physics of Colloidal Metal Oxide Nanocrystals. *J. Phys. Chem. Lett.* **2014**, *5* (9), 1564–1574. https://doi.org/10.1021/jz500440e.
(66) Tandon, B.; Yadav, A.; Khurana, D.; Reddy, P.; Santra, P. K.; Nag, A. Size-Induced Enhancement of Carrier Density, LSPR Quality Factor, and Carrier Mobility in Cr–Sn Doped In2O3 Nanocrystals. *Chem. Mater.* **2017**, *29* (21), 9360–9368. https://doi.org/10.1021/acs.chemmater.7b03351.
(67) Agrawal, A.; Johns, R. W.; Milliron, D. J. Control of Localized Surface Plasmon Resonances in Metal Oxide Nanocrystals. *Annu. Rev. Mater. Res.* **2017**, *47* (1), 1–31. https://doi.org/10.1146/annurev-matsci-070616-124259.
(68) Dai, Q.; Wang, Y.; Li, X.; Zhang, Y.; Pellegrino, D. J.; Zhao, M.; Zou, B.; Seo, J.; Wang, Y.; Yu, W. W. Size-Dependent Composition and Molar Extinction Coefficient of PbSe Semiconductor Nanocrystals. *ACS Nano* **2009**, *3* (6), 1518–1524. https://doi.org/10.1021/nn9001616.
(69) LI-COR Biosciences - Impacting Lives Through Science https://www.licor.com/bio/reagents/irdye-qc-1-nhs-ester (accessed Jul 23, 2019).
(70) Hamberg, I.; Granqvist, C. G. Evaporated Sn-doped In2O3 Films: Basic Optical Properties and Applications to Energy-efficient Windows. *J. Appl. Phys.* **1986**, *60* (11), R123–R160. https://doi.org/10.1063/1.337534.
(71) Ghosh, S. K.; Nath, S.; Kundu, S.; Esumi, K.; Pal, T. Solvent and Ligand Effects on the Localized Surface Plasmon Resonance (LSPR) of Gold Colloids. *J. Phys. Chem. B* **2004**, *108* (37), 13963–13971. https://doi.org/10.1021/jp047021q.

(72) Mendelsberg, R. J.; Garcia, G.; Li, H.; Manna, L.; Milliron, D. J. Understanding the Plasmon Resonance in Ensembles of Degenerately Doped Semiconductor Nanocrystals. *J. Phys. Chem. C* **2012**, *116* (22), 12226–12231. https://doi.org/10.1021/jp302732s.
(73) Luther, J. M.; Jain, P. K.; Ewers, T.; Alivisatos, A. P. Localized Surface Plasmon Resonances Arising from Free Carriers in Doped Quantum Dots. *Nat. Mater.* **2011**, *10* (5), 361–366. https://doi.org/10.1038/nmat3004.
(74) Ozbay, E. Plasmonics: Merging Photonics and Electronics at Nanoscale Dimensions. *Science* **2006**, *311* (5758), 189–193. https://doi.org/10.1126/science.1114849.
(75) Noginov, M. A.; Gu, L.; Livenere, J.; Zhu, G.; Pradhan, A. K.; Mundle, R.; Bahoura, M.; Barnakov, Yu. A.; Podolskiy, V. A. Transparent Conductive Oxides: Plasmonic Materials for Telecom Wavelengths. *Appl. Phys. Lett.* **2011**, *99* (2), 021101. https://doi.org/10.1063/1.3604792.
(76) Runnerstrom, E. L.; Kelley, K. P.; Sachet, E.; Shelton, C. T.; Maria, J.-P. Epsilon-near-Zero Modes and Surface Plasmon Resonance in Fluorine-Doped Cadmium Oxide Thin Films. *ACS Photonics* **2017**, *4* (8), 1885–1892. https://doi.org/10.1021/acsphotonics.7b00429.
(77) Runnerstrom, E. L.; Kelley, K. P.; Folland, T. G.; Nolen, J. R.; Engheta, N.; Caldwell, J. D.; Maria, J.-P. Polaritonic Hybrid-Epsilon-near-Zero Modes: Beating the Plasmonic Confinement vs Propagation-Length Trade-Off with Doped Cadmium Oxide Bilayers. *Nano Lett.* **2018**. https://doi.org/10.1021/acs.nanolett.8b04182.
(78) Kamakura, R.; Takeishi, T.; Murai, S.; Fujita, K.; Tanaka, K. Surface-Enhanced Infrared Absorption for the Periodic Array of Indium Tin Oxide and Gold Microdiscs: Effect of in-Plane Light Diffraction. *ACS Photonics* **2018**. https://doi.org/10.1021/acsphotonics.7b01265.
(79) Agrawal, A.; Singh, A.; Yazdi, S.; Singh, A.; Ong, G. K.; Bustillo, K.; Johns, R. W.; Ringe, E.; Milliron, D. J. Resonant Coupling between Molecular Vibrations and Localized Surface Plasmon Resonance of Faceted Metal Oxide Nanocrystals. *Nano Lett.* **2017**, *17* (4), 2611–2620. https://doi.org/10.1021/acs.nanolett.7b00404.
(80) Zhou, Z.; Kong, B.; Yu, C.; Shi, X.; Wang, M.; Liu, W.; Sun, Y.; Zhang, Y.; Yang, H.; Yang, S. Tungsten Oxide Nanorods: An Efficient Nanoplatform for Tumor CT Imaging and Photothermal Therapy. *Sci. Rep.* **2014**, *4*, 3653. https://doi.org/10.1038/srep03653.
(81) Wokaun, A.; Gordon, J. P.; Liao, P. F. Radiation Damping in Surface-Enhanced Raman Scattering. *Phys. Rev. Lett.* **1982**, *48* (14), 957–960. https://doi.org/10.1103/PhysRevLett.48.957.
(82) Zandi, O.; Agrawal, A.; Shearer, A. B.; Reimnitz, L. C.; Dahlman, C. J.; Staller, C. M.; Milliron, D. J. Impacts of Surface Depletion on the Plasmonic Properties of Doped Semiconductor Nanocrystals. *Nat. Mater.* **2018**, *17* (8), 710–717. https://doi.org/10.1038/s41563-018-0130-5.
(83) Crockett, B. M.; Jansons, A. W.; Koskela, K. M.; Sharps, M. C.; Johnson, D. W.; Hutchison, J. E. The Influence of Nanocrystal Size on the Optoelectronic Properties of Thin, Solution Cast Sn-Doped In2O3 Films. *Chem. Mater.* **2019**. https://doi.org/10.1021/acs.chemmater.9b00538.
(84) Bryan, J. D.; Gamelin, D. R. Doped Semiconductor Nanocrystals: Synthesis, Characterization, Physical Properties, and Applications. In *Progress in Inorganic*

Chemistry; John Wiley & Sons, Ltd, 2005; pp 47–126. https://doi.org/10.1002/0471725560.ch2.
(85) Johns, R. W.; Bechtel, H. A.; Runnerstrom, E. L.; Agrawal, A.; Lounis, S. D.; Milliron, D. J. Direct Observation of Narrow Mid-Infrared Plasmon Linewidths of Single Metal Oxide Nanocrystals. *Nat. Commun.* **2016**, *7*, 11583. https://doi.org/10.1038/ncomms11583.
(86) Kreibig, U.; Fragstein, C. v. The Limitation of Electron Mean Free Path in Small Silver Particles. *Z. Für Phys.* **1969**, *224* (4), 307–323. https://doi.org/10.1007/BF01393059.
(87) Moroz, A. Electron Mean Free Path in a Spherical Shell Geometry. *J. Phys. Chem. C* **2008**, *112* (29), 10641–10652. https://doi.org/10.1021/jp8010074.
(88) Bel Hadj Tahar, R.; Ban, T.; Ohya, Y.; Takahashi, Y. Tin Doped Indium Oxide Thin Films: Electrical Properties. *J. Appl. Phys.* **1998**, *83* (5), 2631–2645. https://doi.org/10.1063/1.367025.
(89) Ziabari, A. A.; Rozati, S. M. Investigation of the Effect of Band-Edge Nonparabolicity on the Carrier Transport in ITO Thin Films. *J. Korean Phys. Soc.* **2014**, *65* (4), 487–490. https://doi.org/10.3938/jkps.65.487.
(90) zum Felde, U.; Haase, M.; Weller, H. Electrochromism of Highly Doped Nanocrystalline SnO2:Sb. *J. Phys. Chem. B* **2000**, *104* (40), 9388–9395. https://doi.org/10.1021/jp0010031.
(91) Tandon, B.; Ghosh, S.; Milliron, D. J. Dopant Selection Strategy for High-Quality Factor Localized Surface Plasmon Resonance from Doped Metal Oxide Nanocrystals. *Chem. Mater.* **2019**, *31* (18), 7752–7760. https://doi.org/10.1021/acs.chemmater.9b02917.
(92) Shklovskii, B. I.; Efros, A. L. *Electronic Properties of Doped Semiconductors*; Springer Series in Solid-State Sciences; Springer-Verlag: Berlin Heidelberg, 1984.
(93) Greenberg, B. L.; Robinson, Z. L.; Reich, K. V.; Gorynski, C.; Voigt, B. N.; Francis, L. F.; Shklovskii, B. I.; Aydil, E. S.; Kortshagen, U. R. ZnO Nanocrystal Networks Near the Insulator–Metal Transition: Tuning Contact Radius and Electron Density with Intense Pulsed Light. *Nano Lett.* **2017**, *17* (8), 4634–4642. https://doi.org/10.1021/acs.nanolett.7b01078.
(94) Ray, S.; Banerjee, R.; Basu, N.; Batabyal, A. K.; Barua, A. K. Properties of Tin Doped Indium Oxide Thin Films Prepared by Magnetron Sputtering. *J. Appl. Phys.* **1983**, *54* (6), 3497–3501. https://doi.org/10.1063/1.332415.
(95) Talapin, D. V.; Lee, J.-S.; Kovalenko, M. V.; Shevchenko, E. V. Prospects of Colloidal Nanocrystals for Electronic and Optoelectronic Applications. *Chem. Rev.* **2010**, *110* (1), 389–458. https://doi.org/10.1021/cr900137k.
(96) Zabet-Khosousi, A.; Dhirani, A.-A. Charge Transport in Nanoparticle Assemblies. *Chem. Rev.* **2008**, *108* (10), 4072–4124. https://doi.org/10.1021/cr0680134.
(97) Miller, A.; Abrahams, E. Impurity Conduction at Low Concentrations. *Phys. Rev.* **1960**, *120* (3), 745–755. https://doi.org/10.1103/PhysRev.120.745.
(98) Thimsen, E.; Johnson, M.; Zhang, X.; Wagner, A. J.; Mkhoyan, K. A.; Kortshagen, U. R.; Aydil, E. S. High Electron Mobility in Thin Films Formed via Supersonic Impact Deposition of Nanocrystals Synthesized in Nonthermal Plasmas. *Nat. Commun.* **2014**, *5*, 5822. https://doi.org/10.1038/ncomms6822.
(99) Efros, A.; Shklovskii, B. *Electronic Properties of Doped Semiconductors*; Springer-Verlag: Berlin Heidel.

(100) Beloborodov, I. S.; Lopatin, A. V.; Vinokur, V. M. Universal Description of Granular Metals at Low Temperatures: Granular Fermi Liquid. *Phys. Rev. B* **2004**, *70* (20), 205120. https://doi.org/10.1103/PhysRevB.70.205120.
(101) Beloborodov, I. S.; Lopatin, A. V.; Vinokur, V. M.; Efetov, K. B. Granular Electronic Systems. *Rev. Mod. Phys.* **2007**, *79* (2), 469–518. https://doi.org/10.1103/RevModPhys.79.469.
(102) Akselrod, G. M.; Argyropoulos, C.; Hoang, T. B.; Ciracì, C.; Fang, C.; Huang, J.; Smith, D. R.; Mikkelsen, M. H. Probing the Mechanisms of Large Purcell Enhancement in Plasmonic Nanoantennas. *Nat. Photonics* **2014**, *8* (11), 835–840. https://doi.org/10.1038/nphoton.2014.228.
(103) Deeb, C.; Zhou, X.; Plain, J.; Wiederrecht, G. P.; Bachelot, R.; Russell, M.; Jain, P. K. Size Dependence of the Plasmonic Near-Field Measured via Single-Nanoparticle Photoimaging. *J. Phys. Chem. C* **2013**, *117* (20), 10669–10676. https://doi.org/10.1021/jp4020564.
(104) Baffou, G.; Quidant, R. Thermo-Plasmonics: Using Metallic Nanostructures as Nano-Sources of Heat. *Laser Photonics Rev.* **2013**, *7* (2), 171–187. https://doi.org/10.1002/lpor.201200003.
(105) Brongersma, M. L.; Halas, N. J.; Nordlander, P. Plasmon-Induced Hot Carrier Science and Technology. *Nat. Nanotechnol.* **2015**, *10* (1), 25–34. https://doi.org/10.1038/nnano.2014.311.
(106) Christopher, P.; Xin, H.; Linic, S. Visible-Light-Enhanced Catalytic Oxidation Reactions on Plasmonic Silver Nanostructures. *Nat. Chem.* **2011**, *3* (6), 467–472. https://doi.org/10.1038/nchem.1032.
(107) Christopher, P.; Moskovits, M. Hot Charge Carrier Transmission from Plasmonic Nanostructures. *Annu. Rev. Phys. Chem.* **2017**, *68* (1), 379–398. https://doi.org/10.1146/annurev-physchem-052516-044948.
(108) Della Gaspera, E.; Chesman, A. S. R.; van Embden, J.; Jasieniak, J. J. Non-Injection Synthesis of Doped Zinc Oxide Plasmonic Nanocrystals. *ACS Nano* **2014**, *8* (9), 9154–9163. https://doi.org/10.1021/nn5027593.
(109) Runnerstrom, E. L.; Bergerud, A.; Agrawal, A.; Johns, R. W.; Dahlman, C. J.; Singh, A.; Selbach, S. M.; Milliron, D. J. Defect Engineering in Plasmonic Metal Oxide Nanocrystals. *Nano Lett.* **2016**, *16* (5), 3390–3398. https://doi.org/10.1021/acs.nanolett.6b01171.
(110) Agrawal, A.; Kriegel, I.; Milliron, D. J. Shape-Dependent Field Enhancement and Plasmon Resonance of Oxide Nanocrystals. *J. Phys. Chem. C* **2015**, *119* (11), 6227–6238. https://doi.org/10.1021/acs.jpcc.5b01648.
(111) Zhang, C.; Chen, B.-Q.; Li, Z.-Y.; Xia, Y.; Chen, Y.-G. Surface Plasmon Resonance in Bimetallic Core–Shell Nanoparticles. *J. Phys. Chem. C* **2015**, *119* (29), 16836–16845. https://doi.org/10.1021/acs.jpcc.5b04232.
(112) Moskovits, M.; Srnová-Šloufová, I.; Vlčková, B. Bimetallic Ag–Au Nanoparticles: Extracting Meaningful Optical Constants from the Surface-Plasmon Extinction Spectrum. *J. Chem. Phys.* **2002**, *116* (23), 10435–10446. https://doi.org/10.1063/1.1449943.
(113) Lu, L.; Burkey, G.; Halaciuga, I.; Goia, D. V. Core–Shell Gold/Silver Nanoparticles: Synthesis and Optical Properties. *J. Colloid Interface Sci.* **2013**, *392*, 90–95. https://doi.org/10.1016/j.jcis.2012.09.057.

(114) Prodan, E.; Radloff, C.; Halas, N. J.; Nordlander, P. A Hybridization Model for the Plasmon Response of Complex Nanostructures. *Science* **2003**, *302* (5644), 419–422. https://doi.org/10.1126/science.1089171.
(115) Prodan, E.; Nordlander, P. Plasmon Hybridization in Spherical Nanoparticles. *J. Chem. Phys.* **2004**, *120* (11), 5444–5454. https://doi.org/10.1063/1.1647518.
(116) Liu, Z.; Zhong, Y.; Shafei, I.; Jeong, S.; Wang, L.; Nguyen, H. T.; Sun, C.-J.; Li, T.; Chen, J.; Chen, L.; Losovyj, Y.; Gao, X.; Ma, W.; Ye, X. Broadband Tunable Mid-Infrared Plasmon Resonances in Cadmium Oxide Nanocrystals Induced by Size-Dependent Nonstoichiometry. *Nano Lett.* **2020**, *20* (4), 2821–2828. https://doi.org/10.1021/acs.nanolett.0c00542.
(117) Hewitt, R. W.; Winograd, N. Oxidation of Polycrystalline Indium Studied by X-ray Photoelectron Spectroscopy and Static Secondary Ion Mass Spectroscopy. *J. Appl. Phys.* **1980**, *51* (5), 2620–2624. https://doi.org/10.1063/1.327991.
(118) A. Sihvola. *Electromagnetic Mixing Formulas and Applications*; The Institution of Electrical Engineers, 1999.
(119) Whitney, A. V.; Elam, J. W.; Zou, S.; Zinovev, A. V.; Stair, P. C.; Schatz, G. C.; Van Duyne, R. P. Localized Surface Plasmon Resonance Nanosensor: A High-Resolution Distance-Dependence Study Using Atomic Layer Deposition. *J. Phys. Chem. B* **2005**, *109* (43), 20522–20528. https://doi.org/10.1021/jp0540656.
(120) Haes, A. J.; Zou, S.; Schatz, G. C.; Van Duyne, R. P. Nanoscale Optical Biosensor: Short Range Distance Dependence of the Localized Surface Plasmon Resonance of Noble Metal Nanoparticles. *J. Phys. Chem. B* **2004**, *108* (22), 6961–6968. https://doi.org/10.1021/jp036261n.
(121) Haes, A. J.; Zou, S.; Schatz, G. C.; Van Duyne, R. P. A Nanoscale Optical Biosensor: The Long Range Distance Dependence of the Localized Surface Plasmon Resonance of Noble Metal Nanoparticles. *J. Phys. Chem. B* **2004**, *108* (1), 109–116. https://doi.org/10.1021/jp0361327.
(122) Adato, R.; Aksu, S.; Altug, H. Engineering Mid-Infrared Nanoantennas for Surface Enhanced Infrared Absorption Spectroscopy. *Mater. Today* **2015**, *18* (8), 436–446. https://doi.org/10.1016/j.mattod.2015.03.001.
(123) Wu, C.; Khanikaev, A. B.; Adato, R.; Arju, N.; Yanik, A. A.; Altug, H.; Shvets, G. Fano-Resonant Asymmetric Metamaterials for Ultrasensitive Spectroscopy and Identification of Molecular Monolayers. *Nat. Mater.* **2012**, *11* (1), 69–75. https://doi.org/10.1038/nmat3161.
(124) Cho, S. H.; Roccapriore, K. M.; Dass, C. K.; Ghosh, S.; Choi, J.; Noh, J.; Reimnitz, L. C.; Heo, S.; Kim, K.; Xie, K.; Korgel, B. A.; Li, X.; Hendrickson, J. R.; Hachtel, J. A.; Milliron, D. J. Spectrally Tunable Infrared Plasmonic F,Sn:In2O3 Nanocrystal Cubes. *J. Chem. Phys.* **2020**, *152* (1), 014709. https://doi.org/10.1063/1.5139050.
(125) Sönnichsen, C.; Reinhard, B. M.; Liphardt, J.; Alivisatos, A. P. A Molecular Ruler Based on Plasmon Coupling of Single Gold and Silver Nanoparticles. *Nat. Biotechnol.* **2005**, *23* (6), 741–745. https://doi.org/10.1038/nbt1100.
(126) Jain, P. K.; El-Sayed, M. A. Universal Scaling of Plasmon Coupling in Metal Nanostructures: Extension from Particle Pairs to Nanoshells. *Nano Lett.* **2007**, *7* (9), 2854–2858. https://doi.org/10.1021/nl071496m.

(127) Tandon, B.; Agrawal, A.; Heo, S.; Milliron, D. J. Competition between Depletion Effects and Coupling in the Plasmon Modulation of Doped Metal Oxide Nanocrystals. *Nano Lett.* **2019**, *19* (3), 2012–2019. https://doi.org/10.1021/acs.nanolett.9b00079.
(128) Sun, Y.; Xia, Y. Increased Sensitivity of Surface Plasmon Resonance of Gold Nanoshells Compared to That of Gold Solid Colloids in Response to Environmental Changes. *Anal. Chem.* **2002**, *74* (20), 5297–5305. https://doi.org/10.1021/ac0258352.
(129) Giraldo, J. P.; Landry, M. P.; Kwak, S.-Y.; Jain, R. M.; Wong, M. H.; Iverson, N. M.; Ben-Naim, M.; Strano, M. S. A Ratiometric Sensor Using Single Chirality Near-Infrared Fluorescent Carbon Nanotubes: Application to In Vivo Monitoring. *Small* **2015**, *11* (32), 3973–3984. https://doi.org/10.1002/smll.201403276.
(130) Lv, X.; Liu, J.; Liu, Y.; Zhao, Y.; Sun, Y.-Q.; Wang, P.; Guo, W. Ratiometric Fluorescence Detection of Cyanide Based on a Hybrid Coumarin–Hemicyanine Dye: The Large Emission Shift and the High Selectivity. *Chem. Commun.* **2011**, *47* (48), 12843–12845. https://doi.org/10.1039/C1CC15721C.
(131) Xing, P.; Xu, Y.; Li, H.; Liu, S.; Lu, A.; Sun, S. Ratiometric and Colorimetric Near-Infrared Sensors for Multi-Channel Detection of Cyanide Ion and Their Application to Measure β-Glucosidase. *Sci. Rep.* **2015**, *5* (1), 1–6. https://doi.org/10.1038/srep16528.
(132) Zhao, Q.; Zhao, T.; Guo, J.; Chen, W.; Zhang, M.; Kagan, C. R. The Effect of Dielectric Environment on Doping Efficiency in Colloidal PbSe Nanostructures. *ACS Nano* **2018**, *12* (2), 1313–1320. https://doi.org/10.1021/acsnano.7b07602.
(133) Runnerstrom, E. L.; Kelley, K. P.; Folland, T. G.; Nolen, J. R.; Engheta, N.; Caldwell, J. D.; Maria, J.-P. Polaritonic Hybrid-Epsilon-near-Zero Modes: Beating the Plasmonic Confinement vs Propagation-Length Trade-Off with Doped Cadmium Oxide Bilayers. *Nano Lett.* **2019**, *19* (2), 948–957. https://doi.org/10.1021/acs.nanolett.8b04182.
(134) Oulton, R. F.; Sorger, V. J.; Genov, D. A.; Pile, D. F. P.; Zhang, X. A Hybrid Plasmonic Waveguide for Subwavelength Confinement and Long-Range Propagation. *Nat. Photonics* **2008**, *2* (8), 496–500. https://doi.org/10.1038/nphoton.2008.131.
(135) Linic, S.; Christopher, P.; Ingram, D. B. Plasmonic-Metal Nanostructures for Efficient Conversion of Solar to Chemical Energy. *Nat. Mater.* **2011**, *10* (12), 911–921. https://doi.org/10.1038/nmat3151.
(136) Li, K.; Hogan, N. J.; Kale, M. J.; Halas, N. J.; Nordlander, P.; Christopher, P. Balancing Near-Field Enhancement, Absorption, and Scattering for Effective Antenna–Reactor Plasmonic Photocatalysis. *Nano Lett.* **2017**, *17* (6), 3710–3717. https://doi.org/10.1021/acs.nanolett.7b00992.
(137) Aslam, U.; Rao, V. G.; Chavez, S.; Linic, S. Catalytic Conversion of Solar to Chemical Energy on Plasmonic Metal Nanostructures. *Nat. Catal.* **2018**, *1* (9), 656. https://doi.org/10.1038/s41929-018-0138-x.
(138) Zhou, L.; Swearer, D. F.; Zhang, C.; Robatjazi, H.; Zhao, H.; Henderson, L.; Dong, L.; Christopher, P.; Carter, E. A.; Nordlander, P.; Halas, N. J. Quantifying Hot Carrier and Thermal Contributions in Plasmonic Photocatalysis. *Science* **2018**, *362* (6410), 69–72. https://doi.org/10.1126/science.aat6967.
(139) Johns, R. W.; Blemker, M. A.; Azzaro, M. S.; Heo, S.; Runnerstrom, E. L.; Milliron, D. J.; Roberts, S. T. Charge Carrier Concentration Dependence of Ultrafast Plasmonic

Relaxation in Conducting Metal Oxide Nanocrystals. *J. Mater. Chem. C* **2017**, *5* (23), 5757–5763. https://doi.org/10.1039/C7TC00600D.
(140) Hexemer, A.; Bras, W.; Glossinger, J.; Schaible, E.; Gann, E.; Kirian, R.; MacDowell, A.; Church, M.; Rude, B.; Padmore, H. A SAXS/WAXS/GISAXS Beamline with Multilayer Monochromator. *J. Phys. Conf. Ser.* **2010**, *247*, 012007. https://doi.org/10.1088/1742-6596/247/1/012007.
(141) Ilavsky, J. *Nika* : Software for Two-Dimensional Data Reduction. *J. Appl. Crystallogr.* **2012**, *45* (2), 324–328. https://doi.org/10.1107/S0021889812004037.
(142) Ilavsky, J.; Jemian, P. R. *Irena* : Tool Suite for Modeling and Analysis of Small-Angle Scattering. *J. Appl. Crystallogr.* **2009**, *42* (2), 347–353. https://doi.org/10.1107/S0021889809002222.
(143) Singh, A.; Lindquist, B. A.; Ong, G. K.; Jadrich, R. B.; Singh, A.; Ha, H.; Ellison, C. J.; Truskett, T. M.; Milliron, D. J. Linking Semiconductor Nanocrystals into Gel Networks through All-Inorganic Bridges. *Angew. Chem. Int. Ed.* **2015**, *54* (49), 14840–14844. https://doi.org/10.1002/anie.201508641.
(144) Barabara Stuart. Organic Molecules. In *Infrared Spectroscopy: Fundamentals and Applications*; John Wiley & Sons, Ltd, 2004; pp 71–93.
(145) Averitt, R. D.; Westcott, S. L.; Halas, N. J. Linear Optical Properties of Gold Nanoshells. *JOSA B* **1999**, *16* (10), 1824–1832. https://doi.org/10.1364/JOSAB.16.001824.
(146) Cho, S. H.; Ghosh, S.; Berkson, Z. J.; Hachtel, J. A.; Shi, J.; Zhao, X.; Reimnitz, L. C.; Dahlman, C. J.; Ho, Y.; Yang, A.; Liu, Y.; Idrobo, J.-C.; Chmelka, B. F.; Milliron, D. J. Syntheses of Colloidal F:In2O3 Cubes: Fluorine-Induced Faceting and Infrared Plasmonic Response. *Chem. Mater.* **2019**, *31* (7), 2661–2676. https://doi.org/10.1021/acs.chemmater.9b00906.